

Miscibility gap of hydrogen-helium mixtures at high pressures and temperatures

Mischungslücke von Wasserstoff-Helium-Mischungen unter hohen
Drücken und Temperaturen

Dissertation
zur Erlangung des akademischen Grades eines
doctor rerum naturalium (Dr. rer. nat.)
der Mathematisch-Naturwissenschaftlichen Fakultät
der Universität Rostock

vorgelegt von
Manuel Schöttler
geboren am 31.07.1988
in Schwerin

Rostock, 10.08.2018

Tag der Abgabe: 10.08.2018

Tag der Verteidigung: 30.11.2018

Gutachter:

1. Prof. Dr. rer. nat. habil. Ronald Redmer
Institut für Physik, Universität Rostock
2. Prof. Dr. Marcus D. Knudson
Institute for Shock Physics, Washington State University

Abstract

Hydrogen-helium demixing has long been proposed to occur in the gas giants Jupiter and Saturn. Strong indications for this process came from measurements of the atmospheric He abundances that revealed a depletion compared to the protosolar value. The miscibility gap probably results in He rain, where the released gravitational energy from the sinking droplets increases the planet's internal heat budget and is a possible explanation for Saturn's excess luminosity. Quantitative assessments require precise knowledge of the thermodynamic conditions at which demixing occurs.

In this work, the miscibility gap of hydrogen-helium mixtures is calculated under conditions relevant for the gas giants Jupiter and Saturn. Density functional theory coupled to classical molecular dynamics simulations is used to obtain the equations of state for 29 helium concentrations. The entropy is calculated using a combination of thermodynamic integration of the equation of state and coupling-constant integration. In contrast to previous work, an exchange-correlation functional is used that treats non-local correlations also known as van der Waals effects. New planetary profiles for Jupiter and Saturn are derived and compared to the miscibility diagram. These profiles give strong indications that there is demixing in Saturn but possibly not in Jupiter.

Zusammenfassung

Es wird seit langem vermutet, dass Wasserstoff und Helium im Inneren der Gasriesen Jupiter und Saturn entmischen. Konkrete Hinweise darauf lieferten Messungen des atmosphärischen Heliumgehalts. In beiden Planeten ist dieser geringer als man im Vergleich zum protosolaren Heliumgehalt erwarten würde. Die Mischungslücke führt wahrscheinlich zu Heliumregen, durch den die Gravitationsenergie der sinkenden Tropfen zu einer Erhöhung des internen Wärmehaushalts führt. Dieser Prozess liefert eine mögliche Erklärung für die besonders hohe Leuchtkraft von Saturn. Um quantitative Aussagen treffen zu können, ist es notwendig genau zu wissen, unter welchen Bedingungen Wasserstoff und Helium entmischen.

In dieser Arbeit wird die Mischungslücke von Wasserstoff-Helium-Mischungen unter Bedingungen, die für die großen Gasplaneten Jupiter und Saturn relevant sind, berechnet. Dichtefunktionaltheorie zusammen mit klassischer Molekulardynamiksimulation wird genutzt, um die Zustandsgleichung für 29 Heliumkonzentrationen zu berechnen. Die Entropie wird mit Hilfe von thermodynamischer Integration in Zusammenhang mit 'coupling-constant' Integration berechnet. Im Gegensatz zu früheren Arbeiten wurde hier ein Austausch- und Korrelationsfunktional benutzt, das nicht-lokale Korrelationen - auch bekannt als van der Waals Effekte - berücksichtigt. Neue Planetenprofile für Jupiter und Saturn werden berechnet und mit dem Entmischungsdiagramm verglichen. Diese Profile geben starke Hinweise darauf, dass Entmischung in Saturn stattfindet aber möglicherweise nicht in Jupiter.

Contents

1	Introduction	1
1.1	Jupiter and Saturn	2
1.2	Phase transitions in H and He: experiment and theory	6
1.3	Miscibility gap of H-He mixtures	10
1.4	Motivation and outline of this thesis	15
2	Methods	17
2.1	Many-body Schrödinger equation	17
2.2	Density functional theory (DFT)	19
2.2.1	Hohenberg-Kohn theorems	19
2.2.2	Kohn-Sham formalism	20
2.2.3	Extension to finite temperatures	22
2.2.4	Exchange-correlation functionals	24
2.2.5	Non-local correlation and van der Waals density functionals	26
2.2.6	Periodic boundary conditions, plane waves and pseudopotentials	30
2.3	Molecular dynamics (MD)	31
2.4	Nuclear quantum corrections	33
2.5	Thermodynamics of binary systems	35
2.6	Entropy	43
2.6.1	Thermodynamic integration	43
2.6.2	Methods based on the VDOS	44
2.6.3	Coupling-constant integration (CCI)	47
2.7	Numerical settings of the DFT-MD simulations	53
3	Equation of state	55
3.1	Hydrogen	56
3.2	Helium	58
3.3	H-He mixtures	59

4	Entropy of H-He mixtures	63
4.1	Basic idea and strategy	63
4.2	Entropy at the reference point	64
4.3	Entropies for arbitrary pressures and temperatures	68
5	Gibbs free energy of mixing of H-He mixtures	73
5.1	Comparison of PBE and vdW-DF results	73
5.2	Nuclear quantum corrections to the Gibbs free energy of mixing . . .	74
5.3	Total Gibbs free energy of mixing for the vdW-DF	78
6	Miscibility diagram	81
6.1	Miscibility gap for PBE and vdW-DF using the ideal entropy	81
6.2	Miscibility gap for the vdW-DF using the ideal and non-ideal entropy	83
6.3	Miscibility gap for solar He concentration	85
7	Planetary isentropes	87
7.1	Calculating planetary $p - T$ profiles	87
7.2	Profiles for Jupiter and Saturn	89
8	Conclusion	95
8.1	Summary	95
8.2	Outlook	96
A	Derivations	101
A.1	Thermodynamic integration formula for p, T	101
A.2	Reduced coupling-constant integration	102
	Bibliography	104
	Curriculum Vitae / Lebenslauf	131
	Acknowledgments / Danksagung	135
	Statement of authorship / Selbständigkeitserklärung	137

List of Figures

1.1.1 Possible interiors for Saturn	5
1.2.1 Hydrogen phase diagram	7
1.2.2 Helium phase diagram	9
1.3.1 Experimental miscibility gap	11
1.3.2 Miscibility gap before this work	12
1.3.3 Miscibility gap for solar He abundance before this work	14
2.5.1 Schematic depiction of a demixed system	36
2.5.2 Schematic depiction of the Gibbs free energy of mixing for different conditions	39
2.5.3 Method of intercepts	42
2.5.4 Partial molar volumes at constant temperature and He fraction . . .	42
2.6.1 Thermodynamic integration of the reflected Yukawa potential	50
2.6.2 Thermodynamic integration of the DFT system	51
2.6.3 Radial distribution functions for H and He for different coupling- constants	52
3.1.1 Volume vs. pressure for H	56
3.1.2 Energy vs. pressure for H	57
3.2.1 Volume vs. pressure for He	58
3.2.2 Energy vs. pressure for He	59
3.3.1 Volume, energy, and enthalpy of mixing at 3 000 K and 10 000 K . . .	61
4.2.1 Partial volumes at the reference state	65
4.2.2 Entropy at the reference state	66
4.2.3 Entropy of mixing at the reference state	67
4.3.1 Benchmarking thermodynamic integration on an isotherm	69
4.3.2 Benchmarking thermodynamic integration for the entropy of mixing .	70
5.1.1 Gibbs free energy of mixing: PBE vs. vdW-DF for ideal entropy . . .	74

5.2.1 Quantum corrections to free energy	75
5.2.2 Quantum corrections to pressure	76
5.2.3 Quantum corrections to Gibbs free energy of mixing at 1 Mbar	77
5.2.4 Quantum corrections to Gibbs free energy of mixing at 10 Mbar . . .	78
5.3.1 Gibbs free energy of mixing at 1 Mbar	79
5.3.2 Gibbs free energy of mixing at 10 Mbar	80
6.1.1 New miscibility gap with ideal entropy of mixing	82
6.2.1 New miscibility gap with non-ideal mixing entropy	84
6.3.1 New miscibility gap at solar He abundance	85
7.2.1 Entropy of Jupiter and Saturn at 1 bar	90
7.2.2 Isentropes for Jupiter and Saturn	91
7.2.3 Evolution of Saturn	93
8.2.1 Temperature of exoplanets	98

List of Tables

1.1.1 Properties of Jupiter and Saturn	3
2.6.1 Coefficients for the reflected Yukawa potential	49

Chapter 1

Introduction

Hydrogen (H) and helium (He) are the most abundant elements in the universe [1]. They make up 98% of the baryonic matter and are major constituents of stars and giant gas planets like Jupiter and Saturn. In stars, hydrogen is converted to He via the proton-proton chain reaction [2]. This fusion process occurs in objects with masses greater than roughly 75 Jupiter masses (M_J) [3–5]. Below this threshold, the class of brown dwarfs (masses between $13 M_J$ and $75 M_J$) bridges the gap between stars and massive planets. Understanding the structure, evolution, and composition of astrophysical objects is an important area of physics. The possibility of finding Earth-like planets that potentially host life forms motivates researchers in various fields and science fiction authors alike. Still, it is impossible to visit other planets beyond our solar system so that most of the planetary research is limited to remote observations. Earth-bound facilities (e.g. the Calar Alto Observatory [6], the Subaru Telescope [7], and the upcoming ELT [8]), observational initiatives (e.g. WASP [9] and YETI [10]), and space missions (e.g. the Hubble Space Telescope [11], Kepler [12], TESS [13], and the upcoming PLATO mission [14]) can reveal information like radius R , mass M , and the distance of a planet to its host star. Moreover, spectral signatures of the host star and the atmosphere of the exoplanet are used to infer their chemical composition. The information about planets in our solar system is much broader since many spacecraft have been launched to explore their special features. From these missions, additional observables can be obtained, such as atmospheric particle abundances x_i for each species i , gravitational moments J_n of order n , magnetic field strengths, the rotational frequency ω , and the luminosity L . These observables are used in planetary models to constrain the possible interior composition and structure. Additional input is required about the equation of state of the contained material for a wide range of pressures and temperatures.

Furthermore, knowledge about phase transitions and chemical reactions is required because they influence the planet's energy balance. Hydrogen atoms are very reactive. They form hydrogen molecules under normal conditions and an enormous amount of stable compounds with other elements. For planets, methane (CH_4), water (H_2O) [15–17], ammonia (NH_3) [18–20], and hydrogen sulfide (H_2S) [21] are important, especially for the ice giants Neptune and Uranus [22]. The situation is much simpler for the noble gas He, since it forms no stable compounds at room temperature. Still, there are experimentally verified compounds at high pressures containing sodium and sodium plus oxygen [23], but it is unclear if these structures could form in the planetary interior.

In the further course of this chapter, special attention will be paid to the gas giant planets Jupiter and Saturn that mainly contain hydrogen and helium. Many space missions have been sent to these planets. Their observations have led to puzzling questions about the He abundance and the relation between the miscibility gap of H-He mixtures and the internal structure of these planets. Furthermore phase transitions in pure H and He will be discussed and the current knowledge of the miscibility diagram will be reviewed. It will become clear why an improved miscibility diagram of hydrogen-helium mixtures is needed and it will be outlined, how the miscibility diagram is calculated in this thesis.

1.1 Jupiter and Saturn

The exploration of Jupiter with space probes started with the Pioneer 10 mission on March, 2nd 1972 [24, 25]. It reached the largest solar system planet in November 1973 and delivered new insights on the structure of Jupiter. It took high quality pictures of the zonal winds, the giant red spot, and also found a smaller red spot that was gone when Pioneer 11 arrived. Pioneer 10 confirmed that Jupiter radiates 2.5 times more heat into space than it receives from the Sun and provided first measurements of the He abundance and thermodynamic conditions in the atmosphere. It measured the magnetic field of Jupiter that extends almost to Saturn's orbit. First gravitational measurements revealed hints towards a possible small, fluid core.

Since then, five more missions were launched to explore Jupiter: Pioneer 11 [26], Voyager 1 [27, 28], Voyager 2 [29, 30], Galileo [31], and Juno [32, 33]. The Pioneer and Voyager missions were fly-by missions, whereas Galileo and Juno were designed as orbiters. The special feature of the Galileo orbiter was an entry probe [34, 35], which was released in July 1995 and descended into the planet. It provided an accurate measurement of the He content in the atmosphere, see Tab. 1.1.1, and reached a

Property	Jupiter	Saturn
$M [M_E]$	317.83	95.16
$R [R_E]$	11.209	9.449
$T_{1\text{bar}} [\text{K}]$	166	149
$\varrho_{\text{mean}} [\text{g/ccm}]$	1.326	0.687
Y_{atm}	0.238 ± 0.005 [35]	$0.18 \dots 0.25$ [45]

Table 1.1.1: Selected properties of Jupiter and Saturn. Mass M , equatorial radius r at 1 bar, temperature $T_{1\text{bar}}$ at 1 bar, mean density ϱ_{mean} , and helium mass fraction in the atmosphere Y_{atm} are shown.

pressure of 22 bar at 426 K in a depth of 146 km below the 1 bar level [35] before the signal was disrupted. The latest Jupiter probe is the Juno spacecraft, which is orbiting Jupiter since July 2016. Some of its scientific objectives [36] are: measuring the gravitational and magnetic field (especially the higher harmonics), determining the ratio of oxygen versus hydrogen to link formation and interior models [37], estimating Jupiter’s core mass, and investigating the magnetosphere near the planet’s poles. First measurements of the gravitational field [38] have been used for comparison with structure models, which suggest that Jupiter has a dilute core with a mass of 7–25 Earth masses [39]. Furthermore a non-uniform distribution of ammonia has been detected [40] indicating that ammonia vapour might play a similar role on Jupiter as water vapour on Earth, regarding the weather on both planets [41]. The atmospheric jet streams have been shown to extend possibly to a depth of 3 000 km [42] and influence the gravity field [43]. Juno measurements of the magnetic field have revealed that current models underestimate its magnitude by a almost a factor of two [44]. Many more results are expected to come in the future.

Pioneer 11 and the two Voyager spacecraft were sent to Saturn after their fly-bys at Jupiter [30, 46, 47]. They discovered additional rings, unknown moons, gave access to new images of Saturn and performed measurements of Saturn’s magnetic field. The latest Saturn mission was Cassini-Huygens [48–50], which was launched in October 1997 and entered Saturn’s orbit in July 2004. It consisted of the Cassini orbiter and the Huygens lander, which was sent onto the moon Titan. The scientific objectives of this mission focused on the exploration of the whole Saturnian system instead of Saturn only. Nevertheless, Cassini’s instruments enabled the first calculation of Saturn’s Love number directly from observations [51], which potentially offers new constraints on Saturn’s interior profile, because the fluid Love number is sensitive to the density distribution inside the planet [52].

Jupiter and Saturn differ significantly in terms of mass, radius, temperature, and mean density as can be seen from Tab. 1.1.1. Yet, they are similar in the sense, that they contain mainly hydrogen and helium. They also share the puzzling observation, that He is depleted in both planets in comparison to the protosolar He abundance. The gas giant planets have formed from the same protosolar nebula and, therefore, should contain similar amounts of H and He. The first measurement of the He abundance in Jupiter and Saturn originated from the Voyager missions and revealed He mass fractions of $Y_J = 0.18 \pm 0.04$ [53] for Jupiter and $Y_S = 0.06 \pm 0.05$ [54] for Saturn. Comparing these values to the present-day solar values is tricky because in the Sun, He is produced via fusion. Therefore, measured atmospheric abundances are not representative for the entire Sun. Additionally, He is able to gravitationally settle towards the Sun's interior. Solar models revealed that the protosolar He mass fraction should be $Y_P = 0.27 \dots 0.28$ [55, 56]. The same models yield a present-day He fraction of $Y_\odot = 0.247 \dots 0.251$ [55, 56] for the solar atmosphere. Hence, there is a strong He depletion in the atmospheres of Jupiter and Saturn compared to the protosolar value. However, the Galileo entry probe determined an atmospheric He mass fraction different from that of the Voyager missions, namely $Y_J = 0.238 \pm 0.005$. The significant discrepancy led to a reevaluation of the Voyager data for Saturn, where an updated He mass fraction of $Y_S = 0.18 \dots 0.25$ was determined [45]. Planetary interior models based on the latest Cassini data led to a mass fraction of $Y_S = 0.16 \dots 0.22$ [57], in agreement with the reanalysed Voyager data. Still, a new Saturn entry probe is required to precisely measure the atmospheric composition.

The similarity of the Saturn and Jupiter He abundances to the present-day atmospheric He abundance of the Sun is intriguing, but deemed to be coincidental. The mechanism of the depletion is different in Jupiter and Saturn: gravitational settling is expected to be negligible compared to the effect of convection, which would remix the interior. Instead, it has been proposed that the immiscibility of hydrogen and helium under certain conditions could explain the measured He abundances [58]. The idea is that H-He separation leads to small helium-rich droplets that precipitate and fall towards the planetary core despite convection. Thus the outermost layer would show a lower He fraction compared to the mean He fraction that should be similar to the protosolar value. The descending helium droplets would convert gravitational energy to heat that contributes to the luminosity. This process would explain Saturn's high excess luminosity [59–61]. If H-He demixing is neglected, most evolution models of Saturn fail to describe the observed luminosity and yield a planetary age much smaller than the solar age of 4.56 Gyr [62]. However, Leconte and Chabrier [63]

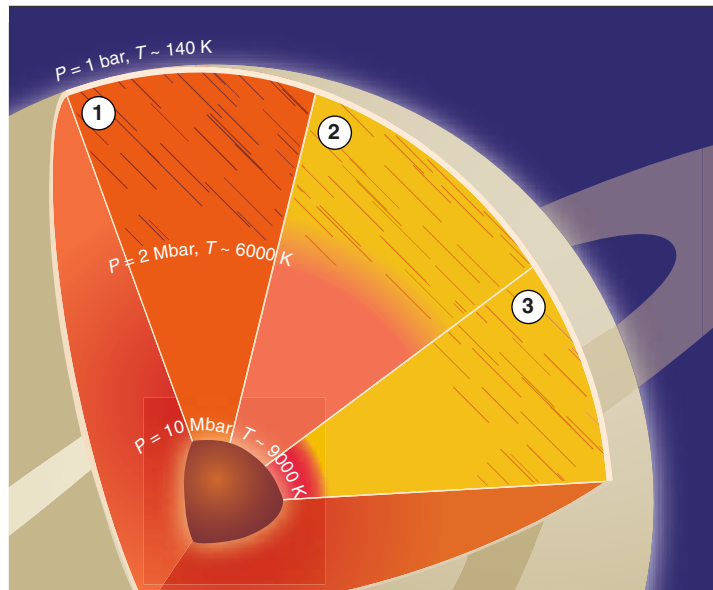


Figure 1.1.1: Different possible interiors for Saturn. Interior 1 shows a uniform distribution of He, where the orange colour refers to a protosolar He abundance. In hashed regions, H is molecular and insulating and in unhashed regions H is an atomic metal. In interior 2, He has separated from H according to the miscibility diagram of Ref. [58]. Helium-poor regions are indicated by lighter, yellowish colours and He-rich regions by darker orange colours. Interior 3 shows a current Saturn model according to Ref. [62]. Figure from Fortney J.J. *Looking into the giant planets*. *Science* **305**, 1414 (2004). Reprinted with permission from AAAS. Credit to Preston Huey/Science.

proposed layered convection models that can reproduce Saturn's correct age without H-He demixing, albeit not entirely ruling it out. In fact, a compositional gradient as caused by H-He demixing is helpful for their layered convection models. Hence, a combination of demixing and layered convection is possible. Another observation that supports H-He demixing is the depletion of neon in Jupiter. Calculations have shown, that neon dissolves preferably in the non-metallic He rather than in the metallic hydrogen [64]. Since the metallisation of hydrogen triggers the demixing [65], neon would sink towards the core with the helium. The opposite is true for argon [64] which was found to be present in Jupiter's atmosphere in a higher abundance than the protosolar value, because it tends to dissolve mainly in the metallic hydrogen. The effect of demixing has a huge impact on the interior structure models as shown in Fig. 1.1.1 for Saturn. If no demixing occurs in Saturn or if the planet is at an evolutionary stage, where the interior temperature is high such that demixing

has not yet begun, the interior would be homogeneously mixed and the He abundance would be Y_P as depicted by interior 1. Upon cooling, demixing could happen in a certain region of the planet, such that He rain occurs and an outer He-poor and inner He-rich layer forms as shown by interiors 2 and 3. Different miscibility diagrams can lead to different amounts of He in these layers and to a case, where a He-rich layer is situated directly above the core as shown by interior 3. Hence, the precise knowledge of the miscibility diagram is crucial for planetary modelling.

1.2 Phase transitions in H and He: experiment and theory

It is important to review the relevant phase transitions and current state of research for the pure constituents, before phase transitions in a mixture of hydrogen and helium are discussed in the next section. The phase diagram of the seemingly simplest element hydrogen shows many different structures and phases. In the solid, there are currently six proposed insulating phases [66, 67]. More than 80 years ago, it was proposed by Wigner and Huntington [68] that solid hydrogen should become metallic under high pressure. At that time, the estimated minimum pressure to convert hydrogen to the metallic phase was 2.5 kbar, which was beyond feasibility for experiments back then. Over the years, the insulator-to-metal transition (IMT) has been investigated using the continuously improving theoretical and experimental methods, see e.g. Ref. [69]. The invention of diamond anvil cells (DAC) has enabled static high pressure experiments in the multi-megabar regime. Pressures of up to 10 Mbar have been obtained for certain materials [70–72] - however, not for hydrogen, where pressures have long been limited to below 4 Mbar [66]. Experimental challenges originate from the mobile hydrogen atoms, which are able to diffuse through the diamond and the rhenium gasket, especially at higher temperatures [67]. A further problem is diamond failure due to defects, residual stress, or laser-activated defect growth [73]. Despite these difficulties, Dias and Silvera [73] reported the first observation of the Wigner-Huntington transition, which occurred at 4.95 Mbar, see Fig. 1.2.1. However, these results are controversially debated in the scientific community [74–77] because metallisation could only be achieved for a single run and more data need to be gathered.

Under standard conditions for temperature and pressure, hydrogen is molecular. At higher temperatures, hydrogen undergoes an IMT in the liquid phase, which has historically been known as the plasma phase transition (PPT) [87]. Chemical

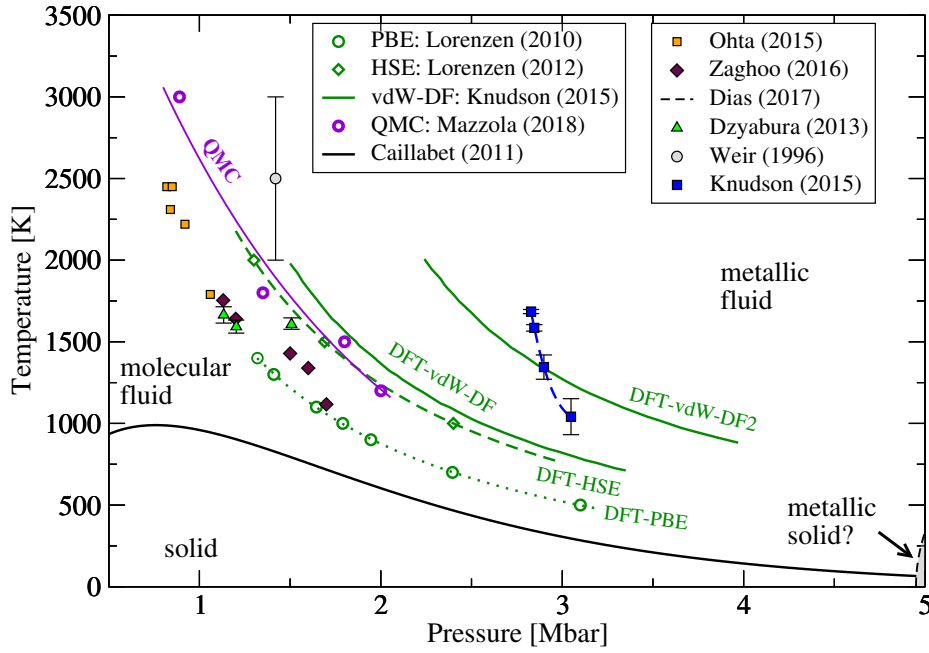


Figure 1.2.1: High-pressure hydrogen phase diagram. Laser-heated DAC experiments performed by Dzyabura *et al.* [78], Ohta *et al.* [79], and Zaghoo *et al.* [80]. Dynamic compression experiments by Weir *et al.* [81, 82] and Knudson *et al.* [83]. Density functional theory calculations for PBE and HSE have been done by Lorenzen *et al.* [84, 85] and for vdW-DF and vdW-DF2 by Knudson *et al.* [83]. First evidence of solid metallic hydrogen by Dias and Silvera [73]. Quantum Monte Carlo (QMC) simulations by Mazzola *et al.* [86].

models predict the PPT to occur at high temperatures with critical points between 10 000 K and 20 000 K, see e.g. Ref. [88, 89] and references therein. These models treat atoms, molecules, ions, and electrons as separate species (the chemical picture [87]) and calculate their ionisation and dissociation equilibrium using the law of mass action [90, 91]. This is in contrast to the physical picture, where atoms, molecules, and ions are systems consisting of only nuclei and electrons, that form bound states [87]. Chemical models that include Pauli blocking show a significantly smaller critical temperature of 6 450 K [92]. All chemical models also predict the IMT to be accompanied by a first-order phase transition, i.e. a density discontinuity, see e.g. Ref. [93] for a detailed review. In recent years, simulations based on density functional theory (DFT) and quantum Monte Carlo (QMC) methods (in the physical picture) have shown that the insulating molecular fluid transforms to an atomic metallic liquid, resulting in a first-order liquid-liquid insulator-to-metal

transition (LL-IMT) [84, 94]. In Fig. 1.2.1, the phase diagram of hydrogen shows a variety of theoretical predictions for the LL-IMT obtained with DFT (green lines and symbols) and QMC (violet circles and line) [86]. This figure shows only a few selected results. More calculations are available in the literature [94–96]. DFT calculations rely on suitable approximations for the exchange-correlation (XC) functional, for which many different exist, see Sec. 2.2.4 in Ch. 2. All of these functionals yield different results for the LL-IMT. In Fig. 1.2.1, the shown XC functionals used by different authors are PBE [97], HSE [98, 99], vdW-DF¹ (van der Waals density functional) [100], and vdW-DF2 [101]. The critical temperatures predicted by these functionals are much smaller than those of the chemical models. The vdW-DF and vdW-DF2 calculations [83] include nuclear quantum effects (NQE), which have been shown to shift the IMT to lower pressures by 35 GPa at 1 200 K [86, 96, 102]. The shown PBE, HSE, and QMC data do not contain NQE and would need to be corrected. DFT and QMC calculations yield metallisation pressures that differ by up to 1.5 Mbar.

Various experiments have been carried out to identify the LL-IMT. Laser-heated DAC experiments by the group around Dzyabura *et al.* [78], Ohta *et al.* [79], and Zaghou *et al.* [80] are consistent with each other. If NQE were added to the QMC and HSE results, they would be shifted towards the DAC data. PBE calculations using path integral molecular dynamics (PIMD) have been shown to yield lower pressures than the DAC experiments [102]. The IMTs predicted by both vdW density functionals are at much higher pressures than the DAC data. Dynamic compression experiments reporting a continuous metallisation transition have been performed by Weir *et al.* [81]. These data reveal a drop in resistivity at 1.4 Mbar to a value typical for liquid metals. The corresponding temperature was calculated to be 2 600 K with an uncertainty of 30%. The most recent dynamic compression experiments² have been done by Knudson *et al.* [83]. They used reverberating shocks followed by ramp compression, that allowed for a quasi-isentropic compression. Metallization pressures determined in this experiment are at 3 Mbar, which are much higher compared to any of the DAC experiments. The vdW density functionals show metallisation pressures in agreement with this experiment. Still, the slopes of the IMT obtained with DFT, QMC, and DAC experiments are consistent with each other, while the slope of the Knudson experiment is much steeper. Due to the contradict-

¹The van der Waals density functional is usually abbreviated by vdW-DF, but is also referred to as vdW-DF1 and vdW-DF-04 in contrast to its revised version vdW-DF2.

²More recent experiments done at the National Ignition Facility have been shown at several conferences but are yet unpublished.

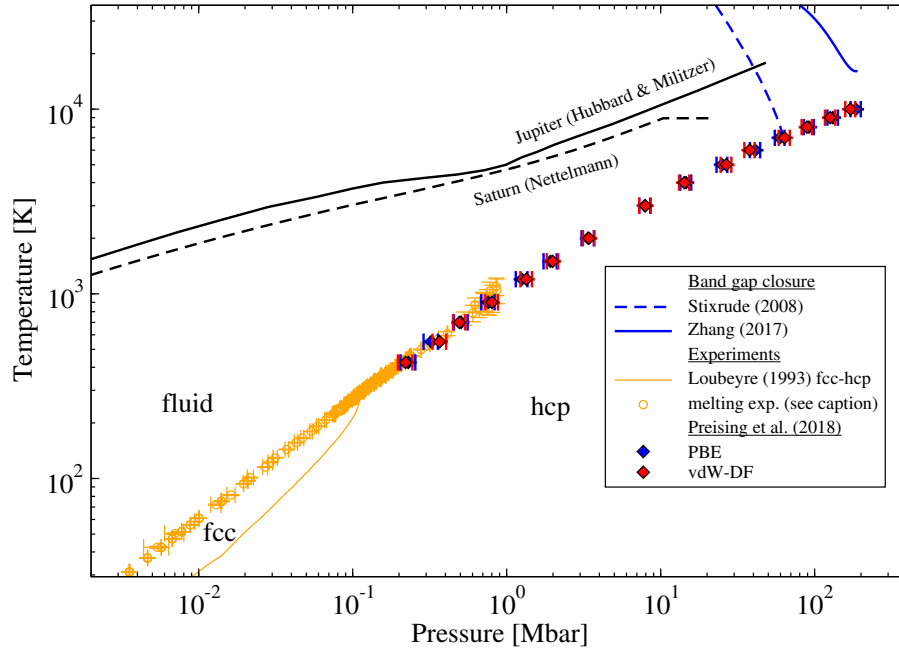


Figure 1.2.2: Helium phase diagram. Orange circles combine various experiments on the melting line of He [103–110] and the orange line shows the fcc-hcp transition [111]. Band gap calculations shown as solid blue line [112] and dashed blue line [113]. Black solid line is the preliminary Jupiter model of Hubbard and Militzer [114]. Black dashed line is the Saturn model of Nettelmann *et al.* [115]. Blue and red diamonds are two-phase simulations for the melting line done by Preising *et al.* [116]. Figure reprinted from Preising *et al.* [116] and modified with permission from Martin Preising.

ing experimental results and contradicting theoretical calculations, no satisfactory answer can be given regarding the phase boundary of the first order LL-IMT now. However, beyond the critical point, continuous metallisation has been measured precisely using Hugoniot experiments [117].

The metallisation of hydrogen is predicted to occur also in H-He mixtures [65] and has been proposed to be the driving force for H-He separation, which will be discussed in the following sections. It is unclear if a possible metallisation of He leads to remixing. However, helium remains in an insulating state up to much higher pressures and temperatures than hydrogen [59] and is most likely insulating under Jovian core conditions [118]. The exact conditions, under which helium becomes metallic, are subject to current research [112, 113, 119]. In Fig. 1.2.2, the high-pressure phase diagram of He is shown. Blue dashed and solid lines show predictions for the closure

of the band gap [112, 113] and the black dashed line is the Jupiter model by Hubbard and Militzer [114]. Even if their Jupiter model overlaps with the prediction by Stixrude *et al.* [113], He is most likely insulating at Jovian core conditions, because the employed DFT calculations underestimate the band gap. This in turn results in too low metallisation pressures, see Ref. [120] for a discussion of the band gap problem in DFT. The calculation of Zhang *et al.* [112] shows band gap closure at even higher pressures with no overlap of the Jupiter model. The melting line of He has been experimentally determined by various authors [103–110], collectively shown as orange dots. Two-phase simulations [121] based on DFT molecular dynamic simulations for the determination of the melting line have been performed by Preising *et al.* [116] using the PBE and the vdW density functionals and agree well with the experiments. According to these calculations, He will be liquid in the entire interiors of Jupiter and Saturn. It will be shown later that the melting line of He has direct implications for the miscibility diagram of H-He mixtures.

1.3 Miscibility gap of H-He mixtures

Experimental results on the miscibility gap of H-He mixtures are sparse and restricted to the low-pressure region [122–125]. These results have been obtained using diamond anvil cells to compress H-He mixtures up to 0.12 Mbar at room temperature [122]. For the solar He concentration, demixing was found to occur at ~ 0.06 Mbar, see Fig. 1.3.1. Recently, similar experiments have been done for pressures up to 0.75 Mbar at room temperature showing new structural changes in the binary phase diagram [126]. However, no demixing experiments relevant for the interiors of Jupiter and Saturn have been published up to now.³ Experiments are challenging for a number of reasons: standard Hugoniot experiments, where a material is shock-compressed using gas guns, magnetically driven flyer plates, or lasers, most likely do not enter the demixing region because temperature rises rapidly above the proposed demixing temperatures. A possible alternative is to precompress H-He to 0.7 g/cm^3 , from where phase separation within a single shock would be possible [127]. Complications also arise from the miscibility diagram at low temperatures, see Fig. 1.3.1. For the solar He abundance, the liquid hydrogen starts to solidify at 0.06 Mbar with helium remaining in the fluid phase. This results in demixing and

³First results on the miscibility of H-He mixtures at planetary interior conditions have been presented at scientific conferences, but unfortunately remain unpublished to date. The experiments were performed by Brygoo, Loubeyre, Collins, and others using laser-driven shocks on precompressed targets. These results will not be discussed here.

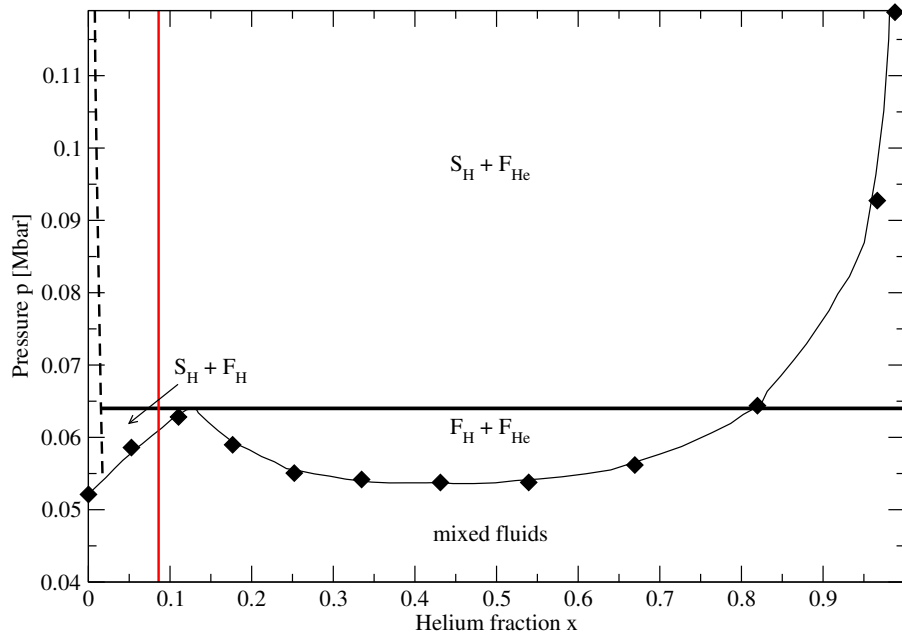


Figure 1.3.1: Experimentally determined miscibility gap of H-He mixtures at room temperature. Diamonds are direct visualizations within diamond anvil cells and lines are inferred from Raman measurements, both performed by Loubeyre *et al.* [122]. The solar He abundance $x = 0.086$ is marked by the vertical red line. The dashed line is the limit for miscibility in the solid. S_H is a H-rich solid, F_H a H-rich fluid, and F_{He} a He-rich fluid.

prevents the construction of a mixed initial state. The behaviour is similar under cryogenic conditions. To avoid rapidly rising temperatures in Hugoniot experiments, techniques like reverberating shock-waves and ramp compression could be combined similarly to the metallisation experiments by Knudson *et al.* [83] for pure hydrogen. In contrast to experiments, many theoretical predictions are available in the literature using various methods [58, 65, 85, 128–136]. Early analytical calculations assumed the ions of both species to be fully pressure-ionised and treated the electron gas perturbatively [58, 129, 130]. This approximation is not valid because Helium is most likely in an insulating state even at conditions typical for Jupiter’s core as seen in the previous section. The first predictions based on density functional theory have been made by Klepeis *et al.* [132] using the local density approximation (LDA) [137]. The accuracy of the obtained results was insufficient due to the neglect of thermal lattice effects. Later, Pfaffen-zeller *et al.* [128] performed the first DFT calculations coupled to classical molecular dynamics (MD) based on the Car-Parinello approach [138]. However, they concluded that the excess free energy at

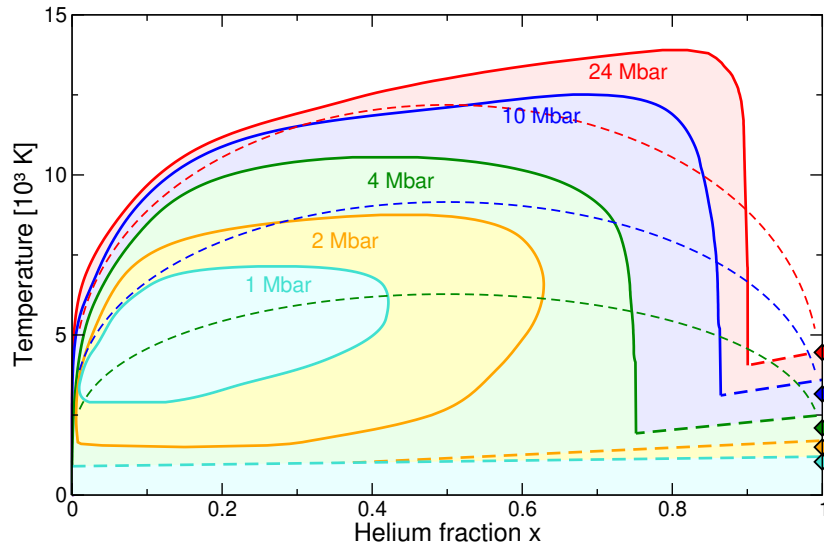


Figure 1.3.2: Miscibility diagram of H-He mixtures as calculated by Lorenzen [85]. Solid lines and coloured area correspond to the colour-coded pressures. Thick dashed lines are estimates for the liquidus line. Thin dashed lines are results from Pfaffenzeller *et al.* [128]. Diamonds show the melting temperature of He [116] for the colour-coded pressures.

finite temperatures up to 3000 K is not different from the excess energy at 0 K, so that they used their zero-temperature calculations together with the ideal entropy of mixing to derive a phase diagram for H-He mixtures at temperatures up to 12000 K. Lorenzen *et al.* [65, 85, 134] performed the first DFT-MD calculations for all considered temperatures and volumes using gradient corrections of the electron density incorporated in the Perdew-Burke-Ernzerhof (PBE) functional [97]. These results are shown in Fig. 1.3.2. The coloured regions correspond to the given pressures. Also shown are results by Pfaffenzeller *et al.* [128] for 4 Mbar, 10 Mbar, and 24 Mbar as thin dashed lines. In contrast to the data of Lorenzen *et al.*, the Pfaffenzeller *et al.* demixing temperatures are lower and symmetric with respect to the helium fraction x . The data of Lorenzen *et al.* show a significant asymmetry with respect to (w.r.t.) x : The demixing temperatures drop sharply at high He fractions for pressures greater than 4 Mbar. It has been shown by Lorenzen *et al.* [134], that the demixing temperatures approach the melting temperatures of pure He for increasing He fractions. The demixing regions show island structures for lower pressures, because they are well-separated from the respective liquidus lines. It has been demonstrated at 1 Mbar and 2 Mbar [65] that the metallisation of the hydrogen subsystem coincides with the demixing regions. Thus, it has been proposed

that the IMT in the H subsystem triggers the immiscibility of H-He mixtures. Vorberger *et al.* [139] and Morales *et al.* [135] have shown that molecular correlations in H increase due to the presence of He atoms, thus, effectively preventing the delocalization of the hydrogen electrons. This effect limits the demixing region at high He-fractions, such that higher pressure is required to metallise the H subsystem at constant temperature and increasing He-fractions. It also explains the sharp drop in demixing temperature.

Demixing calculations by Klepeis *et al.* [132], Pfaffenzeller *et al.* [128] and Lorenzen *et al.* [65, 134] approximated the entropy using only the ideal entropy of mixing. It will be shown in Ch. 4 that this is a rather crude approximation and not valid under most conditions relevant for H-He demixing under planetary interior conditions. Morales *et al.* [135, 136] performed DFT-MD simulations in the same way as Lorenzen *et al.*, but were the first to include also non-ideal effects in the entropy of mixing. Unfortunately, the authors did not present a complete miscibility diagram. Their data are only available for the solar He abundance, and are shown in Fig. 1.3.3 together with the Lorenzen *et al.* data, Jupiter [114, 140–143] and Saturn [115] isentropes, as well as selected phase lines from the hydrogen and helium phase diagram. Comparing the Lorenzen *et al.* and Morales *et al.* data reveals significant changes in the miscibility phase diagram. For temperatures greater than 5 000 K, the Morales *et al.* data show lower demixing temperatures up to 1 500 K compared to the Lorenzen *et al.* data. At pressures below 2 Mbar, the Lorenzen *et al.* miscibility diagram shows island structures, see Fig. 1.3.2, resulting in a negative slope of the demixing temperatures as function of pressure. The location of the demixing phase boundary is close to the PBE LL-IMT line shown in Fig. 1.2.1, but slightly shifted to higher pressures. This underlines the role of the LL-IMT in the hydrogen subsystem as a trigger for demixing. The shift of the LL-IMT in hydrogen to higher pressures is caused by the presence of He atoms, as discussed earlier, and has been demonstrated by Vorberger *et al.* [139], in the PhD thesis of Lorenzen [85], and in recent QMC calculations by Mazzola *et al.* [86]. The Morales *et al.* data, however, show a completely different low-temperature behaviour: The demixing pressure decreases monotonically for decreasing pressure and reproduces calculations of Schouten *et al.* [133], who performed Monte Carlo simulations in the Gibbs ensemble [144] using effective pair-potentials. The extrapolation of the Schouten *et al.* data to lower pressures is consistent with the experiments by Loubeyre *et al.* [122]. Demixing at these pressures cannot be explained by the LL-IMT in the H subsystem. Instead, the non-ideal contribution to entropy must be responsible for the phase separation, but the exact mechanism is unclear.

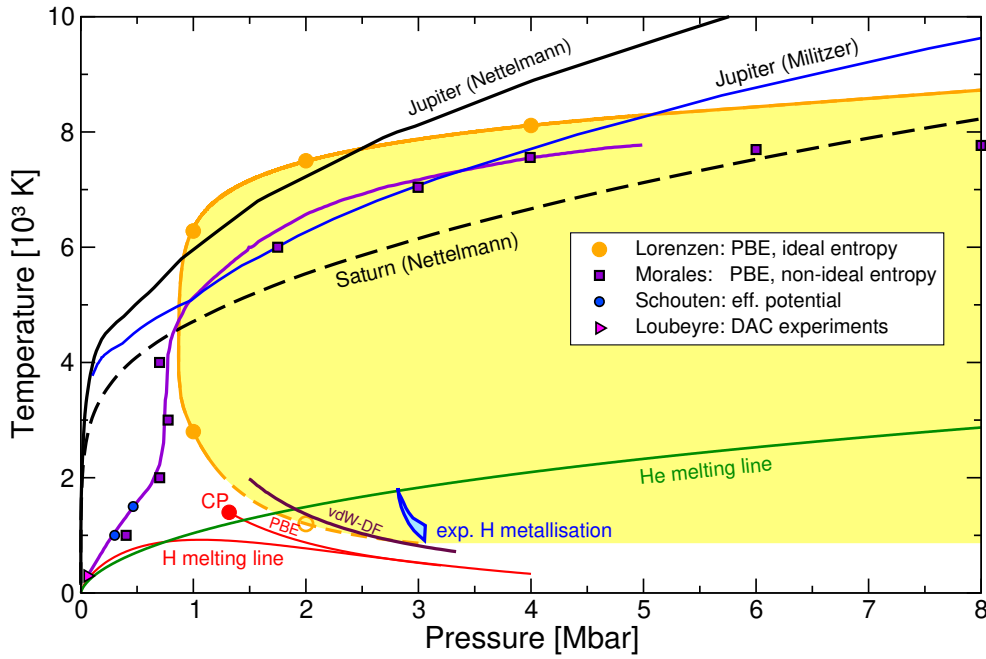


Figure 1.3.3: Miscibility diagram for solar He abundance. The coloured area corresponds to the results of Fig. 1.3.2. DFT-MD data by Morales *et al.* [135, 136] (purple squares), Monte Carlo data by Schouten *et al.* [133] (small blue circles) and experimental diamond anvil cell results by Loubeyre [122] are shown. Jupiter and Saturn isentropes by Nettelmann *et al.* from Ref. [140] and [115], respectively. Jupiter isentrope by Militzer *et al.* [114, 141–143]. He melting line from two-phase DFT-MD simulations by Preising and Redmer [116].

The lower demixing temperatures of the Morales *et al.* data have direct consequences for planetary models of Jupiter. Phase separation of H-He mixtures in Jupiter occurs if the planetary isentrope intersects with the demixing phase diagram. For the isentrope calculated by Nettelmann [140], this is only the case for the Lorenzen *et al.* phase diagram, but not for the Morales *et al.* data. However, a much cooler Jupiter model has been suggested by Militzer *et al.* [114, 141–143], that still intersects with the Morales *et al.* phase diagram. For Saturn, the shown isentrope is significantly cooler than the Jupiter adiabats and intersects with all demixing predictions. Püstow *et al.* [61] performed inhomogeneous evolution calculations for Saturn to determine the cooling as a function of time. Homogeneous evolution calculations, that do not incorporate H-He demixing, predict much shorter ages than the age of our solar system (4.56 Gyr). Püstow *et al.* showed that phase separation in Saturn starts at an age of roughly 1 Gyr using the demixing phase diagram of

Lorenzen *et al.* [65, 134]. After that, the cooling is slowed down significantly and the present-day effective temperature is reached after 5.8 Gyr. However, as seen from the Morales *et al.* data, demixing temperatures should be significantly lower when the non-ideal entropy is considered. Püstow *et al.* lowered the demixing temperatures of Lorenzen *et al.* by 1300 K to mimic this effect, and found good agreement with the age of the solar system. This artificial shift had to be performed since no entire data set of the miscibility diagram was available for the Morales *et al.* data.

1.4 Motivation and outline of this thesis

Making better predictions of Saturn’s cooling behaviour requires knowledge of the complete miscibility diagram for arbitrary He fractions. It has been shown in the previous section that the non-ideal entropy has to be taken into account in order to reproduce demixing at low pressures which is not driven by the metallisation transition but by the entropy itself. Calculating the non-ideal entropy in order to obtain a complete miscibility diagram is one of the two main objectives for this thesis. The second objective is to improve the equation of state data, required for demixing calculations, by performing DFT simulations using an XC-functional that offers a more appropriate description of hydrogen, helium, and their interaction than PBE. Previous DFT calculations of the miscibility diagram used LDA [145] or PBE [97] to approximate the exchange-correlation effects. In Sec. 1.2, it has been shown that the location of the metallisation transition is different for every XC-functional. The PBE functional shows metallisation at lower pressures than the DAC experiments, if NQE are taken into account. Functionals including van der Waals effects show higher metallisation pressures than the DAC experiments but are in better agreement with the ramp compression data by Knudson *et al.* [83]. Since it has been shown that metallisation in the H subsystem is responsible for the demixing of H and He at high pressures (see Sec. 1.3), the chosen functional will also influence the demixing phase diagram. However, comparing experiments on the LL-IMT to the DFT calculations using different XC-functionals does not offer a final answer on which functional is best suited for H-He mixtures. Even for high-precision Hugoniot experiments with deuterium it has been shown, that no functional exists that describes the data best [146].

Nevertheless, Clay *et al.* [147] performed an extensive benchmarking study on H-He mixtures, where many DFT XC-functionals have been compared to highly precise Quantum Monte Carlo calculations. They found that the vdW-DF and BLYP functional describe the enthalpy of H-He mixtures best. Minimising errors in the en-

enthalpy is crucial when calculating phase equilibria and demixing properties as will be shown in Sec. 2.5. Since the vdW-DF has been able to describe the LL-IMT better compared to the Knudson *et al.* experiments, the choice fell on this functional.

In this thesis, the calculation of a new miscibility diagram for H-He mixtures, which includes the non-ideal entropy and uses the vdW density functional of Dion *et al.* [100], will be outlined. In Ch. 2, the theoretical basics and numerical tools, that have been used in this thesis, will be described. Starting with an explanation of density functional theory and the coupling to molecular dynamics, the theory behind XC-functionals, that include van der Waals effects, will be discussed. Additionally, it will be shown how demixing is calculated for binary mixtures and how nuclear quantum effects can be treated in a post-processing step. A major part of Ch. 2 will be dedicated to the calculation of entropy within molecular dynamics. Especially the so-called coupling-constant integration will be explained. In the following chapters, the main results of this thesis will be presented. Most results have already been published in Ref. [148] and [149]. There is a publication on the phase diagram of carbon at high pressures [150] that has been calculated as part of this PhD project, but is not contained in this thesis. In Ch. 3, the equation of state obtained with the vdW-DF will be shown and compared to PBE calculations. In Ch. 4, the entropy of H-He mixtures is presented. Different methods to obtain the entropy will be compared. In Ch. 5, the results from Ch. 3 and 4 will be used to calculate the Gibbs free energy of mixing for H-He mixtures. Nuclear quantum corrections will be added to the Gibbs free energy in this chapter. In Ch. 6, the miscibility diagram of H-He mixtures will be presented and discussed with respect to earlier predictions by Lorenzen *et al.* [65, 134] and Morales *et al.* [136]. New planetary pressure–temperature profiles for Jupiter and Saturn will be calculated and compared to the miscibility diagram in Ch. 7. Finally, this thesis is concluded in Ch. 8, which summarises the obtained results and offers an outlook towards future work.

Chapter 2

Methods

This chapter illustrates the theoretical approaches and tools used to obtain the results in Ch. 3 to 7. In the first section, it is shown how the Schrödinger equation for a system of electrons and nuclei can be decoupled into an electronic part and a nuclear part. The former is treated within density functional theory (DFT) and is explained in the second section. Special attention is given to the non-local van-der-Waals functional and its contribution to the total energy. The third section briefly discusses the coupling of DFT to classical molecular dynamics (MD) simulation. In Sec. 2.5 the thermodynamics of binary systems and the equations used to determine phase separation are given. It is shown how the DFT-MD data can be used to obtain demixing properties. The third section introduces methods to obtain or approximate the total entropy, where especially the calculation of the ionic entropy is the main difficulty. In the last section, numerical details about the performed simulations are given.

2.1 Many-body Schrödinger equation

The properties and evolution of a many-body quantum system consisting of N nuclei with coordinates $\{\mathbf{R}_I\}$ and N_e electrons with coordinates $\{\mathbf{r}_i\}$ are given by the solution to the time-dependent Schrödinger equation [151, 152]

$$i\hbar \frac{\partial}{\partial t} \psi(\{\mathbf{r}_i\}, \{\mathbf{R}_I\}, t) = \hat{H} \psi(\{\mathbf{r}_i\}, \{\mathbf{R}_I\}, t), \quad (2.1.1)$$

where i is the imaginary unit, \hbar is the reduced Planck constant, ψ is the total wave function and t is the time. The Hamiltonian \hat{H} is a sum of the kinetic energy operator of the nuclei \hat{T}_n , the kinetic energy operator of the electrons \hat{T}_e , the Coulomb potential energy between nuclei and nuclei \hat{V}_{n-n} , the Coulomb potential energy be-

tween nuclei and electrons \hat{V}_{n-e} , and the Coulomb potential energy between electrons and electrons \hat{V}_{e-e} :

$$\hat{H} = \hat{T}_n + \hat{T}_e + \hat{V}_{n-n} + \hat{V}_{n-e} + \hat{V}_{e-e}. \quad (2.1.2)$$

The individual terms are defined as:

$$\hat{T}_n = - \sum_I \frac{\hbar^2}{2m_I} \nabla_I^2, \quad (2.1.3)$$

$$\hat{T}_e = - \sum_i \frac{\hbar^2}{2m_e} \nabla_i^2, \quad (2.1.4)$$

$$\hat{V}_{e-e} = \frac{1}{4\pi\epsilon_0} \sum_{i<j} \frac{e^2}{|\mathbf{r}_i - \mathbf{r}_j|}, \quad (2.1.5)$$

$$\hat{V}_{n-n} = \frac{1}{4\pi\epsilon_0} \sum_{I<J} \frac{Z_I Z_J e^2}{|\mathbf{R}_I - \mathbf{R}_J|}, \quad (2.1.6)$$

$$\hat{V}_{n-e} = - \frac{1}{4\pi\epsilon_0} \sum_{i,I} \frac{Z_I e^2}{|\mathbf{r}_i - \mathbf{R}_I|}, \quad (2.1.7)$$

where m_e is the electron mass, m_I is the mass of the nucleus I , ϵ_0 is the vacuum permittivity, and Z_I the charge number of the nucleus I . The electrons are much lighter than the nuclei and their wave functions can be partially decoupled from each other using the Born-Oppenheimer approximation [153]. The electronic Schrödinger equation for fixed nuclear coordinates is then [152]

$$\hat{H}_e \phi_k(\{\mathbf{r}_i\}, \{\mathbf{R}_I\}) = E_k \phi_k(\{\mathbf{r}_i\}, \{\mathbf{R}_I\}), \quad (2.1.8)$$

where the orthonormal set of electronic eigenstates ϕ_k depends only parametrically on the position of the nuclei and the eigenstate k has the corresponding energy eigenvalue E_k . The electronic Hamiltonian is given by

$$\hat{H}_e = \hat{T}_e + \hat{V}_{e-e} + \hat{V}_{n-e} + \hat{V}_{n-n} = \hat{T}_e + \hat{V}_{e-e} + \hat{V}_{\text{ext}}, \quad (2.1.9)$$

where $\hat{V}_{\text{ext}} = \hat{V}_{n-e} + \hat{V}_{n-n}$ is the external potential. Using the electronic eigenstates, the wave function ψ can be expanded [154] as:

$$\psi(\{\mathbf{r}_i\}, \{\mathbf{R}_I\}, t) = \sum_k \chi_k(\{\mathbf{R}_I\}, t) \phi_k(\{\mathbf{r}_i\}, \{\mathbf{R}_I\}), \quad (2.1.10)$$

where χ_k are the nuclear wave functions, which can be viewed as time-dependent expansion coefficients [152]. Inserting this ansatz into Eq. (2.1.1) using Eq. (2.1.8) and integrating out the electronic coordinates yields [152]

$$i\hbar \frac{\partial}{\partial t} \chi_k = \left(- \sum_I \frac{\hbar^2}{2M_I} \nabla_I^2 + E_k \right) \chi_k + \sum_n C_{kn} \chi_n, \quad (2.1.11)$$

where the dependence of χ_k on the nuclear coordinates and time has been dropped for convenience and

$$C_{kn} = \int \phi_k^* \left(- \sum_I \frac{\hbar^2}{2M_I} \nabla_I^2 \right) \phi_n d\mathbf{r} + \frac{1}{M_I} \sum_I \left(\int \phi_k^* i\hbar \nabla_I \phi_n d\mathbf{r} \right) i\hbar \nabla_I. \quad (2.1.12)$$

This term describes the non-adiabatic coupling between the nuclear system and the electronic system. In the Born-Oppenheimer approximation, this term is neglected such that

$$i\hbar \frac{\partial}{\partial t} \chi_k = \left(- \sum_I \frac{\hbar^2}{2M_I} \nabla_I^2 + E_k \right) \chi_k. \quad (2.1.13)$$

Thus, the potential $E_k = E_k(\{\mathbf{R}_I\})$ determines the nuclear motion and requires the solution to the electronic Schrödinger equation. In the next section, density functional theory is discussed as a way to determine the electronic eigenstates of Eq. (2.1.8).

2.2 Density functional theory (DFT)

Density functional theory in its initial formulation [137, 145] is a method to express the ground state energy and other ground state observables of the electronic quantum system as a functional of the electron density. It is based on the Hohenberg-Kohn theorems that are explained in the first subsection. The major advantage of DFT is the reduction of the dimensionality from $3N_e$ electron coordinates to three spatial coordinates of the electron density $n = N_e/V$, where N_e is the number of electrons and V is the volume. The second subsection gives details about the Kohn-Sham formalism that allows the actual calculation of ground-state properties with a tractable numerical scheme. The extension to finite temperature is detailed in Sec. 2.2.3. In subsections 2.2.4 and 2.2.5 the approximations for the exchange-correlation functional are explained and special attention is paid to the inclusion of non-local correlation. In the last subsection, periodic boundary conditions, plane waves and pseudopotentials are explained, which are important for the numerical implementation of DFT.

2.2.1 Hohenberg-Kohn theorems

The Hohenberg-Kohn theorems [137] are crucial for the understanding of density functional theory and will be briefly described here. The first theorem of Hohenberg

and Kohn proves that the electronic problem is fully determined by the external potential because there is a one-to-one correspondence between the external potential and the wave function, which determines the electron density $n(\mathbf{r})$,

$$n(\mathbf{r}) = N \int d\mathbf{r}_2 \dots \int d\mathbf{r}_{N_e} |\phi_0(\{\mathbf{r}_i\})|^2. \quad (2.2.1)$$

In particular, two potentials, \hat{V}_{ext} and \hat{V}'_{ext} , that correspond to the same electron density can only differ by a constant, i.e.

$$\hat{V}_{\text{ext}} = \hat{V}'_{\text{ext}} + \text{const.} \quad (2.2.2)$$

This one-to-one correspondence can be used to formulate ground state observables as a functional of the electron density. For an arbitrary ground state operator \hat{O} one can write

$$O[n] = \langle \hat{O}[n] \rangle = \langle \phi_0[n] | \hat{O} | \phi_0[n] \rangle, \quad (2.2.3)$$

where $\phi_0[n]$ means the wave function that yields the electron density n . The energy as functional of the density can then be formulated as

$$E[n] = \langle \phi_0[n] | \hat{H} | \phi_0[n] \rangle = \langle \phi_0[n] | \hat{T}_e + \hat{V}_{e-e} + \hat{V}_{\text{ext}} | \phi_0[n] \rangle. \quad (2.2.4)$$

The ground state density n_0 that yields the ground state energy E_0 can be found by applying the Rayleigh-Ritz variational principle [137]:

$$E_0[n_0] = \min_n E[n]. \quad (2.2.5)$$

This is the second Hohenberg-Kohn theorem. Unfortunately, the explicit form of the energy functional is not known so that the minimization can not be performed. However, Kohn and Sham in 1965 [145] reformulated the electronic problem within an efficient scheme that can be used in computer simulations. This formalism will be presented in the next section.

2.2.2 Kohn-Sham formalism

The aim of the Kohn-Sham formalism [145] is to map the fully interacting system of electrons onto a system of non-interacting particles in an effective potential that yields the same ground state density as the original system. This approach separates the N -particle problem into N one-particle problems and leads to a computationally more feasible scheme similar to the Hartree-Fock formalism [155]: the Hamilton operator H_s for a non-interacting system can be written as (the operator hats are omitted hereafter):

$$H_s = T_s + V_s, \quad (2.2.6)$$

where T_s and V_s are the kinetic energy and the external potential, respectively. For a non-interacting system, the Schrödinger equation separates into one-particle equations of the form [156]

$$\left\{ -\frac{\hbar^2}{2m_e} \nabla^2 + v_s(\mathbf{r}) \right\} \tilde{\phi}_i(\mathbf{r}) = \varepsilon_i \tilde{\phi}_i(\mathbf{r}), \quad (2.2.7)$$

where $\tilde{\phi}_i(\mathbf{r})$ are one-particle wave functions, the Kohn-Sham orbitals, and ε_i is the energy eigenvalue for each electron i . The electron density is then defined as

$$n(\mathbf{r}) = \sum_{i=1}^{\infty} \theta_i |\tilde{\phi}_i(\mathbf{r})|^2, \quad (2.2.8)$$

where the occupation number is:

$$\theta_i = \begin{cases} 1 & , \text{ if } \varepsilon_i < E_F, \\ 0 & , \text{ else,} \end{cases} \quad (2.2.9)$$

where E_F is the Fermi energy. The key objective is to find an external potential $v_s(\mathbf{r})$, defined via

$$V_s = \int d\mathbf{r} n(\mathbf{r}) v_s(\mathbf{r}), \quad (2.2.10)$$

that reproduces the same electron density as the interacting system. The ansatz of Kohn and Sham was an energy functional similar to Eq. (2.2.4) that had the following form:

$$E[n] = T_s + E_H[n] + E_{\text{ext}}[n] + E_{\text{xc}}[n]. \quad (2.2.11)$$

The first term is the kinetic energy of the non-interacting system and can be defined in terms of the one-particle wave functions:

$$T_s = \sum_{i=1}^{\infty} \theta_i \int d\mathbf{r} \tilde{\phi}_i^*(\mathbf{r}) \frac{-\hbar^2}{2m_e} \nabla^2 \tilde{\phi}_i(\mathbf{r}). \quad (2.2.12)$$

The second term is the Hartree energy of two classical charge densities:

$$E_H[n] = \frac{1}{2} \frac{e^2}{4\pi\epsilon_0} \int d\mathbf{r} \int d\mathbf{r}' \frac{n(\mathbf{r})n(\mathbf{r}')}{|\mathbf{r} - \mathbf{r}'|}. \quad (2.2.13)$$

The third term is the energy of the external potential:

$$E_{\text{ext}}[n] = V_{\text{ext}} = \int d\mathbf{r} v_{\text{ext}}(\mathbf{r}) n(\mathbf{r}). \quad (2.2.14)$$

The last term $E_{\text{xc}}[n]$ is the unknown exchange-correlation energy that contains the difference of the non-interacting system to the fully interacting system.

The energy functional, Eq. (2.2.11), yields the ground state energy for the ground state density n_0 . If a small variation δn is applied to the ground state density such that

$$n = n_0 + \delta n, \quad (2.2.15)$$

then the variational principle can be applied to Eq. (2.2.11) in combination with Eq. (2.2.7) so that the following equation is obtained [156]:

$$0 = \int d\mathbf{r} \left\{ v_s(\mathbf{r}) - \frac{e^2}{4\pi\epsilon_0} \int d\mathbf{r}' \frac{n_0(\mathbf{r}')}{|\mathbf{r} - \mathbf{r}'|} - v_{\text{ext}}(\mathbf{r}) - \frac{\delta E_{\text{xc}}[n]}{\delta n(\mathbf{r})} \Big|_{n=n_0} \right\} \delta n(\mathbf{r}). \quad (2.2.16)$$

Thus, the external potential $v_s(\mathbf{r})$, also known as the Kohn-Sham potential v_{KS} , can be identified as

$$v_s(\mathbf{r}) = v_{\text{KS}}(\mathbf{r}) = v_{\text{ext}}(\mathbf{r}) + v_{\text{H}}[n_0(\mathbf{r})] + v_{\text{xc}}[n_0(\mathbf{r})], \quad (2.2.17)$$

with the Hartree potential

$$v_{\text{H}}[n(\mathbf{r})] = \frac{e^2}{4\pi\epsilon_0} \int d\mathbf{r}' \frac{n(\mathbf{r}')}{|\mathbf{r} - \mathbf{r}'|} \quad (2.2.18)$$

and the exchange-correlation potential

$$v_{\text{xc}}[n(\mathbf{r})] = \frac{\delta E_{\text{xc}}[n]}{\delta n(\mathbf{r})}. \quad (2.2.19)$$

Substituting Eq. (2.2.17) into Eq. (2.2.7) results in the Kohn-Sham equation

$$\left\{ -\frac{\hbar^2}{2m_e} \nabla^2 + v_{\text{ext}}(\mathbf{r}) + v_{\text{H}}[n(\mathbf{r})] + v_{\text{xc}}[n(\mathbf{r})] \right\} \tilde{\phi}_i(\mathbf{r}) = \epsilon_i \tilde{\phi}_i(\mathbf{r}). \quad (2.2.20)$$

Solving the Kohn-Sham equation requires an initial guess for the one-particle wave functions. From these, the initial density is calculated via Eq. (2.2.8), which determines the Kohn-Sham potential, Eq. (2.2.17). The Kohn-Sham equation is then solved yielding new wave functions from which a new electron density can be calculated. This cycle is repeated self-consistently until the energy, Eq. (2.2.14) is minimized. Up to this point, density functional theory and the Kohn-Sham formalism is an exact theory, but in practice the exchange-correlation functional E_{xc} is still unknown. Approximations to E_{xc} are needed and will be discussed in Sec. 2.2.4. In the next section the important extension to finite temperatures will be shown.

2.2.3 Extension to finite temperatures

Initially, DFT was developed as a theory for systems at temperature $T = 0$. Mermin [157] showed that DFT can be extended to finite temperatures. He proved that

for a given temperature and chemical potential no two external potentials can lead to the same ground state density when the grand canonical ensemble is used. In the Kohn-Sham formalism [145] the energy as a functional of the electron density is replaced by the free energy $F[n]$

$$F[n] = E[n] - TS[n], \quad (2.2.21)$$

where $S[n]$ is the entropy consisting of an ideal part S_{id} and an unknown exchange-correlation part S_{xc} :

$$S[n] = S_{\text{id}} + S_{\text{xc}}[n]. \quad (2.2.22)$$

The ideal part can be written as [158]

$$S_{\text{id}} = -k_{\text{B}} \sum_{i=1}^{\infty} [f_i \ln f_i + (1 - f_i) \ln(1 - f_i)], \quad (2.2.23)$$

where f_i is the Fermi-Dirac-distribution

$$f_i = \frac{1}{\exp\{\beta(\varepsilon_i - \mu)\} + 1}. \quad (2.2.24)$$

Here, μ is the chemical potential and $\beta = (k_{\text{B}}T)^{-1}$, where k_{B} is the Boltzmann constant and T is the temperature. Further, the occupation number θ_i , which was a step function in Eq. (2.2.9), is replaced by the Fermi-Dirac-distribution f_i in Eq. (2.2.8):

$$n(\mathbf{r}) = \sum_{i=1}^{\infty} f_i |\tilde{\phi}_i(\mathbf{r})|^2. \quad (2.2.25)$$

The exchange-correlation energy E_{xc} is replaced by the exchange-correlation free energy F_{xc} . Up to now, it has been common to use the zero-temperature exchange-correlation energy E_{xc} also in finite-temperature calculations so that

$$F_{\text{xc}} \approx E_{\text{xc}}. \quad (2.2.26)$$

The development of exchange-correlation functionals for the free energy beyond this approximation is an active field of research [159–169]. Smith *et al.* [170] showed for the analytical model of a Hubbard dimer that the zero-temperature approximation is generally a good approximation for moderate temperatures and weak correlations. For highly correlated systems, errors stemming from the zero-temperature exchange-correlation functional are expected to be larger than the error due to the neglect of thermal effects [170]. Thus, it appears that the choice of a proper ground-state exchange-correlation functional is more important than finite-temperature corrections.

2.2.4 Exchange-correlation functionals

In this section, zero-temperature exchange-correlation functionals will be discussed, which are also used throughout all computations carried out for this thesis. Methods beyond the local density approximation and generalised gradient approximation, i.e. hybrid functionals and meta-GGAs, are only briefly acknowledged, because they play a minor part in this work. More important for this thesis are functionals that incorporate non-local correlation. A separate section will be dedicated to these functionals, see Sec. 2.2.5.

The exact, universal XC functional is not known, so that good approximations are needed in order to perform DFT calculations with sufficient accuracy. The simplest way to approximate E_{xc} is the local density approximation (LDA) [137]. If the electron density is only weakly varying in space it can be assumed to be locally homogeneous, such that:

$$E_{xc}^{LDA}[n] = \int n(\mathbf{r}) \epsilon_{xc}^{\text{hom}}[n(\mathbf{r})] d\mathbf{r}, \quad (2.2.27)$$

where $\epsilon_{xc}^{\text{hom}}$ is the homogeneous exchange-correlation energy. It is split into an exchange part and a correlation part:

$$\epsilon_{xc}^{\text{hom}} = \epsilon_x^{\text{hom}} + \epsilon_c^{\text{hom}}, \quad (2.2.28)$$

where

$$\epsilon_x^{\text{hom}}[n] = -\frac{e^2}{4\pi\epsilon_0} \frac{3}{4} \sqrt{\frac{3n}{\pi}} \quad (2.2.29)$$

is the result for a homogeneous electron gas [171]. The correlation energy ϵ_c^{hom} has been accurately determined by Ceperley and Alder [172] using Monte Carlo simulations and also by other authors [173, 174]. Despite LDA being the simplest approximation, it performs surprisingly well for many systems. This is especially true for the spin-dependent formulation of DFT, where the local spin density approximation improves ionisation potentials, dissociation energies and cohesive energies [175]. The success of LDA is based on the fulfilment of exact constraints that can be derived for the exchange-correlation functional: the two-particle probability (the probability to find an electron at any position \mathbf{r} , given that there is another electron at \mathbf{r}') is defined as

$$P(\mathbf{r}, \mathbf{r}') = N_e(N_e - 1) \int d\mathbf{r}_3 \dots d\mathbf{r}_{N_e} |\phi(\{\mathbf{r}_i\})|^2. \quad (2.2.30)$$

Compared to the two-particle probability in the uncorrelated case, $P_{\text{uncorr}}(\mathbf{r}, \mathbf{r}') = n(\mathbf{r})n(\mathbf{r}')$, the exchange-correlation contribution creates a so-called exchange-correlation hole with density $n_{xc}(\mathbf{r}, \mathbf{r}')$, which corresponds to a reduced probability of finding

two electrons close to each other. The probability can be rewritten in terms of $n_{xc}(\mathbf{r}, \mathbf{r}')$ as

$$P(\mathbf{r}, \mathbf{r}') = n(\mathbf{r})n(\mathbf{r}') + n(\mathbf{r})n_{xc}(\mathbf{r}, \mathbf{r}'). \quad (2.2.31)$$

The exact constraints on $n_{xc}(\mathbf{r}, \mathbf{r}')$ are [176]

$$\int d\mathbf{r} n_{xc}(\mathbf{r}, \mathbf{r}') = -1 \quad \forall \mathbf{r}', \quad (2.2.32)$$

$$\int d\mathbf{r} n_x(\mathbf{r}, \mathbf{r}') = -1 \quad \forall \mathbf{r}', \quad (2.2.33)$$

$$\int d\mathbf{r}, n_c(\mathbf{r}, \mathbf{r}') = 0 \quad \forall \mathbf{r}', \quad (2.2.34)$$

where $n_{xc} = n_x + n_c$. Further the exchange part n_x has to fulfil

$$n_x(\mathbf{r}, \mathbf{r}) = -n(\mathbf{r})/2, \quad (2.2.35)$$

$$n_x(\mathbf{r}, \mathbf{r}') \leq 0. \quad (2.2.36)$$

The LDA fulfils these important conditions exactly [177]. The next step towards a better XC functional is to include also the gradient of the density. This can be done by expanding the exchange energy for slowly varying densities, but it has been shown, that such a gradient expansion approximation (GEA) violates the properties of the exchange-correlation hole [178]. Perdew and Wang [179] developed the generalised gradient approximation (GGA), which improves the GEA significantly because it satisfies the exchange-correlation hole properties. Exchange functionals of the GGA type have the form

$$E_x^{\text{GGA}}[n] = \int n(\mathbf{r}) \epsilon_x^{\text{hom}}[n] F_x(s(\mathbf{r})) d\mathbf{r}, \quad (2.2.37)$$

where

$$s(\mathbf{r}) = \frac{|\nabla n|}{2k_F n}, \quad (2.2.38)$$

is the dimensionless reduced gradient, $k_F = \sqrt[3]{3\pi^2 n}$ is the Fermi wave vector, and $F_x(s)$ is the exchange enhancement factor. Many different GGA functionals exist in the literature, e.g. PW86 [179] PW91 [180], PBE [97], AM05 [181], BLYP [182], and more [183–185]. Among these, PBE is one of the most widely used GGA functionals because it fulfils all the exact constraints that LDA fulfils [186] and it has no empirical parameters.

Further degrees of freedom can be added to GGA when also the kinetic energy density [156]

$$\tau = \frac{\hbar^2}{2m_e} \sum_i f_i \left| \nabla \tilde{\phi}_i \right|^2 \quad (2.2.39)$$

is used. These functionals are called meta-GGAs, where the exchange energy can be written as

$$E_x^{\text{meta-GGA}}[n] = \int n(\mathbf{r}) \epsilon_x^{\text{hom}}[n] F_x(s, \tau) d\mathbf{r}. \quad (2.2.40)$$

Examples for meta-GGAs are TPSS [187], revTPSS [188], and SCAN [189].

In Hartree-Fock (HF) theory, the exchange energy of the one-particle states is calculated exactly. Eventually, this led to the idea to couple HF exchange with density functional theory to obtain the best of both worlds [190]. This was first achieved by Becke [191] and provided the starting point for the so-called hybrid functionals. These mix the HF exchange energy with the usual GGA exchange in a certain fraction. Hybrid functionals were able to better predict atomisation energies, ionisation potentials and proton affinities of molecules [191], and to generally improve the band gap of many systems compared to standard GGA functionals [192].

2.2.5 Non-local correlation and van der Waals density functionals

The LDA and GGA XC functionals do not incorporate long-range, non-local contributions to correlation [193]. Yet, these are necessary to accurately describe van der Waals (vdW) forces. Numerous methods have been devised to account for van der Waals effects [100, 101, 193–208]. The extension of DFT using pairwise vdW potentials has been attempted by, e.g., Grimme *et al.* [201, 204, 205] and by Tkatchenko *et al.* [206–208] (TS and TS-MBD method). True non-local density functionals have been constructed by Rydberg *et al.* [196, 198], Dion *et al.* [100, 199], and Vydrov and van Voorhis [202, 203].

In this section, the theory behind the van der Waals density functional (vdW-DF, sometimes also referred to as vdW-DF1 or vdW-DF-04) [100] will be outlined. The aim is to give a comprehensive review of the steps and approximations needed to derive the vdW-DF. This section will recite the major progress made by Langreth, Lundqvist, and the members of their groups based on Refs. [100, 101, 193–200].

The functional used in this work is the vdW-DF by Dion *et al.* [100]. Starting point for the construction of exchange-correlation functionals is the adiabatic connection formula (ACF), which is a coupling-constant integration from a non-interacting reference system to a fully interacting one. The exchange-correlation energy E_{xc} can be expressed in terms of the exchange-correlation hole $n_{xc}^\lambda(\mathbf{r}, \mathbf{r}')$ (see section 2.2.4)

as

$$E_{\text{xc}} = \int_0^1 d\lambda \iint d\mathbf{r} d\mathbf{r}' \frac{n(\mathbf{r}) n_{\text{xc}}^\lambda(\mathbf{r}, \mathbf{r}')}{|\mathbf{r} - \mathbf{r}'|}, \quad (2.2.41)$$

where λ is a coupling parameter. Note that atomic units are used in this subsection. The equation can be reformulated using the generalisation of Eq. (2.2.31) to arbitrary λ values, i.e.,

$$P_\lambda(\mathbf{r}, \mathbf{r}') = n(\mathbf{r})n(\mathbf{r}') + n(\mathbf{r})n_{\text{xc}}^\lambda(\mathbf{r}, \mathbf{r}'), \quad (2.2.42)$$

as

$$E_{\text{xc}} = \int_0^1 d\lambda \iint d\mathbf{r} d\mathbf{r}' \frac{P_\lambda(\mathbf{r}, \mathbf{r}') - n(\mathbf{r})n(\mathbf{r}')}{|\mathbf{r} - \mathbf{r}'|}. \quad (2.2.43)$$

Using the fluctuation dissipation theorem (FDT), the 2-body probability $P_\lambda(\mathbf{r}, \mathbf{r}')$ can be connected to the response function $\chi_\lambda(\mathbf{r}, \mathbf{r}', t=0)$ and it can be shown [194, 195, 199] that

$$\chi_\lambda(\mathbf{r}, \mathbf{r}', t=0) = \int_{-\infty}^{\infty} \frac{d\omega}{2\pi i} \chi_\lambda(\mathbf{r}, \mathbf{r}', \omega) = P_\lambda(\mathbf{r}, \mathbf{r}') - n(\mathbf{r})n(\mathbf{r}') + \delta(\mathbf{r} - \mathbf{r}')n(\mathbf{r}), \quad (2.2.44)$$

where the response function χ_λ is defined via

$$\delta n_\lambda(\mathbf{r}, \omega) = \int d\mathbf{r}' \chi_\lambda(\mathbf{r}, \mathbf{r}', \omega) \phi_{\text{ext}}^\lambda(\mathbf{r}', \omega), \quad (2.2.45)$$

where δn_λ is the change in density introduced by an external potential $\phi_{\text{ext}}^\lambda$. Inserting Eq. (2.2.44) into Eq. (2.2.43) one arrives at

$$E_{\text{xc}} = - \int_0^1 d\lambda \int_0^\infty \frac{du}{2\pi} \text{Tr} [\chi_\lambda \tilde{V}] - E_{\text{self}}, \quad (2.2.46)$$

where $\tilde{V} = \tilde{V}(\mathbf{r} - \mathbf{r}') = \frac{1}{|\mathbf{r} - \mathbf{r}'|}$. The last term $E_{\text{self}} = \int d\mathbf{r} n(\mathbf{r}) \tilde{V}(0)$ is the self energy, that diverges but should be cancelled exactly by a corresponding counterpart in the first term. The frequency $\omega = iu$ has been used to shift the contour of the integral [199]. The response function χ_λ of an external potential $\phi_{\text{ext}}^\lambda$ can be connected to the response function $\tilde{\chi}_\lambda$ of the total potential $\phi_{\text{tot}}^\lambda$ via

$$\chi_\lambda = \tilde{\chi}_\lambda + \tilde{\chi}_\lambda \lambda \tilde{V} \chi_\lambda, \quad (2.2.47)$$

where $\tilde{\chi}$ is defined via

$$\delta n_\lambda(\mathbf{r}, \omega) = \int d\mathbf{r}' \tilde{\chi}_\lambda(\mathbf{r}, \mathbf{r}', \omega) \phi_{\text{tot}}^\lambda(\mathbf{r}', \omega). \quad (2.2.48)$$

The coupling-constant integration in Eq. (2.2.46) can be performed when Eq. (2.2.47) is inserted and the full potential approximation (FPA) [100, 200], i.e. $\tilde{\chi}_\lambda = \tilde{\chi}_1 = \tilde{\chi}$, is applied:

$$E_{\text{xc}} = - \int_0^\infty \frac{du}{2\pi} \text{Tr} \left[\ln \left(1 - \tilde{\chi} \tilde{V} \right) \right] - E_{\text{self}}. \quad (2.2.49)$$

The FPA neglects spectator excitations, i.e. the influence of the polarisability of a distant object on $\tilde{\chi}$, but yields the correct vdW asymptote for large separations [200]. If the FPA is applied to a uniform system, the exchange-correlation energy would be given by

$$E_{\text{xc}}^0 = - \int_0^\infty \frac{du}{2\pi} \text{Tr} [\ln \epsilon] - E_{\text{self}}, \quad (2.2.50)$$

where ϵ is the dielectric function of a homogeneous system. Subtracting the homogeneous electron gas contribution from Eq. (2.2.49) gives the non-local correlation energy

$$E_{\text{c}}^{\text{nl}} = - \int_0^\infty \frac{du}{2\pi} \text{Tr} \left[\ln \left(1 - \tilde{\chi} \tilde{V} \right) - \ln \epsilon \right]. \quad (2.2.51)$$

This splitting of the total exchange-correlation energy, i.e.,

$$E_{\text{xc}} = E_{\text{xc}}^0 + E_{\text{c}}^{\text{nl}}, \quad (2.2.52)$$

is key for density functionals, which incorporate non-local correlations. Using this convention, the non-local part vanishes for homogeneous systems by construction. Importantly, this form is not limited to the treatment of well-separated fragments, e.g. molecules far away from each other, but is able to treat close molecules with overlapping densities. Instead of using Eq. (2.2.50) for the local contribution, the vdW-DF uses a combination of the Zhang-Yang revPBE exchange [183] and LDA correlation, because the FPA would not be appropriate, since it was designed specifically to accurately describe asymptotic, non-local vdW effects. It has been shown that the exchange part of most GGAs introduces binding for rare-gas atoms [209]. Since this should be solely a correlation effect, the vdW-DF uses the revPBE exchange, which does not introduce binding in these cases.

The non-local correlation energy E_{c}^{nl} has to be further approximated to enable a tractable computation scheme. This is done by expanding Eq. (2.2.51) to second order in $\check{S} = 1 - \epsilon^{-1}$ which results in

$$E_{\text{c}}^{\text{nl}} = - \int_0^\infty \frac{du}{4\pi} \text{Tr} \left[\check{S}^2 - \left(\frac{\nabla \check{S} \cdot \nabla \tilde{V}}{4\pi e^2} \right)^2 \right]. \quad (2.2.53)$$

In a plane-wave representation, Dion *et al.* [100, 199] make the ansatz

$$\check{S}_{\mathbf{q},\mathbf{q}'} = \frac{1}{2} \left[\tilde{S}_{\mathbf{q},\mathbf{q}'} + \tilde{S}_{-\mathbf{q},-\mathbf{q}'} \right], \quad (2.2.54)$$

where \mathbf{q} and \mathbf{q}' are wave vectors and

$$\tilde{S}_{\mathbf{q},\mathbf{q}'} = \int d\mathbf{r} e^{-i(\mathbf{q}-\mathbf{q}')\cdot\mathbf{r}} \frac{\omega_p^2}{[\omega_q(\mathbf{r}) + \omega][\omega_q(\mathbf{r}) - \omega]}, \quad (2.2.55)$$

$$\omega_p = \sqrt{4\pi n}, \quad (2.2.56)$$

$$\omega_q(\mathbf{r}) = \frac{q^2}{2m_e \left(1 - e^{-\frac{4\pi q^2}{9q_0(\mathbf{r})^2}} \right)}, \quad (2.2.57)$$

$$q_0(\mathbf{r}) = k_F(\mathbf{r}) \left(1 - \frac{Z_{ab}}{9} (s(\mathbf{r}))^2 \right). \quad (2.2.58)$$

The function $q_0(\mathbf{r})$ with parameter $Z_{ab} = -0.8491$ determines the scale on which ω_q switches from its low- \mathbf{q} to large- \mathbf{q} limits. Its form and parameters represent the local density approximation with gradient corrections. The choice of $\check{S}_{\mathbf{q},\mathbf{q}'}$ is similar to a plasmon pole approximation, where the excitation energy as function of wave vector interpolates between plasmon excitations at low \mathbf{q} (long wavelengths) and electron-hole excitations which go as $q^2/2m_e$ for large \mathbf{q} [199]. Furthermore, the f-sum rule is respected because $\check{S}_{\mathbf{q},\mathbf{q}'} \rightarrow - (4\pi e^2/m_e \omega^2) n$ for large ω [100]. Also the large- \mathbf{q} limit is reproduced, that gives the right self-correlation, and the resulting exchange-correlation hole integrates to -1 as required by Eq. (2.2.32). The vdW-DF is a pure density functional, in the sense that it relies only the electronic density n and its gradient, which enter via ω_p and ω_q , and no other empirical quantities. Thus, in a more general way, the non-local correlation energy can be written as [100]

$$E_c^{\text{nl}} = \frac{1}{2} \int d\mathbf{r} d\mathbf{r}' n(\mathbf{r}) \Phi(\mathbf{r}, \mathbf{r}') n(\mathbf{r}'), \quad (2.2.59)$$

where $\Phi(\mathbf{r}, \mathbf{r}')$ is the vdW-kernel that is a given function depending on the electron densities n at positions \mathbf{r} and \mathbf{r}' , and $\mathbf{r} - \mathbf{r}'$. It has been shown, that Eq. (2.2.53) can be recast into this form [199]. The exact formula is not reprinted here. However, for large separations $R = |\mathbf{r} - \mathbf{r}'|$ the asymptotic form of $\Phi(\mathbf{r}, \mathbf{r}')$ is [100, 199]

$$\Phi(\mathbf{r}, \mathbf{r}') = -\frac{1}{R^6} \frac{C}{q_0(\mathbf{r})^2 q_0(\mathbf{r}')^2 (q_0(\mathbf{r})^2 + q_0(\mathbf{r}')^2)}, \quad (2.2.60)$$

where $C = 12 (4\pi/9)^3 m_e e^4$. The asymptotic form of $\Phi(\mathbf{r}, \mathbf{r}')$ decays with R^{-6} as expected from the usual expression for the asymptotic van der Waals potential [210]. In hydrogen, local energy differences and potential energy surfaces, especially close

to metallisation are best reproduced with the vdW-DF in comparison to QMC simulations [211]. Also in hydrogen-helium mixtures, the vdW-DF has been shown to give best performance with respect to enthalpies for all mixing ratios [147]. Yet, the pressure is overestimated compared to QMC simulations. However, the vdW-DF has been tested on the S22¹ [212] data set with moderate success [213] and solids [214] with less success.

Further developments of the vdW-DF method have been done by Lee *et al.* [101] (vdW-DF2). They use a different underlying exchange functional (rPW86) and change the parameter Z_{ab} to -1.887, altering the gradient expansion of the local density approximation used in Eq. (2.2.58). It has been realized by Klimeš *et al.* [214, 215] that the accuracy of the vdW-DF method can be optimized by selecting a different exchange functional. They proposed several functionals which decreased the mean absolute deviation on the S22 data set to below chemical accuracy (1 kcal/mol).

2.2.6 Periodic boundary conditions, plane waves and pseudopotentials

The simulation of macroscopic systems within DFT is numerically not possible. Instead, periodic boundary conditions are introduced, where the original simulation cell is periodically continued in every space direction. This periodicity implies the periodicity of the Kohn-Sham potential $V^{\text{KS}} = \int d\mathbf{r} v^{\text{KS}}(\mathbf{r})n(\mathbf{r})$, i.e.

$$V^{\text{KS}}(\mathbf{r}) = V^{\text{KS}}(\mathbf{r} + \mathbf{L}), \quad (2.2.61)$$

where \mathbf{L} is the lattice vector. The Kohn-Sham orbitals are thus described by Bloch functions [152, 216]

$$\tilde{\phi}_i(\mathbf{r}, \mathbf{k}) = u_i(\mathbf{r}, \mathbf{k})e^{i\mathbf{r}\cdot\mathbf{k}}, \quad (2.2.62)$$

where \mathbf{k} is a vector in reciprocal space restricted to the first Brillouin zone. In turn, the periodicity of the Kohn-Sham potential results in periodicity of the Bloch factor $u_i(\mathbf{r}, \mathbf{k})$ and the Kohn-Sham orbitals:

$$u_i(\mathbf{r}, \mathbf{k}) = u_i(\mathbf{r} + \mathbf{L}, \mathbf{k}), \quad (2.2.63)$$

$$\tilde{\phi}_i(\mathbf{r}, \mathbf{k}) = \tilde{\phi}_i(\mathbf{r} + \mathbf{L}, \mathbf{k}). \quad (2.2.64)$$

The exact numerical solution to the Kohn-Sham equation requires the Bloch factors to be expanded in a complete, orthonormal basis set. Here, plane waves are used

¹The S22 data set contains molecules which contain important non-covalent bonds.

for that purpose and the Kohn-Sham orbitals become [152]

$$\tilde{\phi}_i(\mathbf{r}, \mathbf{k}) = \frac{1}{\sqrt{V}} \sum_{\mathbf{G}} c_i(\mathbf{G}, \mathbf{k}) e^{i(\mathbf{G}+\mathbf{k})\mathbf{r}}, \quad (2.2.65)$$

where \mathbf{G} are reciprocal space vectors and $c_i(\mathbf{G}, \mathbf{k})$ are the expansion coefficients. The infinite sum over \mathbf{G} has to be truncated in numerical calculations. A cutoff energy E_{cutoff} is introduced such that only \mathbf{G} vectors are included that satisfy

$$\frac{\hbar^2}{2m_e} |\mathbf{G} + \mathbf{k}|^2 \leq E_{\text{cutoff}}. \quad (2.2.66)$$

The calculation of, e.g., electron density and energy requires an integral over wave vectors \mathbf{k} in the first Brillouin zone [152]. However, wave vectors that are close to each other contain similar information [216] so that the integration over \mathbf{k} -space can be reduced to a weighted sum over a few discrete \mathbf{k} -points. Convergence w.r.t. E_{cutoff} and the amount of \mathbf{k} -points has to be checked and the values used in this thesis are denoted in Sec. 2.7.

The expansion of the Kohn-Sham orbitals into plane waves requires large E_{cutoff} to reproduce the strong oscillations of the wave function near the core. In fact, the required cutoff energies increase the cost for DFT-MD simulations beyond feasibility for many applications. To overcome this limitation, pseudopotentials are used [152, 216]. They replace the wave function in a certain sphere with radius r_c around the nucleus with a smooth, node-free wave function. This reduces the number of \mathbf{G} vectors needed to achieve convergence of the basis set. The use of pseudopotentials for the core electrons is valid because they do not contribute significantly to binding energies and other observables unlike the valence electrons. In this work, Projector-Augmented-Wave (PAW) pseudopotentials [217, 218] supplied with VASP [219–221] are used, which connect the wave function to the pseudo wave function using a linear transformation. Pseudopotentials do not impact the simulation results unless two atoms are closer than the combined distance of their core radii r_c . Still, they have to be validated, e.g., by comparing pseudopotentials with different r_c or even with calculations using the Coulomb potential.

2.3 Molecular dynamics (MD)

The Newtonian equations of motion for classical point particles can be derived from Eq. (2.1.13) [152]:

$$M_I \frac{d^2}{dt^2} \mathbf{R}_I = -\nabla_I E_k(\{\mathbf{R}_I\}). \quad (2.3.1)$$

Using the Hellman-Feynman theorem, see e.g. [222], the derivative of the potential energy surface, can be calculated from the derivative of the electronic Hamiltonian as:

$$\nabla_I E_k(\{\mathbf{R}_I\}) = \int d\mathbf{r}_1 \dots \int d\mathbf{r}_{N_e} \phi_k^*(\{\mathbf{r}_i\}) \left[\nabla_I \hat{H}_e(\{\mathbf{R}_I\}) \right] \phi_k(\{\mathbf{r}_i\}). \quad (2.3.2)$$

The equations of motion are integrated numerically using an appropriate algorithm such as the Verlet algorithm [223] as implemented in VASP. For every time step, the forces on the ions need be computed in a DFT calculation. Special care has to be taken with respect to the time step of the simulation. Especially if hydrogen molecules are present, their vibrational period needs to be temporally resolved. Thus the time step needs to be sufficiently small. The simulations are initialised by having an ensemble of N atoms at certain predefined positions in a box with volume V . Periodic boundary conditions are employed. The system is generally not in equilibrium because the direction of the initial velocities is chosen randomly, while the mean kinetic energy is chosen such that the desired simulation temperature is obtained. To simulate the system at a selected temperature, i.e. in the canonical ensemble, the Nosé-Hoover thermostat [224, 225] is used. Depending on how close the initial setup was to the equilibrium conditions, the simulation has to be run for several hundred time steps before equilibrium is eventually reached. From that point on, thermodynamic averages of pressure, energy, and other quantities that can be expressed as an ensemble average, can be computed. The pressure is derived from the potential energy surface using the Virial theorem [226]. From the particle positions one can calculate distribution functions of the ions, e.g. the radial distribution function (RDF). From the velocities, the auto-correlation function can be computed of which the Fourier transformation yields the vibrational density of states (VDOS). Nuclear quantum effects are important under certain conditions and are discussed in the next section.

In classical molecular dynamics simulations with analytical force fields, it is nowadays possible to simulate hundreds of millions of particles [227, 228] using efficient algorithms and high performance computers on thousands of CPUs. In DFT-MD simulations however, the most computationally expensive part is the DFT calculation and feasible particle numbers are actually constrained by the total number of electrons. Lorenzen *et al.* performed highly demanding DFT-MD simulations on hydrogen-helium mixtures using 2048 electrons [65, 85] only for a limited number of calculations to visualise demixing directly in the simulation box. Typical DFT-MD calculations are performed using 64-512 explicitly treated electrons [15, 17, 18, 119, 134, 142, 229–231], i.e. valence electrons which are not frozen

in the pseudopotentials. Hence, convergence with respect to the particle number has to be checked.

2.4 Nuclear quantum corrections

Quantum effects for the nuclei become increasingly important for low temperatures. The explicit simulation of nuclear quantum effects (NQE) is a challenging task. Methods, which compute NQE directly during the MD simulations are Path Integral Molecular Dynamics (PIMD) [232–234] and coloured-noise thermostats based on the generalised Langevin equation (GLE) [235, 236]. PIMD simulations increase computational costs compared to DFT-MD simulations using classical nuclei by a factor of 10-100 [152] and are thus out of the scope for a large number of computations. Coloured-noise thermostats are much more feasible, which reduce the computational costs significantly compared to PIMD. Unfortunately, this type of thermostat is not implemented in the simulation package VASP and an own implementation would be out of the scope of this work. In this work, nuclear quantum corrections (NQC) were accounted for by applying post-processing procedures based on the vibrational density of states \mathcal{S} (VDOS)² [237]. The VDOS can be calculated from the velocity-autocorrelation function $\langle \mathbf{v}_\alpha(t) \cdot \mathbf{v}_\alpha(0) \rangle_{V,T}$ evaluated at given volume V and temperature T [18]:

$$\mathcal{S}(\nu, V, T) = \sum_{\alpha} x_{\alpha} \frac{4m_{\alpha}}{3k_{\text{B}}T} \int_0^{\infty} dt \cos(2\pi\nu t) \langle \mathbf{v}_{\alpha}(t) \cdot \mathbf{v}_{\alpha}(0) \rangle_{V,T}, \quad (2.4.1)$$

where ν is the frequency, \mathbf{v}_{α} are the velocities, and x_{α} and m_{α} are the particle fraction and the mass of species α , respectively. The integral of $\mathcal{S}(\nu, V, T)$ over the entire frequency range is equal to 1. The canonical partition function Q can be expressed as:

$$\ln Q = 3N \int_0^{\infty} d\nu \mathcal{S}(\nu, V, T) \ln q(\nu), \quad (2.4.2)$$

if the frequencies of the normal modes are continuously distributed. Here, $q(\nu)$ is the partition function for a mode with frequency ν . The partition function for a quantum mechanical harmonic oscillator q^{Q} is

$$q^{\text{Q}}(\nu) = \frac{\exp(-\frac{\beta h \nu}{2})}{1 - \exp(-\beta h \nu)}. \quad (2.4.3)$$

²Do not confuse the calligraphic symbol \mathcal{S} for the VDOS with the letter S used for entropy or with \tilde{S} and \check{S} as used in Sec. 2.2.5.

The partition function for a classical harmonic oscillator q^C is

$$q^C(\nu) = (\beta h \nu)^{-1}, \quad (2.4.4)$$

where h is Planck's constant. These partition functions act as weighting functions for the VDOS. From Eq. (2.4.2), (2.4.3), and (2.4.4), one can derive weighting functions for the internal energy U , free energy F , and entropy S in the quantum (superscript Q) and classical (superscript C) case for a system of harmonic oscillators. These are [237]:

$$W_U^Q(\nu) = \frac{\beta h \nu}{2} + \frac{\beta h \nu}{\exp(\beta h \nu) - 1}, \quad (2.4.5)$$

$$W_F^Q(\nu) = \ln \frac{1 - \exp(-\beta h \nu)}{\exp(-\beta h \nu/2)}, \quad (2.4.6)$$

$$W_S^Q(\nu) = \frac{\beta h \nu}{\exp(\beta h \nu) - 1} - \ln(1 - \exp(-\beta h \nu)), \quad (2.4.7)$$

$$W_U^C(\nu) = 1, \quad (2.4.8)$$

$$W_F^C(\nu) = \ln(\beta h \nu), \quad (2.4.9)$$

$$W_S^C(\nu) = 1 - \ln(\beta h \nu). \quad (2.4.10)$$

The corresponding expressions for U , F , and S in the quantum and classical case are

$$U^\gamma(V, T) = 3Nk_B T \int_0^\infty d\nu \mathcal{S}(\nu, V, T) W_U^\gamma(\nu), \quad (2.4.11)$$

$$F^\gamma(V, T) = 3Nk_B T \int_0^\infty d\nu \mathcal{S}(\nu, V, T) W_F^\gamma(\nu), \quad (2.4.12)$$

$$S^\gamma(V, T) = 3Nk_B \int_0^\infty d\nu \mathcal{S}(\nu, V, T) W_S^\gamma(\nu), \quad (2.4.13)$$

where $\gamma = \{Q, C\}$. Although the weighting functions are consistently derived from the partition functions, the given expressions for U^γ , F^γ , and S^γ are not thermodynamically consistent because the VDOS also depends on V and T [238]. In practice, this is not a serious limitation because the thermodynamic inconsistency is expected to be small. Furthermore, thermodynamically consistent energies and pressures can be calculated from $F^\gamma(V, T)$ if the obtained data is fit to a suitable, differentiable model function. However, the integrands in the formulas for free energy and entropy diverge for $\nu \rightarrow 0$ if $\mathcal{S}(0) \neq 0$, which is generally the case for liquids. Only for solids the zero-frequency contribution vanishes, because the diffusion coefficient is zero. For a single-species system, where all particles have mass m , the vibrational density of states at $\nu = 0$ is connected to the diffusion coefficient D via [237]

$$D = \frac{\mathcal{S}(0)}{4m\beta}. \quad (2.4.14)$$

The divergence can be eliminated when the classical case is subtracted from the quantum case, which then yields equations for quantum corrections (QC) of the thermodynamic quantities:

$$U^{\text{QC}} = U^{\text{Q}} - U^{\text{C}}, \quad (2.4.15)$$

$$F^{\text{QC}} = F^{\text{Q}} - F^{\text{C}}, \quad (2.4.16)$$

$$S^{\text{QC}} = S^{\text{Q}} - S^{\text{C}}. \quad (2.4.17)$$

In this thesis, only F^{QC} has been used to add quantum corrections to the free energy as a post-processing step. The VDOS can easily be calculated from the velocity auto-correlation function (VACF), which is calculated from the DFT-MD runs. In general, the system in DFT-MD simulations contains also anharmonic contributions, especially at high temperatures. Anharmonicities enter only through the VDOS $\mathcal{S}(\nu, V, T)$ since only harmonic weighting functions have been used. Thus, the quantum corrections capture anharmonic effects in an incomplete way. Furthermore, the quantum nature of rotation is not captured using this approach. Nevertheless, this technique has been successfully applied to many systems [18, 238, 239].

2.5 Thermodynamics of binary systems

In this section, the thermodynamics of binary systems, see e.g. Ref. [240], are outlined, which are needed to understand how demixing is calculated. The thermodynamic potential for a binary system such as a hydrogen-helium mixture at given temperature T , pressure p , and mole numbers \bar{n}_i ($i = 1, 2$) is the Gibbs free energy G :

$$G(\bar{n}_1, \bar{n}_2, p, T) = U(\bar{n}_1, \bar{n}_2, p, T) + pV(\bar{n}_1, \bar{n}_2, p, T) - TS(\bar{n}_1, \bar{n}_2, p, T) \quad (2.5.1)$$

$$= \bar{n}_1 \mu_1(\bar{n}_1, \bar{n}_2, p, T) + \bar{n}_2 \mu_2(\bar{n}_1, \bar{n}_2, p, T), \quad (2.5.2)$$

where U is the internal energy, V the volume, and μ_i the chemical potential. It is convenient to rewrite these equations in terms of mole fractions

$$x_i = \frac{\bar{n}_i}{\sum_i \bar{n}_i} = \frac{\bar{n}_i}{\bar{n}}, \quad (2.5.3)$$

where

$$\sum_i x_i = 1, \quad (2.5.4)$$

and

$$\sum_i \bar{n}_i = \bar{n}. \quad (2.5.5)$$

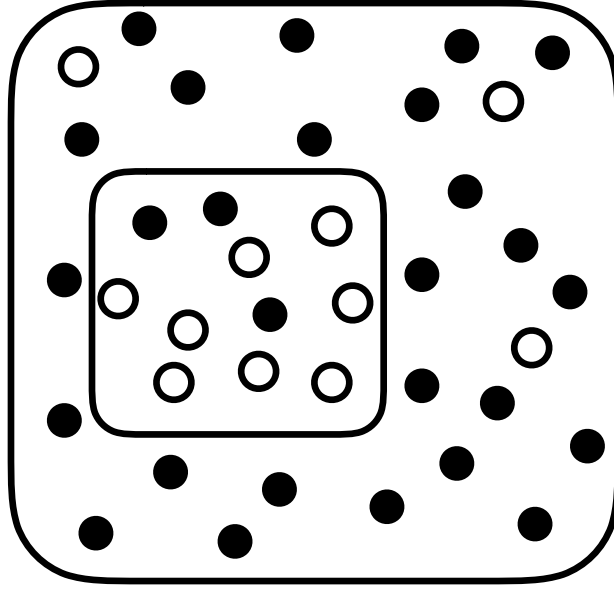


Figure 2.5.1: Schematic depiction of a demixed binary system. Closed circles are species 1 and open circles are species 2. The outer system has particle fraction $x'_2 = 1/9$ and the inner system $x''_2 = 8/11$. The overall particle fraction of species 2 is $x_2 = 11/38$.

The Gibbs free energy is then

$$G(x_2, p, T) = U(x_2, p, T) + pV(x_2, p, T) - TS(x_2, p, T), \quad (2.5.6)$$

$$\overline{G} = \frac{G(x_2, p, T)}{\bar{n}} = (1 - x_2)\mu_1(x_2, p, T) + x_2\mu_2(x_2, p, T) \quad (2.5.7)$$

$$= \mu_1(x_2, p, T) + x_2 [\mu_2(x_2, p, T) - \mu_1(x_2, p, T)], \quad (2.5.8)$$

where the dependency on both mole numbers is replaced by the mole fraction of one species. Note that the mole fraction x_i is equal to the particle fraction $N_i / \sum_i N_i$. The total differential of \overline{G} and its derivative with respect to x_2 are

$$d\overline{G} = \mu_1(x_2, p, T)dx_1 + \mu_2(x_2, p, T)dx_2 + \left. \frac{\partial \overline{G}}{\partial p} \right|_{x_i, T} dp + \left. \frac{\partial \overline{G}}{\partial T} \right|_{x_i, p} dT, \quad (2.5.9)$$

$$\left. \frac{d\overline{G}}{dx_2} \right|_{p, T} = \mu_2(x_2, p, T) - \mu_1(x_2, p, T), \quad (2.5.10)$$

where $dx_1 = -dx_2$ has been used.

Now a binary system that consists of two subsystems is considered where only the mole fractions differ. One could think of a hydrogen-helium system, where a helium-rich droplet has formed inside a hydrogen-rich environment. The first subsystem is

labelled by a dash and the second by a double dash, i.e., the mole fractions are x'_i and x''_i , see Fig. 2.5.1 for a schematic depiction. In these systems, $T' = T''$ and $p' = p''$ holds. The total differential of the molar Gibbs free energy is thus

$$d\bar{G} = \mu'_1(x_2, p, T)dx'_1 + \mu'_2(x_2, p, T)dx'_2 + \mu''_1(x_2, p, T)dx''_1 + \mu''_2(x_2, p, T)dx''_2. \quad (2.5.11)$$

The total number of particles is not allowed to change so that a change in x'_i necessarily results in a change in x''_i , which can be expressed as

$$dx'_i = -dx''_i. \quad (2.5.12)$$

Equation (2.5.11) then becomes

$$d\bar{G} = [\mu'_1(x_2, p, T) - \mu''_1(x_2, p, T)] dx'_1 + [\mu'_2(x_2, p, T) - \mu''_2(x_2, p, T)] dx'_2. \quad (2.5.13)$$

In equilibrium, the Gibbs free energy does not change and $d\bar{G}$ has to be zero, so that this equation for arbitrary dx'_i only holds if

$$\mu'_i = \mu''_i, \quad (2.5.14)$$

i.e. the chemical potentials have to be equal in both subsystems. Let us evaluate Eq. (2.5.8) for both subsystems and drop the dependencies on p and T for simplicity:

$$\bar{G}(x'_2) = \bar{G}' = \mu'_1 + (\mu'_2 - \mu'_1)x'_2 \quad (2.5.15)$$

$$\bar{G}(x''_2) = \bar{G}'' = \mu''_1 + (\mu''_2 - \mu''_1)x''_2 \quad (2.5.16)$$

Subtracting Eq. (2.5.15) from Eq. (2.5.16) yields

$$\frac{\bar{G}'' - \bar{G}'}{x''_2 - x'_2} = \mu'_2 - \mu'_1 = \left. \frac{d\bar{G}}{dx_2} \right|_{x'_2} = \mu''_2 - \mu''_1 = \left. \frac{d\bar{G}}{dx_2} \right|_{x''_2}, \quad (2.5.17)$$

where Eq. (2.5.14) and (2.5.10) have been used. Equation (2.5.17) is of major importance: it says that equilibrium concentrations can be found from \bar{G} when a common tangent is applied, where the derivatives of \bar{G} w.r.t. x_2 at the points x'_2 and x''_2 are equal. If a binary system tends to separate into two subsystems with different compositions, the mole fractions x'_i and x''_i can be determined this way. Applying this common tangent construction to the Gibbs free energy at different pressures and temperatures yields the so called binodal curve, i.e. the ensemble of x'_i and x''_i as a function of temperature or pressure. While the binodal curve corresponds to thermodynamically stable states, there are also states that can be metastable. To

determine the unstable region one has to evaluate the second derivative of the Gibbs free energy, which is negative in unstable regions, i.e.

$$\frac{\partial^2 \bar{G}}{\partial x_2^2} < 0. \quad (2.5.18)$$

The point of inflection is given by the second derivative of \bar{G} being zero and separates the stable and metastable region (convex \bar{G}) from the unstable region (concave \bar{G}). For different temperatures and pressures this condition yields the so called spinodal curve. In Fig. 2.5.2, the stable, metastable, and unstable regions are visualized for a schematic depiction of the Gibbs free enthalpy of mixing.

The same considerations also apply when the Gibbs free energy of mixing $\Delta\bar{G}(x, p, T)$ is taken into account. The index 2 is dropped hereafter so that $x = x_2$. For H-He mixtures, x is considered to be the helium fraction. The Gibbs free energy of mixing (also free enthalpy of mixing or excess free enthalpy) $\Delta\bar{G}(x, p, T)$ is defined as:

$$\Delta\bar{G}(x, p, T) = \bar{G}(x, p, T) - (1 - x) \bar{G}(0, p, T) - x \bar{G}(1, p, T). \quad (2.5.19)$$

It is more convenient to work with this quantity because it becomes zero for both $x = 0$ and $x = 1$ and is thus easier to present graphically. Equations (2.5.17) and (2.5.18) then become:

$$\frac{\Delta\bar{G}(x'', p, T) - \Delta\bar{G}(x', p, T)}{x'' - x'} = \frac{\partial \Delta\bar{G}(x, p, T)}{\partial x} \Big|_{x'} = \frac{\partial \Delta\bar{G}(x, p, T)}{\partial x} \Big|_{x''} \quad (2.5.20)$$

and

$$\frac{\partial^2 \Delta\bar{G}(x, p, T)}{\partial x^2} < 0. \quad (2.5.21)$$

In calculations, the Gibbs free energy of mixing can only be evaluated for a discrete set of He fractions. This data set can then be fitted using a suitable ansatz. In the work of Lorenzen *et al.* [134], a Redlich-Kister fit [241] was used such that

$$\Delta\bar{G}^{\text{RK}}(x) = (x^2 - x) \sum_{i=0}^k A_i (2x - 1)^i, \quad (2.5.22)$$

where k is the order of the fit and A_i are the coefficients. The factor $(x^2 - x)$ ensures that the function vanishes for $x = 0$ and $x = 1$ and the term $(2x - 1)$ was designed to be the most simple function $f(x)$ that fulfils the condition $f(x) = -f(1 - x)$, i.e. that has central symmetry with respect to the point $x = 0.5$. The Redlich-Kister fit facilitates the numerical determination of the spinodal and tangent points and has been used throughout this work.

In Fig. 2.5.2, a schematic depiction of the Gibbs free energy of mixing is shown for

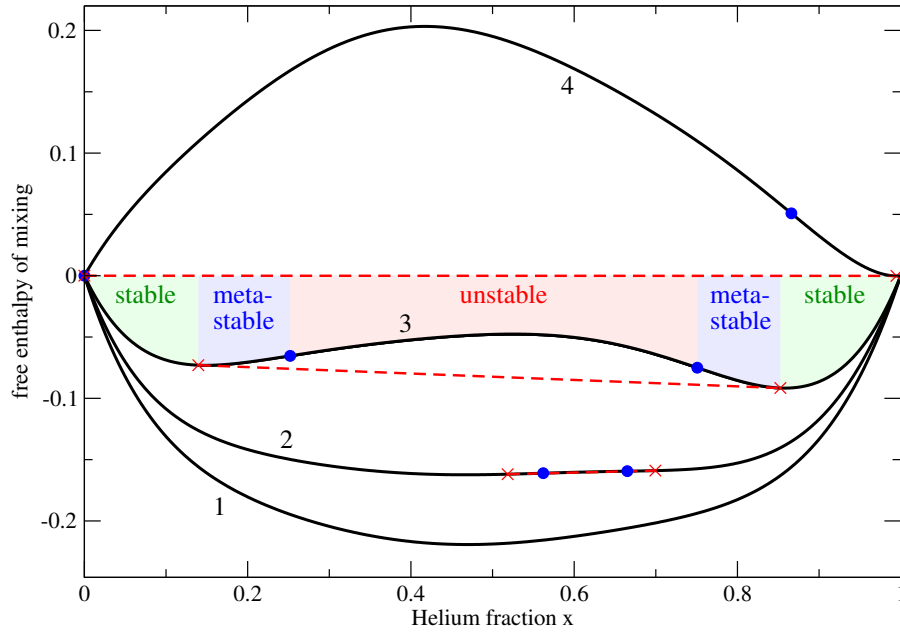


Figure 2.5.2: Schematic depiction of the Gibbs free energy of mixing (black solid curves) for different conditions labelled 1 to 4: If pressure is constant, the temperature would decrease from curve 1 to curve 4. The common tangent construction (red dashed line with crosses at the tangent points) and spinodal points (blue circles) are shown, where demixing occurs (curves 2, 3, and 4). For curve 3, the stable, metastable, and unstable x are marked as coloured region.

different conditions. If constant pressure is assumed, the black curves would show varying temperatures from hottest (curve 1) to coldest (curve 4). In general, if the temperature is increased (or pressure is decreased) the interactions between particles are weakened so that mixtures can be seen as increasingly ideal and well-mixed. In curve 1, the Gibbs free energy of mixing does not show any point of inflection, so that the system is perfectly mixed for arbitrary helium fractions. In curve 2 the temperature is decreased compared to curve 1 and a small double-well structure forms in the Gibbs free energy of mixing, such that the common tangent construction can be applied. The temperature of curve 3 is even lower than the temperature of curve 2 and the double-well structure is more pronounced. In curve 4 the Gibbs free energy of mixing is concave up to a helium fraction of $x = 0.87$ indicated by the blue circle, so that the mixture is not stable in the region $(0, 0.87)$. In general, if the curve is concave at either end of x or over the entire range, the tangent line according to Eq. (2.5.20) can not be determined. It is important to note that there always exists a finite miscibility of one species in another, so that in principle the Gibbs free energy

of mixing should show a small minimum in the vicinity of $x = 0$, $x = 1$, or both ends. In the simulations presented in this thesis, it is not computationally feasible to calculate arbitrary small helium or hydrogen fractions. Instead, a set of discrete He fractions is simulated with a certain distribution, so that the Redlich-Kister fit of this discrete set is not able to resolve miscibility at fractions smaller than the lowest He and H fractions. This, in turn, leads to cases, where the Gibbs free energy of mixing is concave over the entire range of He fractions and the existence of a tangent is mathematically not fulfilled, but should occur physically.

Similar to the Gibbs free energy of mixing, other mixing quantities can be defined. Such as the entropy of mixing Δs_{mix} , volume of mixing Δv_{mix} , energy of mixing Δu_{mix} , and enthalpy of mixing Δh_{mix} :

$$\Delta s(x, p, T) = s(x, p, T) - (1 - x) s(0, p, T) - x s(1, p, T), \quad (2.5.23)$$

$$\Delta v(x, p, T) = v(x, p, T) - (1 - x) v(0, p, T) - x v(1, p, T), \quad (2.5.24)$$

$$\Delta u(x, p, T) = u(x, p, T) - (1 - x) u(0, p, T) - x u(1, p, T), \quad (2.5.25)$$

$$\Delta h(x, p, T) = h(x, p, T) - (1 - x) h(0, p, T) - x h(1, p, T), \quad (2.5.26)$$

where $s(x, p, T)$, $v(x, p, T)$, $u(x, p, T)$, and $h(x, p, T) = u(x, p, T) + p v(x, p, T)$ are the specific entropy, volume, energy, and enthalpy per particle, respectively. The Gibbs free energy of mixing per particle $\Delta g(x, p, T)$ is similar to Eq. (2.5.19)

$$\Delta g(x, p, T) = g(x, p, T) - (1 - x) g(0, p, T) - x g(1, p, T), \quad (2.5.27)$$

where $g(x, p, T)$ is the Gibbs free energy per particle.

An interesting aspect of computing the equation of state of a binary system for various mixing ratios is the calculation of partial (molar) quantities, e.g. the partial volume. The partial volume ξ_i is defined as

$$\xi_i = \left(\frac{\partial V}{\partial N_i} \right)_{p, T, \{N_j\}}, \quad (2.5.28)$$

where V is the volume and N_i is the particle number of species i . It is important to note that ξ_i is a function of temperature T , pressure p , and particle fractions x_i . The partial volume is important, e.g., for the calculation of entropies within the formalism of Lin *et al.* [242] and Desjarlais [243] in the multi-component case - see also French *et al.* [238]. The effective particle density

$$n_i^{\text{eff}} = \frac{1}{\xi_i} = \frac{1}{V \xi_i} \sum_j N_j \xi_j \quad (2.5.29)$$

is required in these methods for binary systems, see Sec. 2.6.2 for more details on how they enter in these theories. The quantity ξ_i can numerically be evaluated by

simulating an isobaric-isothermal ensemble with different particle numbers of species i . However, such an approach is quite demanding. Instead the partial volumes are here calculated via the so called 'Method of intercepts' [244], which will be explained in the following:

In a binary system the total volume per particle $v = V/N$ is given by:

$$v(x, p, T) = (1 - x)\xi_1(x, p, T) + x\xi_2(x, p, T). \quad (2.5.30)$$

which has already been used in Eq. (2.5.29). The derivative with respect to x at constant p and T is

$$\left(\frac{\partial v(x, p, T)}{\partial x} \right)_{p, T} = \xi_2 - \xi_1 + \left(\frac{\partial \xi_2}{\partial x} - \frac{\partial \xi_1}{\partial x} \right) x + \frac{\partial \xi_1}{\partial x} \quad (2.5.31)$$

$$= \xi_2 - \xi_1 + (1 - x) \frac{\partial \xi_1}{\partial x} + x \frac{\partial \xi_2}{\partial x} \quad (2.5.32)$$

$$= \xi_2(x) - \xi_1(x), \quad (2.5.33)$$

where $(1 - x)d\xi_1 + xd\xi_2 = 0$, since the change in ξ_1 and ξ_2 is not independent when the particle fraction is changed. In other words, the slope of the specific volume as a function of particle fraction is given by the difference in partial volumes evaluated at that particle fraction. To obtain also the absolute values one considers a tangent $t(x)$, that is applied to $v(x)$ at the fraction x' . This tangent has the form

$$t(x) = [\xi_2(x') - \xi_1(x')] (x - x') + v(x'). \quad (2.5.34)$$

Inserting Eq. (2.5.30) at $x = x'$ into the tangent equation one obtains

$$t(x) = \xi_1(x') + [\xi_2(x') - \xi_1(x')] x. \quad (2.5.35)$$

Thus, the tangent construction for $v(x)$ at $x = x'$ yields the partial volumes ξ_1 at $x = 0$ and ξ_2 at $x = 1$. In Fig. 2.5.3, the method of intercepts is demonstrated for actual H-He data. The specific volume data were fitted using a second-order polynomial. The tangent and the partial volumes were then computed analytically. The curvature of $v(x)$ is small, so that the partial volumes show only a weak variation with particle fraction. In Fig. 2.5.4, the partial volumes and their ratio are given as a function of pressure for three different He fractions at a temperature of 10 000 K. The partial volumes of H and He decrease with increasing pressure in a similar way as the specific volumes of the mixture would decrease with pressure. However, the ratio of the partial volumes increases only weakly with pressure and decreases with increasing He fraction. It has been shown [135, 136] that the addition of He favours the bonding of hydrogen molecules even under conditions, where pure H

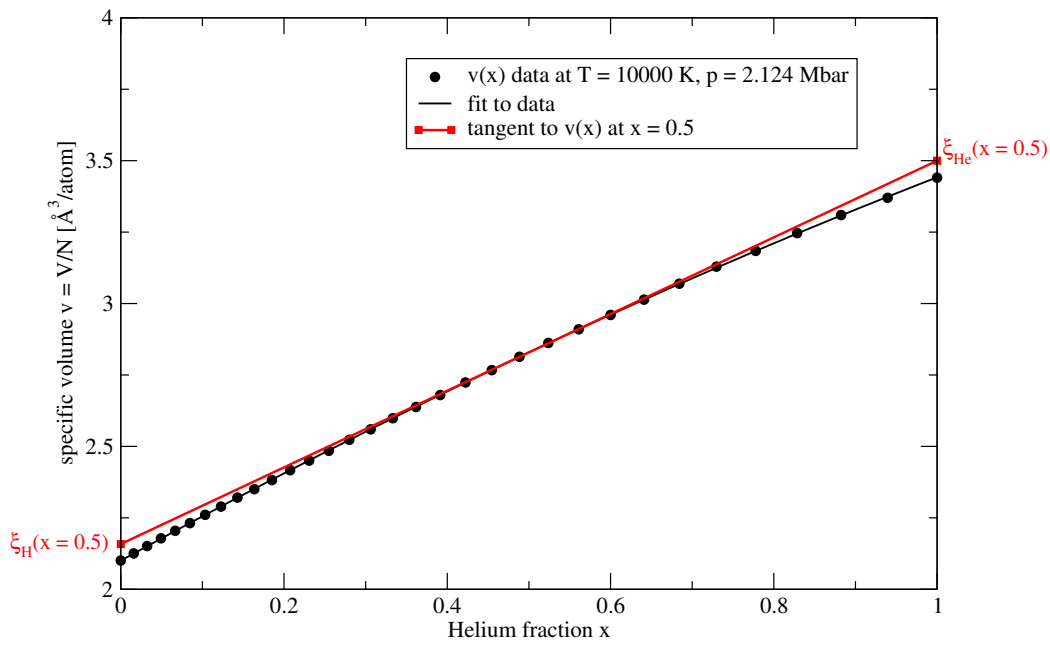


Figure 2.5.3: Method of intercepts demonstrated for H-He mixtures at a temperature of 10 000 K and a pressure of 2.124 Mbar. A tangent was constructed at He fraction $x' = 0.5$, which yields ξ_H at $x = 0$ and ξ_{He} at $x = 1$.

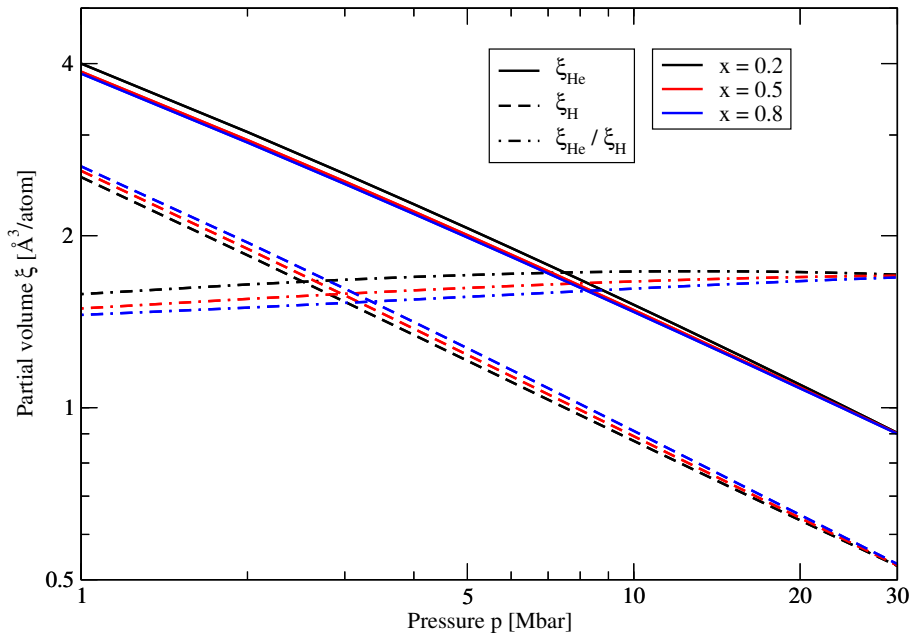


Figure 2.5.4: Partial volumes of H and He, and their ratio as a function of pressure p at a temperature of 10 000 K for three He fractions.

would be completely dissociated. Molecular hydrogen has a higher specific volume than atomic hydrogen. Thus, the partial volume of H also increases with increasing He fraction. With increasing pressure, this effect is weakened so that the ratio of partial volumes increases slightly.

2.6 Entropy

In sections 2.2 and 2.3, the determination of energy and pressure using DFT-MD simulations has been explained. The calculation of phase equilibria additionally requires knowledge of the entropy. The ideal electronic entropy is given by Eq. (2.2.23), where the XC contribution to entropy is neglected due to the lack of sophisticated finite-temperature XC functionals. The major contribution, however, is the ionic entropy. Unfortunately, it is not possible to evaluate the ionic entropy as an ensemble average within molecular dynamics. Thus, additional techniques are needed to access it. Many different methods exist to calculate or approximate the ionic entropy. In the following subsections, the most important methods are summarised and applied to hydrogen-helium mixtures.

2.6.1 Thermodynamic integration

The difference in entropy between the state of interest and a given reference state can be obtained by integrating the equation of state along thermodynamic paths [140]. If the volume V and temperature T are chosen as independent variables the integration can be performed at isochoric or isothermal conditions:

$$S(V, T) = \frac{U(V, T)}{T} + \int_{V_0}^V dV' \frac{p(T_0, V')}{T_0} + \int_{T_0}^T dT' \frac{U(T', V)}{T'^2} - \frac{F_0}{T_0}, \quad (2.6.1)$$

where $F_0 = U(V_0, T_0) - T_0 S(V_0, T_0)$ is the free energy of the reference state at volume V_0 and temperature T_0 . It contains the unknown entropy of the reference state $S(V_0, T_0)$. A similar formula can also be derived if pressure p and temperature T are chosen as independent variables, see Appendix A.1:

$$S(p, T) = \frac{U(p, T) + pV(p, T)}{T} - \int_{p_0}^p dp' \frac{V(p', T_0)}{T_0} + \int_{T_0}^T dT' \frac{U(p, T') + pV(p, T')}{T'^2} - \frac{G_0}{T_0}, \quad (2.6.2)$$

where $G_0 = U(p_0, T_0) + p_0 V(p_0, T_0) - T_0 S(p_0, T_0)$ is the Gibbs free energy of the reference state located at pressure p_0 and temperature T_0 . The required equation of state data are available from DFT-MD simulations, but the reference entropy is in principle unknown. A possible choice for the reference state is the ideal gas limit for high temperatures and/or low densities since the entropy of the ideal gas is analytically known. However, DFT-MD calculations become increasingly demanding for low densities and high temperatures especially in a plane-wave basis. Thus, the connection of DFT-MD data and the ideal gas limit is impossible on an equal theoretical description. To overcome this limitation Becker *et al.* [230] used different theoretical models to create patched, wide-range equations of state for pure hydrogen and helium from which the absolute entropy can be reconstructed using Eq. (2.6.1) or (2.6.2). The construction of such an EOS for numerous He fractions is beyond the scope of this work because it would require a wide-range EOS for 29 different He fractions. From a technical point of view, the integration over a wide range of volumes and temperatures is challenging, because the EOS data is not given analytically but on a discrete volume and temperature grid. Thus, the data has to be interpolated or fitted to a given model. If the caloric and thermal EOS are interpolated or fitted independently, they are not thermodynamically consistent, which is mandatory to apply Eq. (2.6.2). The resulting uncertainty in entropy from an inconsistent EOS will increase with the length of the integration since errors in the EOS are added along the integration path. In order to avoid performing the integration over a wide range, the calculation of high precision reference entropies at certain volumes and temperatures is inevitable. There are methods based on the calculation of the vibrational density of states derived from the velocity-autocorrelation function, which will be outlined in the next section, but the most reliable method for this purpose is coupling-constant integration, which will be explained in Sec. 2.6.3.

2.6.2 Methods based on the VDOS

In the harmonic approximation, the entropy of solids can be computed via the phonon density of states [150] or from the VDOS $\mathcal{S}(\nu)$ using appropriate weighting functions derived from the harmonic and quantum harmonic oscillators, see Sec. 2.4 and in particular Eq. (2.4.13). However, as mentioned in Sec. 2.4, these weighting functions diverge for liquids because the VDOS is finite at zero frequency ($\nu = 0$). It has been suggested by Lin *et al.* [242] that the VDOS of liquids $\mathcal{S}_\alpha(\nu)$ for species α can be interpreted as the superposition of a solid-like VDOS $\mathcal{S}_\alpha^s(\nu)$ and a gas-like VDOS $\mathcal{S}_\alpha^g(\nu)$. Here, the multi-component formulation of French *et al.* [245] will be

used, which is based on the notation of Desjarlais [243]. The VDOS for species α is, thus,

$$\mathcal{S}_\alpha(\nu) = f_\alpha^s \mathcal{S}_\alpha^s(\nu) + f_\alpha^g \mathcal{S}_\alpha^g(\nu), \quad (2.6.3)$$

where $f_\alpha^g = 1 - f_\alpha^s$ is the gas-like fraction and f_α^s is the solid-like fraction. Using an appropriate decomposition of the total power spectrum, the harmonic weighting functions can be applied to the solid-like part while a good model has to be found for the gas-like part. Lin *et al.* [242] chose a hard sphere model³ to obtain the gas-like entropy. In this formalism, the gas-like fraction is given by

$$f_\alpha^g = \gamma_\alpha^{2/5} \Delta_\alpha^{3/5}, \quad (2.6.4)$$

where the hard sphere packing fraction γ_α can be determined from the normalised diffusivities Δ_α via [243]

$$\frac{2(1 - \gamma_\alpha)^3}{2 - \gamma_\alpha} - \gamma_\alpha^{2/5} \Delta_\alpha^{3/5} = 0, \quad (2.6.5)$$

where

$$\Delta_\alpha = \frac{2}{3} \mathcal{S}_\alpha(0) \sqrt{\frac{\pi k_B T}{m_\alpha}} (n_\alpha^{\text{eff}})^{1/3} \left(\frac{6}{\pi} \right)^{2/3}, \quad (2.6.6)$$

The gas-like VDOS in the hard sphere approximation has the form

$$f_\alpha^g \mathcal{S}_\alpha^g = \frac{\mathcal{S}_\alpha(0)}{1 + \left(\frac{\pi \nu \mathcal{S}_\alpha(0)}{2 f_\alpha^g} \right)^2}. \quad (2.6.7)$$

The entropy of the solid part is then obtained as an integration over the solid-like spectrum

$$S_\alpha^s = 3N_\alpha k_B \int_0^\infty [\mathcal{S}_\alpha(\nu) - f_\alpha^g \mathcal{S}_\alpha^g] W_S^Q(\nu) d\nu, \quad (2.6.8)$$

where $W_S^Q(\nu)$ is the weighting function of a harmonic oscillator defined in Eq. (2.4.7). The weighting function for the hard sphere gas is

$$W_\alpha^{\text{HS}} = \frac{1}{3} \left\{ \frac{S_\alpha^{\text{IG}}}{k_B} + \ln \left[\frac{1 + \gamma_\alpha + \gamma_\alpha^2 - \gamma_\alpha^3}{(1 - \gamma_\alpha)^3} \right] + \frac{\gamma_\alpha (3\gamma_\alpha - 4)}{(1 - \gamma_\alpha)^2} \right\}, \quad (2.6.9)$$

where the entropy of the ideal gas S_α^{IG} is

$$\frac{S_\alpha^{\text{IG}}}{k_B} = \frac{5}{2} + \ln \left[\left(\frac{2\pi m_\alpha k_B T}{h^2} \right)^{3/2} \frac{1}{f_g n_\alpha^{\text{eff}}} \right], \quad (2.6.10)$$

³The terminology of 'hard spheres' used in the work of Lin *et al.* actually refers to a relaxation time approximation.

and the corresponding gas-like entropy is

$$S_{\alpha}^g = 3N_{\alpha}f_{\alpha}^gk_B \int_0^{\infty} \mathcal{S}_{\alpha}^g(\nu) W_{\alpha}^{\text{HS}} = 3N_{\alpha}f_{\alpha}^gk_B W_{\alpha}^{\text{HS}}. \quad (2.6.11)$$

The total entropy S is simply

$$S = \sum_{\alpha} S_{\alpha}^s + S_{\alpha}^g. \quad (2.6.12)$$

This method, named 2PT (two-phase thermodynamic), was successfully applied to Lennard-Jones fluids [242], molecular water [246], and carbon dioxide [247]. Importantly, in the multi-component formulation, the partial volumes are needed to calculate the effective particle densities n_{α}^{eff} as explained in Sec. 2.5, see also [245]. It has been shown, that the 2PT method fails for liquid metals near the melting line [243]. Desjarlais [243] has significantly improved the 2PT method by using a memory function (MF) approach [248–250] to the gas-like component. The gas-like spectrum with MF kernel $K_{\alpha}^g(\tau)$ can be written as

$$\mathcal{S}_{\alpha}^g(\nu) = 2 \left[\frac{1}{\hat{K}_{\alpha}^g(i2\pi\nu) + i2\pi\nu} + \frac{1}{\hat{K}_{\alpha}^g(-i2\pi\nu) - i2\pi\nu} \right], \quad (2.6.13)$$

where $\hat{K}_{\alpha}^g(s)$ is the Laplace transform of $K_{\alpha}^g(\tau)$. Desjarlais uses a Gaussian form of the MF kernel $K_{\alpha}^g(\tau)$ whose Laplace transform is [243]

$$\hat{K}_{\alpha}^g(s) = A_{\alpha}^g \sqrt{\frac{\pi}{4B_{\alpha}^g}} \exp \left[\frac{s^2}{4B_{\alpha}^g} \right] \text{Erfc} \left[\frac{s}{2\sqrt{B_{\alpha}^g}} \right], \quad (2.6.14)$$

where A_{α}^g and B_{α}^g are parameters and $\text{Erfc}(z)$ is the complementary error function. The parameters can be related via the zero-frequency value

$$\mathcal{S}_{\alpha}(0) = 4 \frac{f_{\alpha}^g}{A_{\alpha}^g} \sqrt{\frac{B_{\alpha}^g}{\pi}}, \quad (2.6.15)$$

and the requirement that the low-frequency behaviour is equal to that of a hard sphere system:

$$A_{\alpha}^g = 4B_{\alpha}^g / \left[2 + \sqrt{\pi \left(1 + B_{\alpha}^g \mathcal{S}_{\alpha}^2(0) / (2f_{\alpha}^g)^2 \right)} \right]. \quad (2.6.16)$$

The yet to be determined parameter B_{α}^g can be computed from the moment expansion of the autocorrelation function. However, this parameter essentially determines the high-frequency tail of the gas-like spectrum. Thus, it is possible to fit $\mathcal{S}_{\alpha}^g(\nu)$

to the high frequency tail of $\mathcal{S}_\alpha(\nu)$, because these spectra should merge for high ν [243]. It has been demonstrated that this 2PT-MF method improves the accuracy of entropies for liquid metals to within 1 %. It has also been successfully applied to superionic water [245].

The advantage of the 2PT and 2PT-MF method is that entropies can be computed from a single molecular dynamics run without the need for classical pair potentials and additional demanding simulations as in the coupling-constant approach, which will be explained next.

2.6.3 Coupling-constant integration (CCI)

Coupling-constant integration (CCI)⁴ is related to the thermodynamic integration of the equation of state, but instead of using a physical quantity such as volume, temperature, or pressure as variable one uses an artificial coupling parameter λ which connects two different interactions [251]. Let the two systems be labelled by index 0 and 1. The Hamiltonians are thus $H_0(\mathbf{r}, \mathbf{p})$ and $H_1(\mathbf{r}, \mathbf{p})$ that depend on the space coordinate $\mathbf{r} = (\mathbf{r}_1, \mathbf{r}_2, \dots, \mathbf{r}_N)$ and the momentum coordinate $\mathbf{p} = (\mathbf{p}_1, \mathbf{p}_2, \dots, \mathbf{p}_N)$ containing the coordinates of all N atoms. The Hamiltonians for both systems can be written as

$$H_j(\mathbf{r}, \mathbf{p}) = \sum_{i=1}^N \frac{\mathbf{p}_i^2}{2m_i} + V_j(\mathbf{r}), \quad (2.6.17)$$

where m_i is the mass of atom i and $V_j(\mathbf{r})$ is the potential that determines the interaction of the particles for system j . These systems can be coupled using the coupling-constant λ as

$$H(\lambda) = (1 - \lambda)H_0 + \lambda H_1, \quad (2.6.18)$$

$$= \sum_{i=1}^N \frac{\mathbf{p}_i^2}{2m_i} + V_0 + \lambda(V_1 - V_0), \quad (2.6.19)$$

$$= \sum_{i=1}^N \frac{\mathbf{p}_i^2}{2m_i} + V(\lambda), \quad (2.6.20)$$

where

$$V(\lambda) = V_0 + \lambda(V_1 - V_0). \quad (2.6.21)$$

Using this coupling, the system switches linearly from V_0 at $\lambda = 0$ to V_1 at $\lambda = 1$. The dependences on \mathbf{p} and \mathbf{r} have been dropped from the notation for convenience.

⁴It should be noted, that CCI is often also referred to as thermodynamic integration. In this thesis, the term thermodynamic integration will exclusively refer to Eq. (2.6.2).

The difference in free energy ΔF between system 0 and 1 is given by

$$\Delta F = \int_0^1 \frac{\partial F(\lambda)}{\partial \lambda} d\lambda. \quad (2.6.22)$$

The free energy $F(\lambda)$ is related to the Hamiltonian $H(\lambda)$ via the canonical partition function $Q(\lambda)$ as

$$F(\lambda) = -\beta^{-1} \ln Q(\lambda). \quad (2.6.23)$$

The canonical partition function can be denoted as an integral over the phase space as

$$Q(\lambda) = \int \frac{d\mathbf{r}d\mathbf{p}}{h^{3N}N!} e^{-\beta H(\lambda)}, \quad (2.6.24)$$

where h is the Planck constant. Using the canonical partition function ΔF becomes

$$\Delta F = - \int_0^1 d\lambda \frac{\partial}{\partial \lambda} \beta^{-1} \ln Q(\lambda) \quad (2.6.25)$$

$$= - \int_0^1 d\lambda \beta^{-1} \frac{1}{Q(\lambda)} \frac{\partial}{\partial \lambda} \int \frac{d\mathbf{r}d\mathbf{p}}{h^{3N}N!} e^{-\beta H(\lambda)} \quad (2.6.26)$$

$$= \int_0^1 d\lambda \frac{1}{Q(\lambda)} \int \frac{d\mathbf{r}d\mathbf{p}}{h^{3N}N!} \left(\frac{\partial V(\lambda)}{\partial \lambda} \right) e^{-\beta H(\lambda)} \quad (2.6.27)$$

$$= \int_0^1 d\lambda \left\langle \frac{\partial V(\lambda)}{\partial \lambda} \right\rangle_\lambda. \quad (2.6.28)$$

In the last step, it has been used that the ensemble average of any thermodynamic quantity A can be calculated via

$$\langle A \rangle_\lambda = \frac{1}{Q(\lambda)} \int \frac{d\mathbf{r}d\mathbf{p}}{h^{3N}N!} A e^{-\beta H(\lambda)}. \quad (2.6.29)$$

Substituting Eq. (2.6.21) into Eq. (2.6.28) yields

$$\Delta F = \int_0^1 \langle V_1 - V_0 \rangle_\lambda d\lambda. \quad (2.6.30)$$

The result provides a straight-forward recipe to calculate free energy differences within molecular dynamics or Monte Carlo simulations: a system with potential $V(\lambda)$ is simulated at a series of λ values. For each simulation, the difference of the potential energies is averaged over a thermodynamically equilibrated run. Finally,

	a [a.u.]	b [a.u.]	L [a.u.]
H-H	1.0	2.5	8.0
H-He	1.0	1.9	8.0
He-He	1.0	1.2	8.0

Table 2.6.1: Coefficients for the reflected Yukawa pair potentials [135]. Values are given in atomic units.

the integration with respect to λ is carried out. In contrast to the thermodynamic integration introduced in Sec. 2.6.1, it is possible to use the ideal gas as system 0. The interaction energy of the ideal gas is zero, i.e. $V_0 = 0$, and Eq. 2.6.28 simplifies to

$$\Delta F = \int_0^1 \langle V_1 \rangle_\lambda d\lambda \quad (2.6.31)$$

The absolute value of the free energy of an ideal gas is given by:

$$F_{\text{id}} = - \sum_{\alpha} N_{\alpha} k_{\text{B}} T \left(\ln \frac{V}{N_{\alpha} \lambda_{\alpha}^3} + 1 \right), \quad (2.6.32)$$

where $\lambda_{\alpha} = h/\sqrt{2\pi m_{\alpha} k_{\text{B}} T}$ is the thermal wavelength. However, obtaining the free energy difference between the real DFT-MD system and the ideal gas directly is not recommended, because at $\lambda = 0$ the interaction energy and thus the forces on the ions become zero. This eventually leads to an ideal distribution of particles, where particles might overlap significantly. But according to Eq. (2.6.30) the energy V_1 , i.e. the DFT energy, has to be computed for these configurations. This might lead to numerical instabilities where the Kohn-Sham cycle does not converge. To avoid these difficulties, the CCI is split into two steps: First, the free energy difference between a classical reference potential and the ideal gas $\Delta F_{\text{id} \rightarrow \text{cl}}$ is evaluated via Eq. (2.6.31). Second, the free energy difference between the DFT-MD system and the classical reference potential $\Delta F_{\text{cl} \rightarrow \text{DFT}}$ is evaluated via Eq. (2.6.28). The absolute free energy F then becomes:

$$F = F_{\text{id}} + \Delta F_{\text{id} \rightarrow \text{cl}} + \Delta F_{\text{cl} \rightarrow \text{DFT}}. \quad (2.6.33)$$

The classical reference potential should closely resemble the DFT-MD system in terms of radial distribution function and energy. Thus, an accurate integration of Eq. (2.6.28) is possible with only few coupling-constants. In this work, the reflected

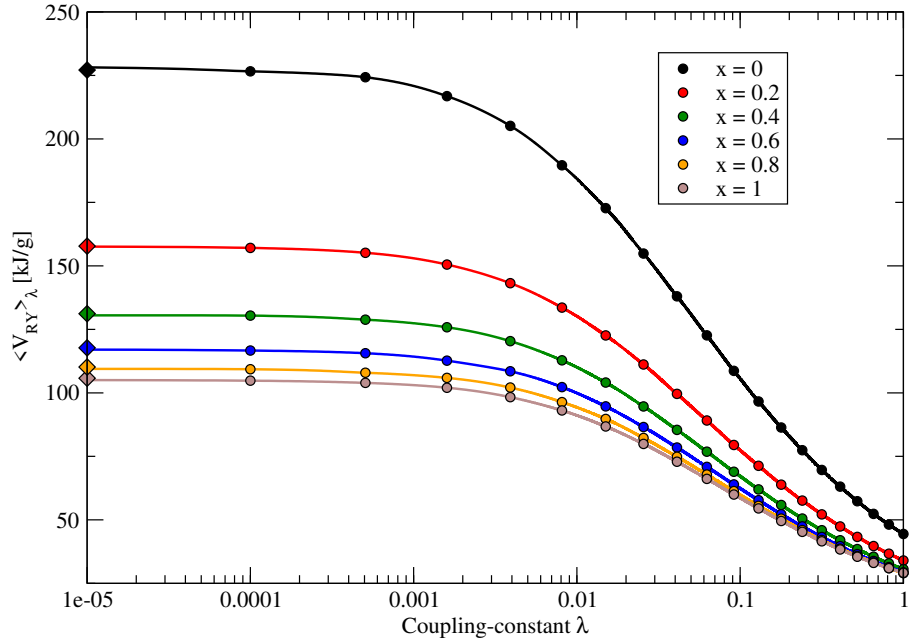


Figure 2.6.1: Integrand of Eq. (2.6.31) for the reflected Yukawa potential at a temperature of $T = 10\,000$ K and a Wigner-Seitz-radius of $r_s = 1.4\,a_0$. The ensemble average of the RY potential simulated at different coupling-constants is shown for various He fractions (coloured circles). The diamonds on the left side represent the analytical values obtained via Eq. (2.6.36) for $\lambda = 0$. Lines are Akima splines.

Yukawa (RY) pair potentials given by Morales *et al.* [135] have been used. The potential energy $V_{RY}(\mathbf{r})$ can then be expressed as:

$$V_{RY}(\mathbf{r}) = \sum_{i=1}^N \sum_{j=i+1}^N V_{RY}^{ij}(r_{ij}), \quad (2.6.34)$$

where $V_{RY}^{ij}(r_{ij})$ is the potential between atom i and j depending on their distance $r_{ij} = |\mathbf{r}_i - \mathbf{r}_j|$:

$$V_{RY}^{ij}(r_{ij}) = \begin{cases} a \left(\frac{e^{-br}}{r_{ij}} + \frac{e^{-b(L-r_{ij})}}{L-r_{ij}} - 4 \frac{e^{-bL/2}}{L} \right) & r_{ij} \leq L/2, \\ 0 & r_{ij} > L/2, \end{cases} \quad (2.6.35)$$

where a , b , and L are parameters. If two different species are considered the parameters depend on the species of atom i and j . For a H-He system three sets of parameters need to be known for the interaction between H-H, H-He, and He-He. These are given in Table 2.6.1. The free energy of the RY potential was obtained using a Metropolis Monte Carlo (MMC) code [226, 252], that has been developed as

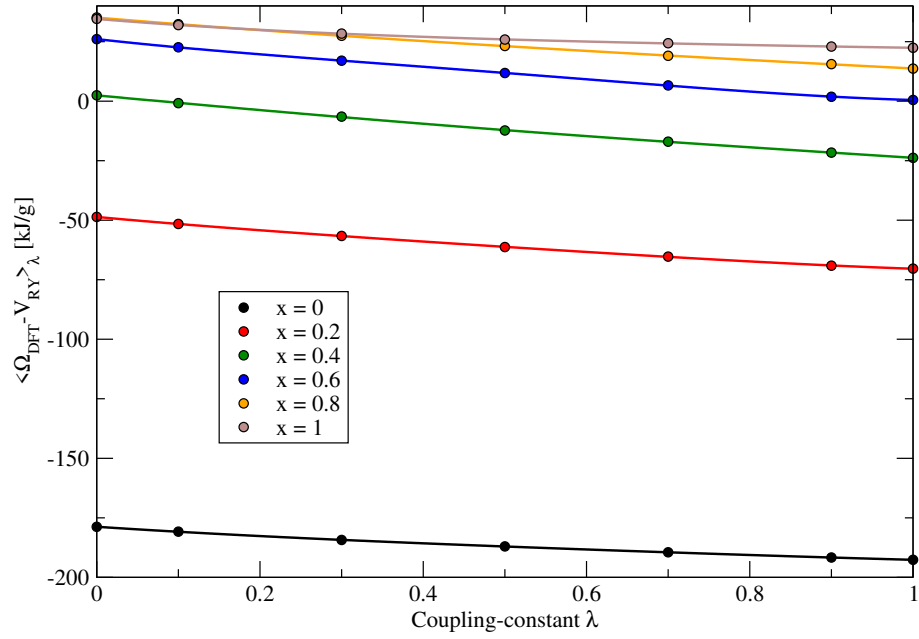


Figure 2.6.2: Thermodynamic integration of the DFT and RY system at a temperature of $T = 10\,000$ K and a Wigner-Seitz-radius of $r_s = 1.4 a_0$. The ensemble average simulated at different coupling-constants is shown for various He fractions (coloured circles). Lines are 4th order polynomial fits to the data.

part of this thesis. The MMC code evaluates Eq. (2.6.31) for $V_1 = V_{\text{RY}}$ using twenty λ values. In Fig. 2.6.1, the integrand of Eq. (2.6.31) is shown as a function of the coupling-constant λ for various He fractions. Solid lines are Akima splines [253], which have been used for the numerical integration. For $\lambda \rightarrow 0$ the data becomes constant and the diamonds show the analytical value for $\lambda \rightarrow 0$ obtained via

$$\langle V_{\text{RY}} \rangle_{\lambda} = \frac{N^2}{2V} \sum_i \sum_j x_i x_j \int_0^{\infty} d\mathbf{r} V_{\text{RY}}^{ij}(\mathbf{r}) g_{\lambda}^{ij}(\mathbf{r}), \quad (2.6.36)$$

where the sums are over particle species i and j with particle fraction x_i and x_j . The radial distribution function $g_{\lambda}^{ij}(\mathbf{r})$ has to be known for a system obeying the total potential given by Eq. 2.6.21. As already noted, at $\lambda = 0$ the interaction potential is that of an ideal gas, i.e. $V_0 = 0$, and the radial distribution function is thus unity. This enables the analytic evaluation of Eq. (2.6.36). Comparing the analytic solution to the MMC data set shows very good agreement.

The free energy of the DFT-MD system was obtained by implementing the CCI procedure into the VASP code which was done as part of this thesis. In finite-temperature DFT-MD simulations, the energy as functional of the density $E[n]$ is

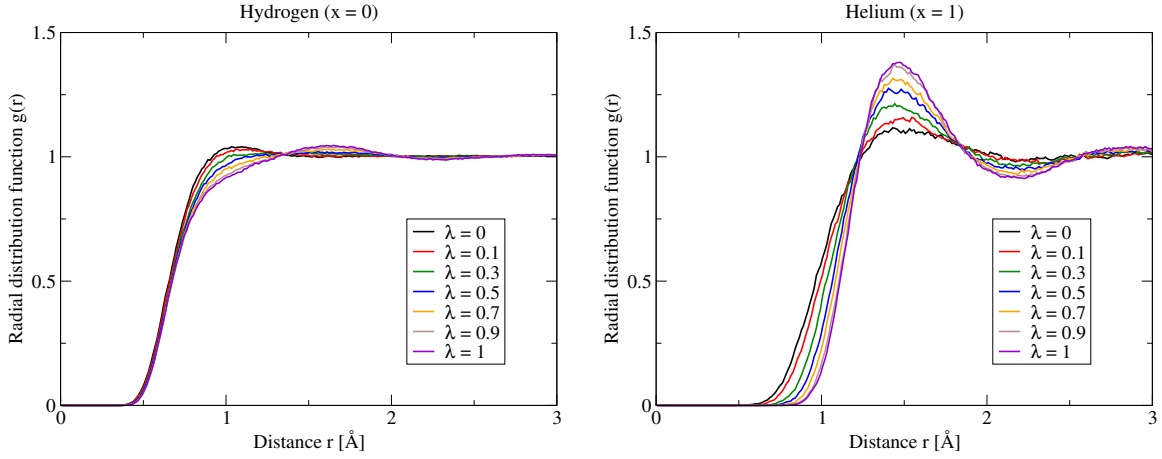


Figure 2.6.3: Radial distribution functions of pure hydrogen and pure helium at a temperature of $T = 10\,000$ K and a Wigner-Seitz-radius of $r_s = 1.4 a_0$ for different coupling-constants λ , where $\lambda = 0$ is the RY system and $\lambda = 1$ is the DFT system.

replaced by the free energy $F[n]$, see Sec. 2.2.3. As a consequence, the forces on the ions are derived from the Mermin free energy [142]

$$\Omega_{\text{DFT}} = V_{\text{KS}} - TS_{\text{id}}, \quad (2.6.37)$$

where $V_{\text{KS}} = \int d\mathbf{r} n(\mathbf{r}) v_{\text{KS}}(\mathbf{r})$ is the Kohn-Sham potential and S_{id} is the ideal entropy given by Eq. (2.2.23) due to the lack of finite-temperature XC functionals. Thus, the free energy difference to the classical potential, i.e. the reflected Yukawa potential, $\Delta F_{\text{cl} \rightarrow \text{DFT}}$, is

$$\Delta F_{\text{cl} \rightarrow \text{DFT}} = \int_0^1 \langle \Omega_{\text{DFT}} - V_{\text{RY}} \rangle_\lambda d\lambda \quad (2.6.38)$$

In Fig. 2.6.2, the integrand of Eq. (2.6.38) is shown for various He fractions. The obtained data are very smooth and well-behaved, so that they could be fitted to a 4th order polynomial function. This allows for an analytic evaluation of the coupling-constant integral. Most importantly, the number of coupling-constants, which need to be simulated can be kept as low as seven values, which is beneficial for the evaluation of CCI entropies. This is also due to the fact, that the structure of the H-He system at $T = 10\,000$ K and $r_s = 1.4 a_0$ is quite simple in the sense that correlations are low and no molecules are present. This can be seen when comparing the radial distribution functions $g(r)$ for pure H and pure He as shown in Fig. 2.6.3. The transition from the RY system ($\lambda = 0$) to the DFT system ($\lambda = 1$) is smooth and does not involve huge changes in the internal structure.

It is possible to reduce the amount of coupling-constants to a single value using further approximations. For that, the integrand of Eq. (2.6.22), i.e. the derivative of F w.r.t. λ , is expanded in a Taylor series centred around λ_0 [254, 255]:

$$\Delta F = \int_0^1 d\lambda \sum_{n=0}^{\infty} \frac{1}{n!} \left(\frac{\partial^{n+1} F(\lambda)}{\partial \lambda^{n+1}} \right)_{\lambda_0} (\lambda - \lambda_0)^n. \quad (2.6.39)$$

Truncating this series after the linear term and evaluating the derivatives as described in Appendix A.2 leads to

$$\Delta F \simeq \langle V_1 - V_0 \rangle_{\lambda_0} - \frac{1 - 2\lambda_0}{2k_B T} \left\{ \langle (V_1 - V_0)^2 \rangle_{\lambda_0} - \langle V_1 - V_0 \rangle_{\lambda_0}^2 \right\}. \quad (2.6.40)$$

This method will be called reduced CCI (RCCI) in the following. The expression in curly braces is the variance of $V_1 - V_0$ at the given λ_0 . Thus, the derivative of the integrand in Eq. (2.6.22) w.r.t. λ is given by

$$\frac{\partial}{\partial \lambda} \frac{\partial F}{\partial \lambda} = -\beta \text{Var} (V_1 - V_0)_{\lambda}. \quad (2.6.41)$$

If the potentials V_0 and V_1 yield similar configurations and energies, the variance and the slope of the integrand will be small resulting in a good approximation for ΔF . Higher order terms have been derived, but no systematic convergence could be achieved, see Appendix A.2 for more information.

2.7 Numerical settings of the DFT-MD simulations

In this section the numerical settings of the performed simulations will be outlined. The DFT-MD simulations have been performed using the plane-wave code VASP (Vienna Ab Initio Simulation Package) [219–221]. Every simulation setting was determined by extensive convergence tests, see e.g. the appendix of Ref. [85] where convergence tests for H-He mixtures are discussed in detail. The used cutoff energy is 1 200 eV. The Baldereschi mean-value \mathbf{k} -point [256] was used. Molecular dynamic simulations were performed with a time step of 0.2 fs and thermodynamic averages were taken for at least 10 000 time steps after thermodynamic equilibrium has been reached. Projector-augmented wave pseudopotentials (PAW) [218] supplied with VASP have been used. Specifically, these were pseudopotentials with a core radius of $r_c = 1.1 a_0$ both released in 2001. Simulations for the equation of state have been performed for 29 He concentrations for 15 temperatures in the range of 1 000 K to 15 000 K and several pressures in the range of 0.2 and 30 Mbar summing up to more

than 7 500 calculations. An electron number of 64 has been used for these calculations. Pressures are converged within 1 % in the given pressure range. Simulations for the CCI, RCCI and 2PT-MF calculations have been performed for an electron number of 256 to reduce finite-size effects. Other convergence settings were chosen as for the EOS calculations.

Chapter 3

Equation of state

Density functional theory molecular dynamics simulations in the canonical ensemble, i.e. at constant volumes and temperatures, have been performed as described in Ch. 2. The discrete simulation data (energy per particle $u = U/N$ and pressure p as function of volume per particle $v = V/N$, temperature T and helium fraction x) are inverted such that u and v are given as functions of p , T and x . Energy and volume per particle are fit as functions of p at constant T , and x using the following formulas:

$$\ln v(p) = \sum_{i=0}^4 A_i (\ln p)^i, \quad (3.1)$$

$$\ln (u(p) + c) = \sum_{i=0}^4 B_i (\ln p)^i, \quad (3.2)$$

where A_i and B_i are coefficients and $c = 10$ eV/atom is a constant that shifts the energy to positive values avoiding negative arguments in the logarithm. In principle, it would be desirable to obtain a two-dimensional fit of both p and T or even a three-dimensional fit of x , p , and T , but all tested model functions had an inferior accuracy compared to the one-dimensional fit functions. In the following two sections, the equation of state (without NQC) is shown for a selected number of isotherms for pure H and pure He and compared to the hydrogen and helium Rostock EOS in its third version (H-REOS.3 and He-REOS.3) [230]. The H/He-REOS.3 use DFT-MD calculations and the PBE functional in the strongly correlated regime. For lower densities, these data are connected to the fluid variational theory calculations of Juranek *et al.* [257], Holst *et al.* [89], and Saumon *et al.* [258], and to a virial EOS [230]. The following figures, that show the vdW-DF EOS, are limited to three isotherms to ensure the readability of the figures. Due to the enormous amount of data produced for this thesis, it is not possible to print the

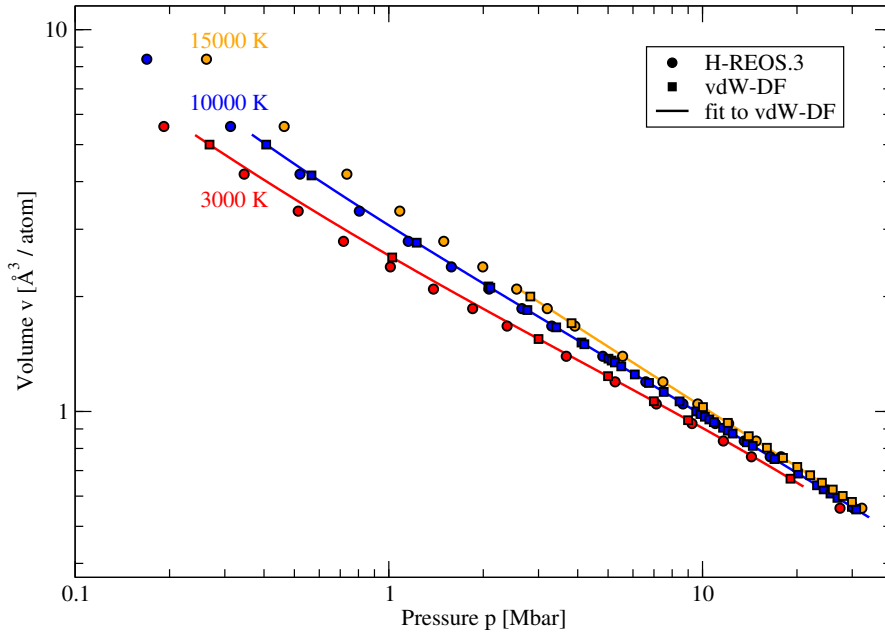


Figure 3.1.1: Volume as function of pressure for three temperatures (colour coded) for pure hydrogen. The H-REOS.3 based on PBE is compared to simulations using the vdW-DF. Lines are fits to the vdW-DF data using Eq. (3.1).

EOS and the fit coefficients in tabular form (there are 7933 EOS points resulting in 4350 fit coefficients). Still, these data can be provided upon request. In the third section, the EOS of the mixture is displayed. This is done by calculating the volume of mixing Δv , energy of mixing Δu , and enthalpy of mixing Δh according to Eq. (2.5.24), (2.5.25), and (2.5.26), respectively. For mixtures, the H/He-REOS.3 (and any other EOS for the pure components) can only be used within the linear mixing approximation and Δv , Δu , and Δh are zero by definition. PBE data for the real mixture have been calculated by Lorenzen *et al.* [65, 85, 134] as part of their miscibility calculations, which will be used for comparison.

3.1 Hydrogen

In Fig. 3.1.1, the volume per atom is shown as function of pressure for pure hydrogen. For the 15000 K isotherm, there exist no vdW-DF data for pressures lower than 3 Mbar. It will become apparent later that, at this temperature, no demixing occurs for all considered pressures so that the missing data is not crucial. Compared to the PBE functional used in the H-REOS.3, the vdW-DF shows higher pressures at constant volume. This shift to higher pressures is more pronounced for low pres-

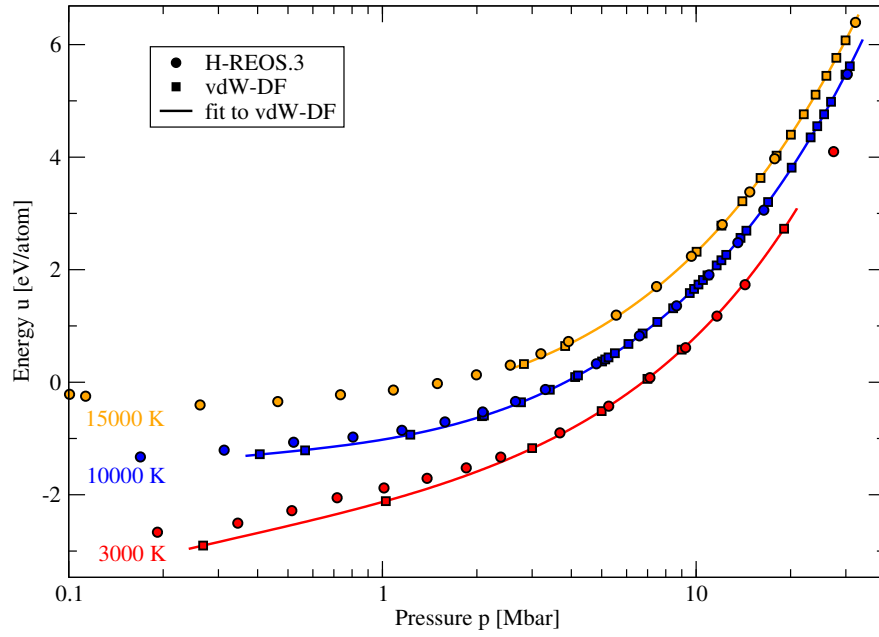


Figure 3.1.2: Energy as function of pressure for three temperatures (colour coded) for pure hydrogen. The H-REOS.3 based on PBE is compared to simulations using the vdW-DF. Lines are fits to the vdW-DF data using Eq. (3.2).

tures and has also been noted by Clay *et al.* [147, 211] in their benchmarking study. Compared to these QMC calculations, the vdW-DF overestimates the pressure by up to 4% for pure H at a volume of $v = 1.49 \text{ \AA}^3/\text{atom}$ [147]. Under these conditions, PBE overestimates the pressure only by 1%. The difference between PBE and vdW-DF decreases significantly with increasing pressure and increasing temperature, so that differences between PBE and vdW-DF in the miscibility diagram are expected to occur mainly at small pressures.

In Fig. 3.1.2, the energy per atom is shown as a function of pressure. Symbols and lines are equal to Fig. 3.1.1. A constant shift of $\Delta u = 13.32 \text{ eV/atom}$ has been added to the H-REOS.3, so that the energies of H-REOS.3 and the vdW-DF data match at $T = 15000 \text{ K}$ and $p = 30 \text{ Mbar}$. This point has been chosen because the pressure difference between PBE and vdW-DF is least for a given volume. The slope of the vdW-DF energy is similar to the H-REOS.3 for high pressures. For lower pressures, there are significant differences in the slopes and the energy deviates significantly for pressures smaller than 3 Mbar. Comparing the EOS with the hydrogen phase diagram and the metallisation predictions of PBE and vdW-DF in Fig. 1.2.1 reveals that the energies and volumes differ most in the molecular regime, i.e. for $p < 3 \text{ Mbar}$.

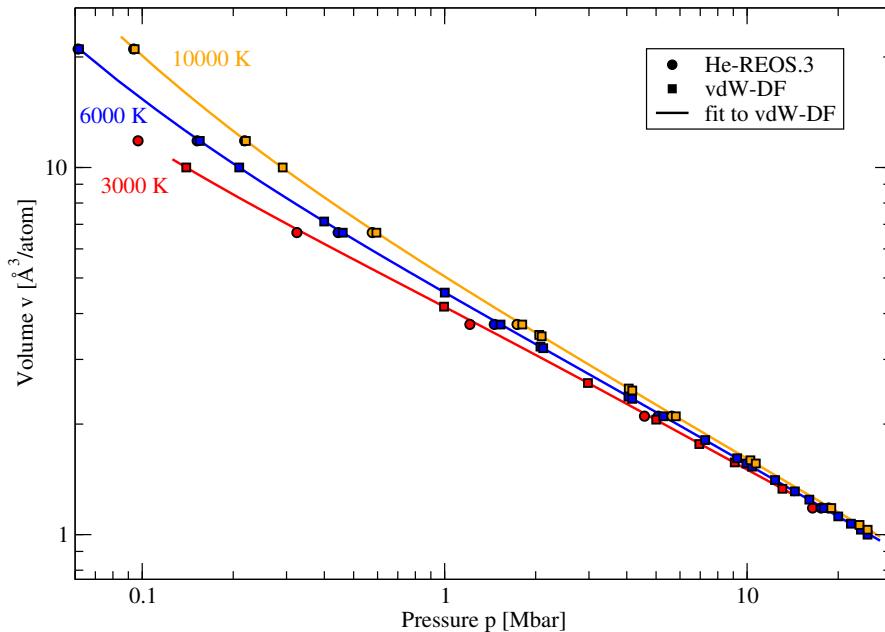


Figure 3.2.1: Volume as function of pressure for three temperatures (colour coded) for pure helium. The He-REOS.3 based on PBE is compared to simulations using the vdW-DF. Lines are fits to the vdW-DF data using Eq. (3.1)

3.2 Helium

In Fig. 3.2.1, the volume per atom is shown as a function of pressure for pure helium. The given temperatures are different to those shown in Fig. 3.1.1 and 3.1.2 because the He-REOS.3 table has no entry for 15 000 K. The 6 000 K isotherm is shown instead. Differences in volumes between the He-REOS.3 and the vdW-DF are less than 5%, and there is no strong pressure dependence as for hydrogen that was caused by the molecular regime.

In Fig. 3.2.2, the energy per atom is shown as a function of pressure for pure helium. Temperatures are equal to those shown in Fig. 3.2.1. The energy of the He-REOS.3 has been shifted to match the vdW-DF energies at 10 000 K and 30 Mbar similar to the energy of the H-REOS.3 in the previous section. As for hydrogen, the slope of the vdW-DF energy shows a lower deviation to the He-REOS.3 at higher pressures than at lower pressures. However, the deviations do not decrease when temperature is increased as for hydrogen.

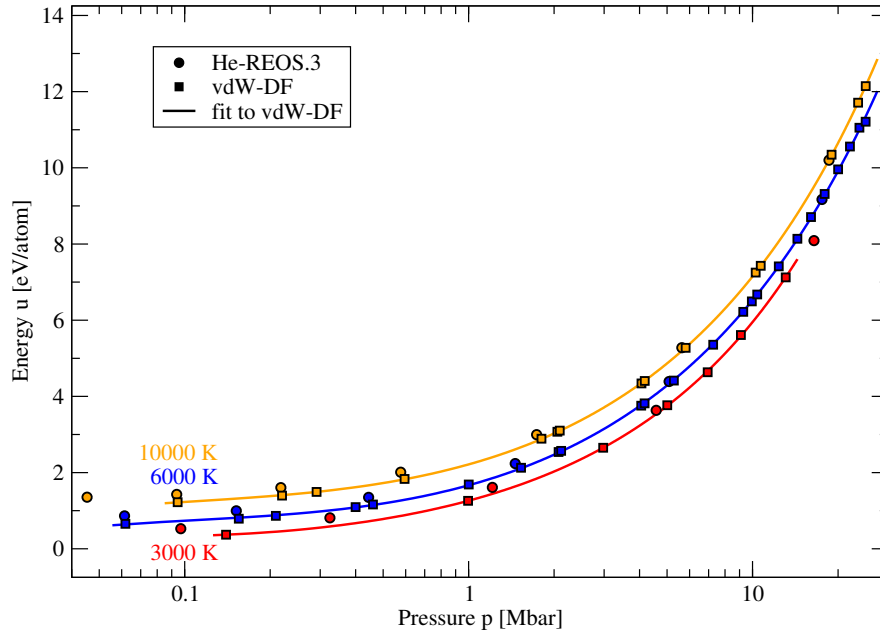


Figure 3.2.2: Energy as function of pressure for three temperatures (colour coded) for pure helium. The He-REOS.3 based on PBE is compared to simulations using the vdW-DF. Lines are fits to the vdW-DF data using Eq. (3.2)

3.3 H-He mixtures

In Fig. 3.3.1, the volume of mixing Δv (top panels), energy of mixing Δu (middle panels), and enthalpy of mixing Δh (bottom panels) are shown for temperatures of 3000 K (left column) and 10000 K (right column) and pressures of 2 Mbar, 4 Mbar, and 10 Mbar. Open symbols show the data of Lorenzen *et al.* [65, 85, 134] and closed symbols show the vdW-DF data. The volume of mixing shown in the first row generally decreases with increasing pressure and increasing temperature at fixed He fraction. The PBE data show lower Δv than the vdW-DF data except for 3000 K and 10 Mbar. The pressure dependence of Δv is significantly stronger than its temperature dependence as already seen in Fig. 3.1.1 and 3.2.1. In the second row of Fig. 3.3.1, the energy of mixing Δu is shown. It can be seen that Δu increases with increasing pressure and temperature as apparent from Fig. 3.1.2 and 3.2.2. The PBE functional results in higher Δu for all of the shown conditions. At 3000 K and 2 Mbar, the vdW-DF energy of mixing is negative while the PBE energy of mixing is positive. Negative Δu occur, where pure hydrogen is still in its molecular form. At the shown pressures of 4 Mbar and 10 Mbar, hydrogen is already dissociated, see the hydrogen phase diagram, Fig. 1.2.1. At 3000 K, the Δu for PBE at 2 Mbar is

similar to the Δu for the vdW-DF at 4 Mbar. This also underlines the already noted pressure shift between PBE and the vdW-DF. At 10 000 K, the energy of mixing is positive for all shown conditions. The third row of Fig. 3.3.1 shows the enthalpy of mixing $\Delta h = \Delta u + p\Delta v$. Despite the negative Δu at 3 000 K and 2 Mbar for the vdW-DF, Δh is positive for all shown conditions. The enthalpy of mixing shows the same trend as the energy of mixing, i.e. it increases with increasing pressure and temperature. The enthalpy itself does not allow any conclusion about demixing. As shown in Sec. 2.5, the entropy of mixing is required to calculate the Gibbs free energy of mixing. Previous calculations by Lorenzen *et al.* [134] approximated the entropy with the ideal entropy of mixing per particle

$$\Delta s_{\text{id}} = -k_{\text{B}} [(1-x) \ln(1-x) + x \ln x]. \quad (3.1)$$

In Fig. 3.3.1, the ideal entropy of mixing times temperature $T\Delta s_{\text{id}}$ is shown for comparison. It can be seen that $T\Delta s_{\text{id}}$ is on the same order of magnitude as the enthalpy data. Thus, the difference of Δh and $T\Delta s_{\text{id}}$ required to calculate the Gibbs free energy is small and demixing features depend crucially on the accuracy of the simulations. In the next chapter, the non-ideal entropy of mixing will be calculated.

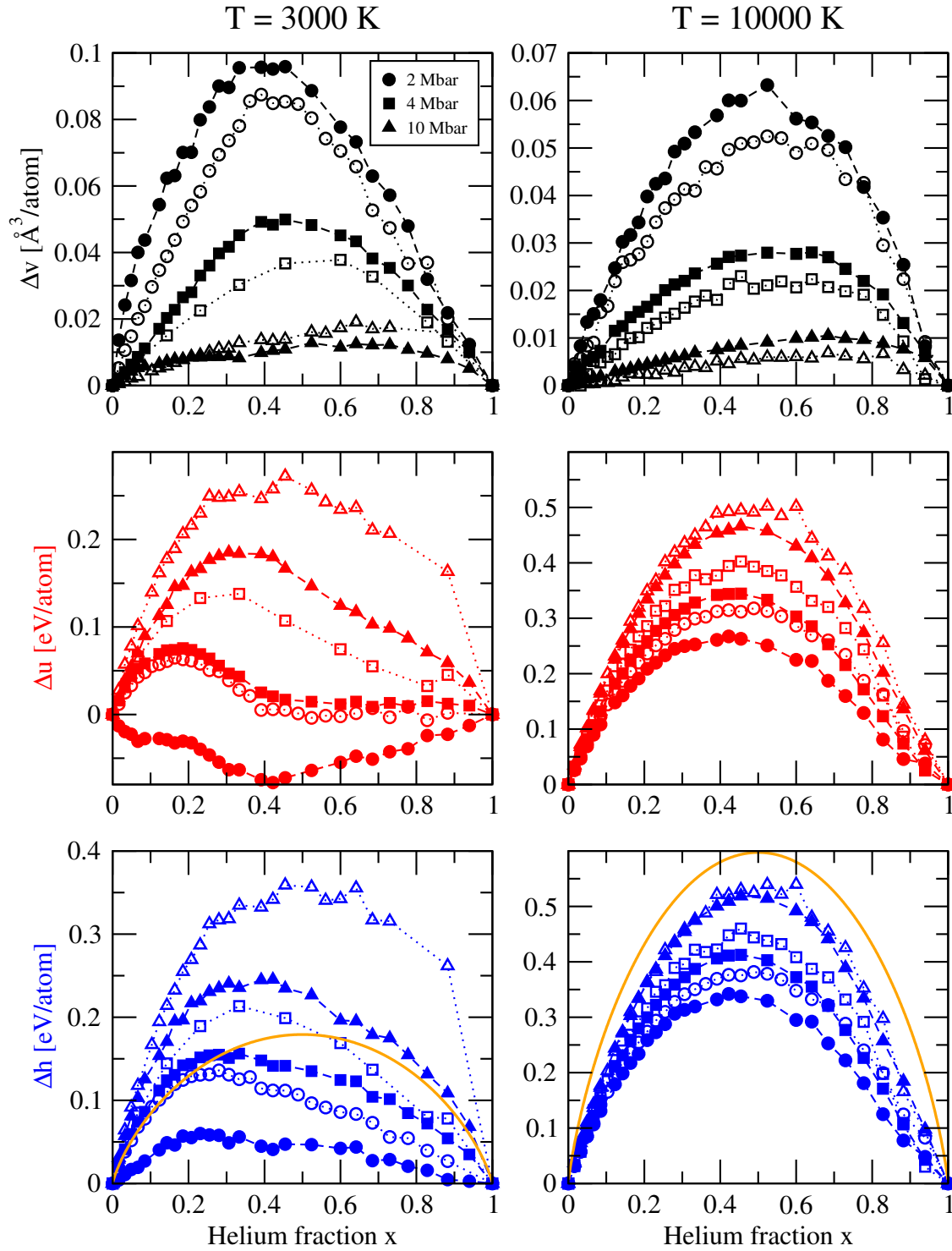


Figure 3.3.1: Volume of mixing (black), energy of mixing (red), and enthalpy of mixing (blue) at 3000 K (left column) and 10000 K (right column) for 2 Mbar (circles), 4 Mbar (squares), and 10 Mbar (triangles). The vdW-DF data (filled symbols) are compared to the PBE data of Lorenzen *et al.* [65, 85, 134] (open symbols). The orange line in the bottom row shows the ideal entropy of mixing times temperature in eV/atom. Other lines are guides to the eye.

Chapter 4

Entropy of H-He mixtures

In this chapter, the entropies of H-He mixtures are calculated, which are needed in order to obtain the Gibbs free energy. In the first section, the general strategy to calculate entropies is outlined. In Sec. 4.2, entropies obtained at a carefully chosen reference point are compared. In Sec. 4.3, it is detailed how the entropies at the reference point are used for the thermodynamic integration via Eq. (2.6.2) to compute entropies at arbitrary pressures and temperatures.

4.1 Basic idea and strategy

The aim is to avoid the ideal entropy approximation by calculating the non-ideal ionic entropy for all considered He fractions in the temperature range of 1 000 K to 15 000 K and pressure range of 0.2 to 30 Mbar for 29 different He fractions. The most reliable way is to apply coupling-constant integration for all EOS points because it is formally exact and has been successfully applied to H-He mixtures by other authors [135, 136, 141, 142, 231]. However, this approach is not feasible because it would exceed the given computational resources by a large factor, not taking into account the time needed to obtain adequate classical potentials. Another approach is to apply the 2PT-MF method for any EOS point, which only needs the velocities of the particles to calculate the VDOS and the partial volumes. Yet, the VDOS is sensitive to the particle number, especially for low and high He fractions, where only a few particles of either species are in the box. Thus, all EOS calculations would need to be redone using higher particle numbers. This, in turn, would lead to demixing in the box at certain conditions, which influences the entropy. The resulting simulation data would not be those of a uniformly mixed system as required by Eq. (2.5.19). But most notably, it will be shown in the next section, that the 2PT-MF method

does not yield accurate and thermodynamically consistent results for H-He mixtures. Therefore, the strategy is to calculate entropies via thermodynamic integration of the equation of state, where the needed reference entropies for the He fractions are calculated using coupling-constant integration. Morales *et al.* [135] applied the same strategy and defined the reference state at temperature $T_{\text{ref}} = 10\,000$ K and Wigner-Seitz radius $r_s = 1.25\,a_0$. The resulting pressures might be too close to the demixing region and features of demixing are already visible in the radial pair-distribution function, see Fig. 5 of Ref. [135]. Thus, for the calculations in this work, the reference state was shifted to $r_s = 1.40\,a_0$, i.e. lower pressures, to avoid any demixing in the simulation box. Coupling-constant integrations at the reference point have not been performed for all 29 He fractions, because of the high computational costs. Instead, 12 He fractions were chosen and a Redlich-Kister fit [241] was applied to obtain reference entropies for arbitrary He fractions. The reference entropies have then been used to perform thermodynamic integrations of the equation of state to calculate entropies for arbitrary pressures and temperatures. In the next section, the entropy at the given reference state will be calculated using different approaches.

4.2 Entropy at the reference point

At the beginning of this work, the idea was to use the 2PT-MF method at the reference state ($T_{\text{ref}} = 10\,000$ K, $r_s = 1.4\,a_0$) instead of coupling-constant integration, because entropies can be obtained much faster from a single MD run and the numerical implementation is much simpler. However, the accuracy of the 2PT-MF method for H-He mixtures was unknown while the CCI method has been successfully applied [135, 136, 141, 142, 231]. As mentioned in Sec. 2.6.2, the partial volumes are needed to apply the 2PT-MF method. These were obtained using the method of intercepts as described in Sec. 2.5 and are shown in Fig. 4.2.1. In panel **a** of this figure, the application of the method of intercepts to three different He fractions at the reference point is shown. The given pressures correspond to the pressures at $r_s = 1.4\,a_0$ for the given x . Panel **b** shows the partial volumes of H and He and their ratio at the reference state as a function of He fraction. Although there is a significant change in the partial volumes, their influence on the entropy is only on the order of $0.01\,k_B/\text{atom}$. If the partial volume is approximated with the specific volume at constant pressure for pure H and He, the error in entropy would also be of the same order of magnitude, so that the effort in calculating partial volumes could be avoided entirely for future calculations.

The resulting total entropies for the 2PT-MF method are shown in Fig. 4.2.2. Ad-

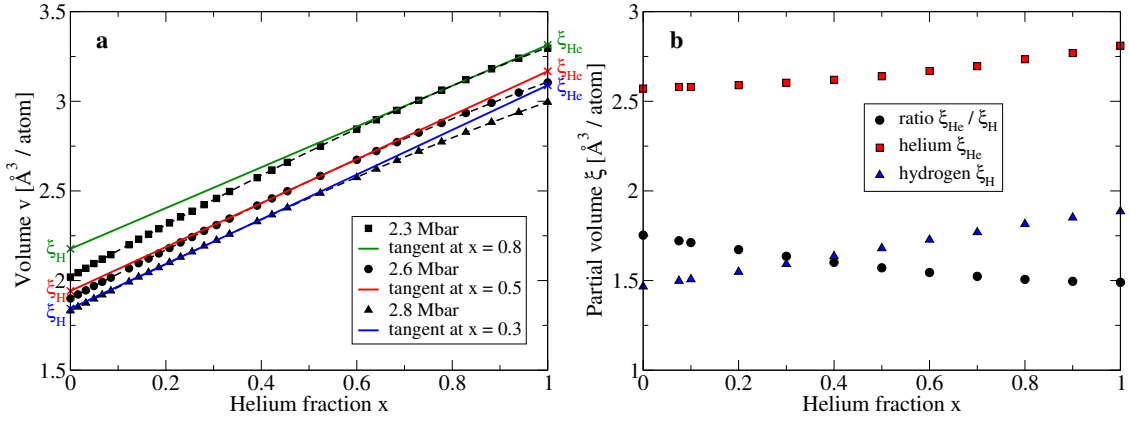


Figure 4.2.1: **a**: Volume versus He fraction for three pressures at 10 000 K. The determination of partial volumes for H and He is demonstrated for three He fractions at pressures corresponding to the reference state. Partial volumes are indicated by the crosses at $x = 0$ for hydrogen and $x = 1$ for helium. **b**: Partial volumes and their ratio at the reference state for all considered He fractions.

ditionally, the entropy has been calculated using the CCI, and RCCI methods for the same conditions as described in Sec. 2.6. The RCCI method has been applied for three λ_0 values. The CCI method is most accurate with an estimated error of $0.01 k_B/\text{atom}$. An error bar of 1% is shown for the 2PT-MF method, which has been demonstrated for liquid metals [243]. Despite this rather large error, the 2PT-MF entropies deviate significantly from the CCI entropies. While the 2PT-MF method works well for liquid metals near the melting line, deviations of up to $0.46 k_B/\text{atom}$ compared to the CCI approach are observed.

The RCCI method shows in general a much smaller deviation to the full CCI approach than the 2PT-MF method. For a value of $\lambda_0 = 0$ the deviation is largest on average with a maximum error of $0.34 k_B/\text{atom}$ at $x = 1$. For $\lambda_0 = 1$ the agreement with CCI is better with a maximum error of $0.12 k_B/\text{atom}$ at $x = 0.8$. The best performance of the RCCI method was achieved for a value of $\lambda_0 = 0.5$ where a maximum error of $0.042 k_B/\text{atom}$ can be seen at $x = 1$. The differences in entropy for different λ_0 especially for $x = 1$ can be explained by comparing $\langle \Omega_{\text{DFT}} - U_{\text{RY}} \rangle_\lambda$ for different He fractions as shown in Fig. 2.6.2. The slope of the $x = 1$ curve is significantly different to the other He fractions, most notably for small λ values. This leads to larger errors in the RCCI method because the λ integration is not well represented by a linear expansion in λ at these small λ values, cf. Eq. (2.6.40). In general, it would be possible to obtain higher order terms for the RCCI method, but systematic convergence of the higher order terms could not be achieved, see

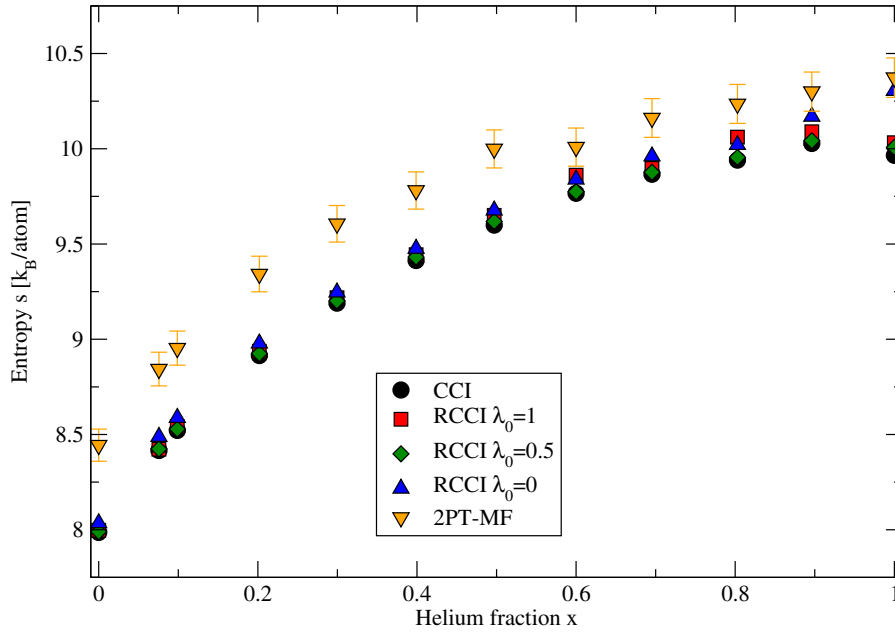


Figure 4.2.2: Entropy of H-He mixtures as a function of He fraction x at $T = 10\,000$ K and $r_s = 1.4 a_0$. Data for the coupling-constant integration (CCI), reduced coupling-constant integration (RCCI), and 2PT-MF method have been obtained using the vdW-DF.

Appendix A.1. This was due to the fact, that higher order terms are increasingly hard to converge and much more simulation time would be needed to do so.

In general, the performance of the RCCI method is surprisingly good given the performance of the reflected Yukawa potential at these conditions, see Fig. 2.6.3 where the radial pair-distribution function of the RY and the DFT system has been compared. The calculations demonstrate, that even these moderately accurate potentials can yield highly accurate entropies with the RCCI method and the computational effort can be decreased significantly if special attention is paid to finding a good pair potential. More importantly, if $\lambda_0 = 1$ is chosen, the RCCI method can be applied without modifications in the DFT-MD code, because the simulation is performed with pure DFT forces and the classical potential can be evaluated on the DFT-MD trajectory in a post-processing step to evaluate the ensemble averages of Eq. (2.6.40). Still, the RCCI method works only well, if structural changes in the coupling-constant integration procedure are small. In molecular systems, where dissociation occurs, the effective potential would most likely not reproduce the dissociation reactions accurately enough for the RCCI method to work.

In Fig. 4.2.3, the entropy of mixing, Eq. (2.5.23), is shown at the reference point

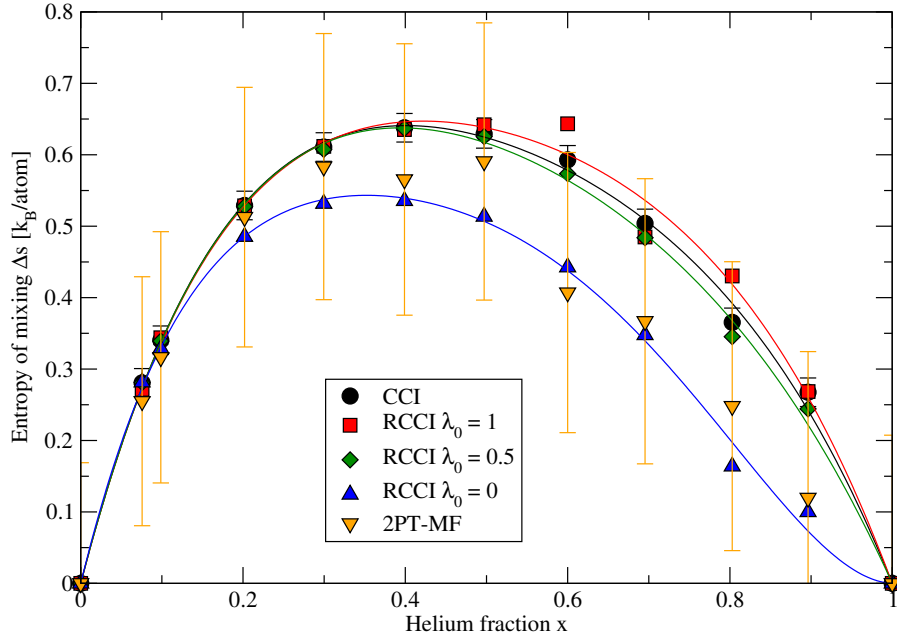


Figure 4.2.3: Entropy of mixing of H-He mixtures as a function of He fraction x at $T = 10\,000$ K and $r_s = 1.4\,a_0$. Data for the coupling-constant integration (CCI), reduced coupling-constant integration (RCCI), and 2PT-MF method have been obtained using the vdW-DF.

for the 2PT-MF, CCI, and RCCI methods similar to Fig. 4.2.2. For the 2PT-MF method, an estimated uncertainty of 1% in the total entropies results in an uncertainty of $\sim 0.2\,k_B/\text{atom}$ in the entropies of mixing, which translates into a relative uncertainty of at least 30%. The CCI entropies of mixing are within the error bars of the 2PT-MF entropies of mixing. The RCCI method for $\lambda_0 = 0$ also shows a significant deviation to the CCI entropies of mixing. For $\lambda_0 = 0.5$ and $\lambda_0 = 1$ the entropies of mixing agree well with the CCI entropies of mixing. The lines in Fig. 4.2.3 are third order RK fits.

The CCI method is in principle exact if the integration w.r.t. λ is performed using a sufficient amount of simulations. Thus, the CCI entropies are expected to be most accurate at the chosen reference point. In contrast, the 2PT-MF method relies on approximations and it can be shown, that the obtained data are not thermodynamically consistent with the equation of state. Therefore, the RK fit of the CCI data set, $\Delta s^{\text{RK}}(x)$, will be used as reference entropies in the following where the entropy of the mixture at the reference point for arbitrary x is given by:

$$s(x) = \Delta s^{\text{RK}}(x) - (1-x)s(0) - xs(1), \quad (4.2.1)$$

where $s(0)$ and $s(1)$ are the CCI entropies of H and He, respectively.

4.3 Entropies for arbitrary pressures and temperatures

As mentioned before, the strategy is to use thermodynamic integration via the equation of state (TI), Eq. (2.6.2), to obtain entropies for arbitrary pressures and temperatures. The entropies at the reference point computed with CCI were shown in the previous section, Fig 4.2.2 and 4.2.3.

First, it should be demonstrated that TI is able to yield the same results as coupling-constant integration, and is therefore thermodynamically consistent. For this purpose, CCI entropies were calculated at a constant temperature of 10 000 K for different Wigner-Seitz radii for a He fraction of $x = 0.0756$, which are shown in Fig 4.3.1 as a function of pressure. These calculations were performed for the vdW-DF and the PBE functional. Also shown are PBE CCI results from Militzer and Hubbard [141]. The CCI calculations with PBE agree with those of Ref. [141]. The vdW-DF entropies for the same Wigner-Seitz radii also agree with the PBE entropies within $0.006 k_B/\text{atom}$ but the vdW-DF yields higher pressures at a given density. Additionally, entropies obtained with the 2PT-MF method calculated for the PBE functional are shown. These entropies deviate significantly from the CCI entropies as already shown in Fig. 4.2.2. The dashed lines are TI results using Eq. (2.6.2). For each method separately (CCI using PBE, CCI using vdW-DF, and 2PT-MF using PBE), the reference entropy that determines the constant G_0 was chosen to be the entropy value at $r_s = 1.4 a_0$. The TI curves agree perfectly with the CCI results for the PBE functional and the vdW-DF. The 2PT-MF method, despite overestimating the entropy significantly, yields entropies that do not reproduce the thermodynamic integration via the equation of state. This suggests, that the 2PT-MF method does not produce entropies that are thermodynamically consistent with the equation of state. Figure 4.3.2 shows the entropy of mixing for the vdW-DF as function of x for different T at a constant Wigner-Seitz radius of $r_s = 1.4 a_0$. Symbols are CCI calculations. The black solid line is a Redlich-Kister (RK) fit [241] of 4th order of the 10 000 K data, see Eq. (2.5.22). The other coloured lines have been obtained using TI where the reference entropy for every He fraction is the RK fit of the 10 000 K CCI data. For 12 000 K and 15 000 K, the CCI entropies agree with TI within the given error bars except for 15 000 K at $x = 0.9$ where the TI yields slightly higher entropies. Nevertheless, the thermodynamic integration via the equation of state is

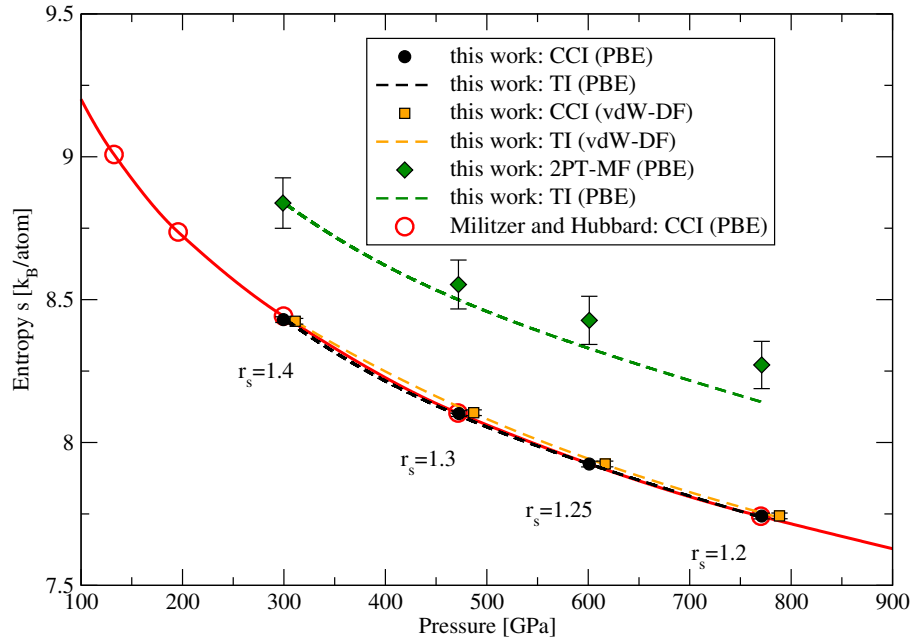


Figure 4.3.1: Entropy at 10 000 K for a H-He mixture with $x = 0.0756$ as function of pressure. The CCI entropy for four different densities using the PBE functional (black circles) and the vdW-DF (orange squares) is shown. The 2PT-MF entropy has been evaluated for the PBE functional. PBE and vdW-DF calculations have been performed for four Wigner-Seitz radii r_s given in atomic units. Dashed lines are obtained using Eq. (2.6.2), where the constant G_0 was determined from the entropy value at $r_s = 1.4 a_0$ for the corresponding method. The black and green TI curves for PBE are thus only shifted by the constant G_0 . Red open circles are from Ref. [141].

well suited to obtain entropies at arbitrary pressures and temperatures. Most importantly, this figure shows that the non-ideal entropy of mixing deviates significantly from the temperature-independent ideal entropy of mixing shown as dot-dashed line. The inclusion of non-ideal effects will therefore significantly alter the miscibility diagram.

In the following, the technical procedure to calculate entropies at arbitrary pressures and temperatures will be explained in more detail. It is based on the fact that thermodynamic integration can be performed along isobars as well as isotherms to obtain entropies in the required $p - T$ space. Starting from the obtained reference entropies at a temperature of 10 000 K and a Wigner-Seitz radius of $1.4 a_0$, the first step is to use Eq. (2.6.2) to calculate the entropy as a function of pressure for all considered He fractions for the constant reference temperature of 10 000 K. The

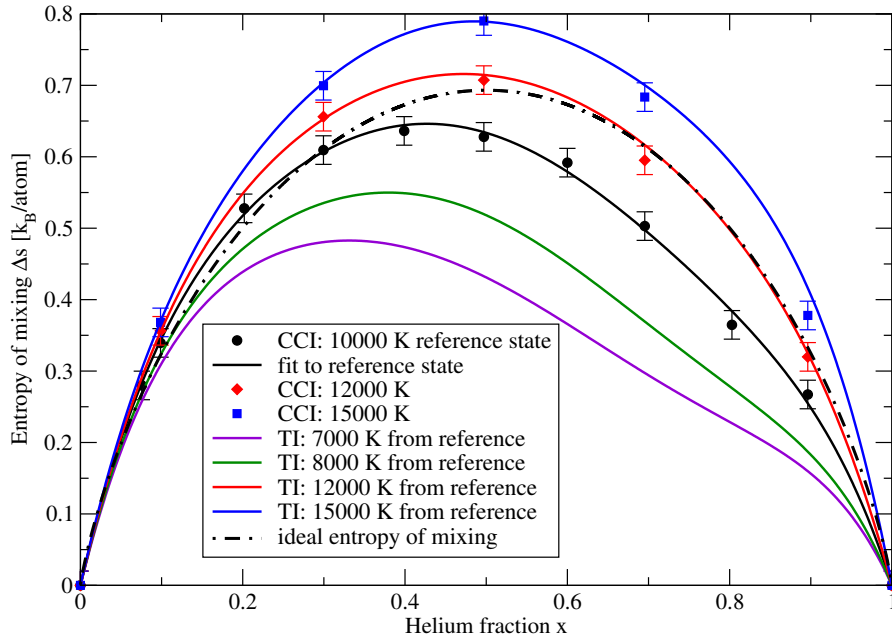


Figure 4.3.2: Entropy of mixing for five temperatures at a Wigner-Seitz radius of $r_s = 1.4 a_0$. Symbols are CCI calculations. Black solid line is a RK fit of 4th order of the CCI data. Colored solid lines are obtained using TI, Eq. (2.6.2), where the reference entropy is the RK fit of the 10 000 K CCI data.

constants G_0 for each He fraction are given by the CCI entropies of the reference state and their respective energy and pressure. The integration requires volume as function of pressure, see Eq. (2.6.2). In Ch. 3 it was demonstrated that $v(p)$ can be fitted very accurately using Eq. (3.1), which can be easily integrated numerically. The obtained entropy at 10 000 K for all He fractions is represented on a dense grid of pressures, due to the numerical integration. The second step is to calculate the entropy for different temperatures. Again, Eq. (2.6.2) is applied but for a single fixed pressure. A pressure of 3 Mbar was chosen to obtain the entropy on an isobar. This choice was motivated by two factors: First, the pressure is high enough to be beyond the first-order LL-IMT in liquid hydrogen, cf. the LL-IMT for the vdW-DF in Fig. 1.2.1. Second, the chosen pressure is in a region where a sufficient amount of EOS data points has been calculated for all considered temperatures. For this chosen pressure, energies and volumes in the temperature range from 1 000 to 15 000 K have been fitted to a fourth order polynomial as a function of temperature. Using these fits, Eq. (2.6.2) has been evaluated, where the constant G_0 at 3 Mbar is available from the first step. Again, the integration is performed numerically and entropies are given on a grid, that is equal to the grid of the simulated temperatures, i.e. from

1 000 K to 15 000 K in steps of 1 000 K. A much finer grid could be calculated, if the EOS data had been fitted in both p and T simultaneously. However, the accuracy of such a fit is inferior to only pressure-dependent fit functions for each individual temperature independently. The third step is to repeat the first step but for every temperature, i.e. to calculate the entropy on the given isotherm via Eq. (2.6.2). The constants G_0 for every temperature are now given by the entropies obtained in the previous step.

The described procedure yields entropies on a dense pressure grid for all considered temperatures that are used in Ch. 5 to construct the Gibbs free energy of mixing. Nuclear quantum corrections to the EOS and the entropies will also be discussed in the following chapter.

Chapter 5

Gibbs free energy of mixing of H-He mixtures

In this chapter, the Gibbs free energy of mixing is shown for hydrogen-helium mixtures. In the first section, the Gibbs free energies of mixing for the exchange-correlation functionals PBE and vdW-DF are compared. In Sec. 5.2, the nuclear quantum corrections to the Gibbs free energy of mixing are discussed. Finally, the total Gibbs free energy of mixing is shown for different $p - T$ conditions.

5.1 Comparison of PBE and vdW-DF results

Previous DFT-MD calculations targeting the miscibility of hydrogen and helium have been performed using the PBE functional [65, 85, 134–136]. Here, a comparison of the Gibbs free energy of mixing between the PBE functional and the vdW-DF is made. The PBE data by Lorenzen *et al.* have been obtained using the ideal entropy of mixing [134], so that, in a first step, this approximation is used for a direct comparison. In Fig. 5.1.1, the Gibbs free energy of mixing is shown for the vdW-DF and the PBE functional. Temperatures from 3 000 K to 11 000 K are shown for a pressure of 4 Mbar. The dashed straight lines and dot-dashed lines represent the common tangent construction to the PBE data and the vdW-DF data, respectively. Both vdW-DF and PBE results show demixing for temperatures up to 10 000 K (not shown in the figure), apparent by the double-well structure and regions with negative curvature, see Sec. 2.5 on the explanation of the thermodynamics of binary systems. At a temperature of 11 000 K, no negative curvature can be seen: thus, the system is in a well mixed state. Compared to PBE, the vdW-DF leads to significantly lower enthalpies of mixing. This effect is more pronounced for the He-rich side of the figure.

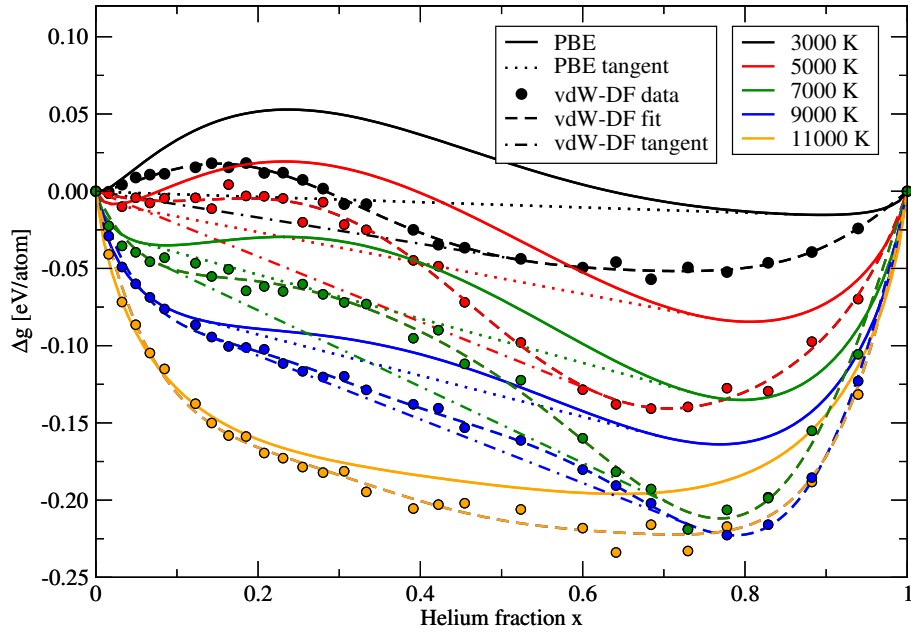


Figure 5.1.1: Comparison of the Gibbs free energy of mixing at 4 Mbar for various temperatures (colour coded) between the PBE and the vdW density functional. The PBE curves have been taken from Lorenzen *et al.* [134]. The ideal entropy of mixing has been used.

The common tangent construction which determines the He fractions of the He-poor, x_1 , and He-rich, x_2 , phases results in significantly different He fractions of the He-rich phase for both functionals. For 3000 K, the vdW-DF leads to a much lower x_2 than PBE. For increasing temperature, x_2 increases significantly for the vdW-DF functional and decreases slightly for the PBE functional, see also Fig. 6.1.1 in the upcoming Ch. 6 for a comparison of the vdW-DF and PBE miscibility diagram.

5.2 Nuclear quantum corrections to the Gibbs free energy of mixing

Nuclear quantum corrections (NQC) to the Gibbs free energy g^{QC} can be calculated from the nuclear quantum corrections to the free energy f^{QC} :

$$g^{\text{QC}}(x, p, T) = f^{\text{QC}}(x, p, T) + p^{\text{QC}}(x, p, T)v(x, p, T), \quad (5.2.1)$$

where $p^{\text{QC}}(x, p, T)$ is the NQC to pressure that is determined from f^{QC} in the further course of this section. Note, that the total pressure p includes the NQC to pressure

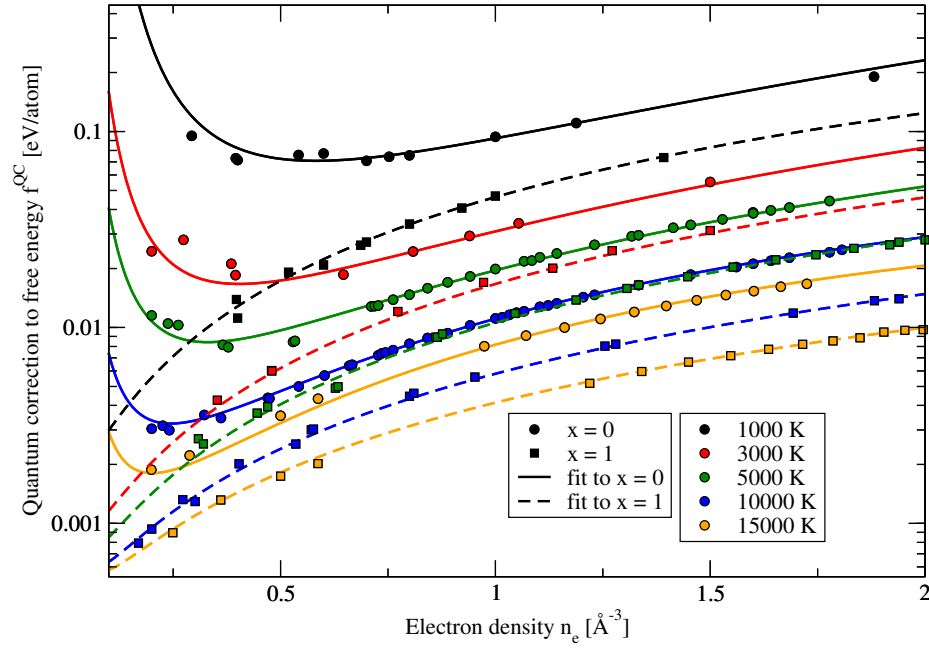


Figure 5.2.1: Quantum corrections to the free energy for pure H and pure He as a function of electron density for various temperatures (colour coded). Lines are fits according to Eq. (5.2.3).

now. The corresponding NQC to the Gibbs free energy of mixing is then

$$\Delta g^{\text{QC}}(x, p, T) = g^{\text{QC}}(x, p, T) - (1 - x)g^{\text{QC}}(0, p, T) - xg^{\text{QC}}(1, p, T). \quad (5.2.2)$$

First, the NQC to the free energy have been obtained using Eq. (2.4.17). The free energy per particle f^{QC} was then fitted (for each He fraction separately) to the following two-dimensional function

$$f^{\text{QC}}(n_e, T) = \exp \left[\sum_{i=0}^3 \sum_{\substack{j=0 \\ i+j \leq 3}}^2 A_{i,j} \ln(n_e)^i \ln(T)^j \right], \quad (5.2.3)$$

where $n_e = N_e/V$ is the electron density and $A_{i,j}$ are fit coefficients. The use of the electron density instead of the particle or mass density, or the volume is an arbitrary choice only motivated by the numerical implementation of the data processing routines. In Fig. 5.2.1, the NQC data and their fits for pure H and pure He as a function of electron density is shown for five temperatures. For pure He, the quantum corrections to the free energy increase with increasing density and decrease with increasing temperature. For pure H, the general trend is similar except that at low densities, the NQC exhibit a minimum followed by a slight increase for even lower

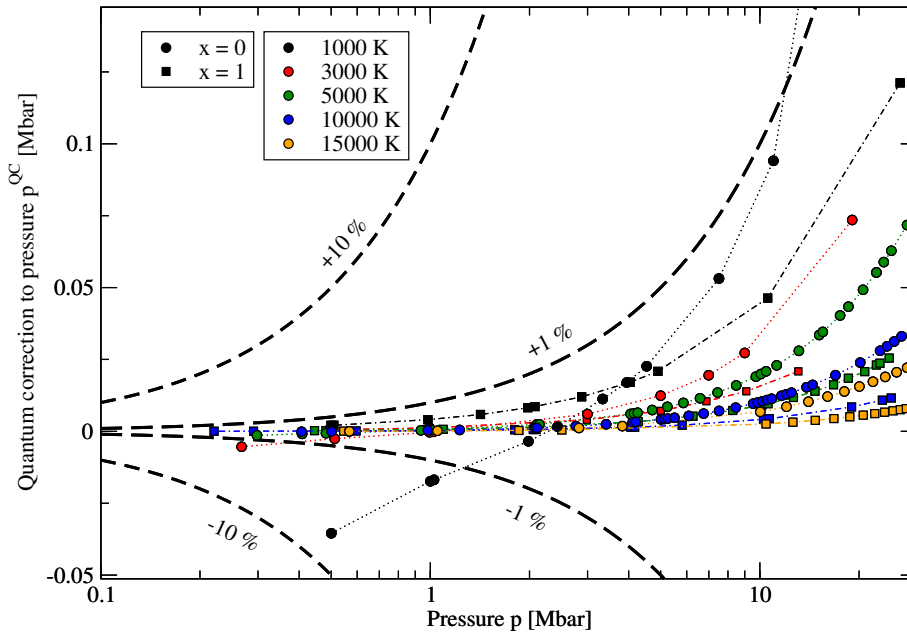


Figure 5.2.2: Quantum corrections to the pressure for pure H and pure He as a function of total pressure for various temperatures (colour coded). Lines are guides to the eye. Dashed lines mark the percental fraction of the NQC to the total pressure.

densities. This behaviour can be explained by the pressure induced dissociation of hydrogen molecules with increasing density. In the molecular phase at low densities, the NQC are stronger because of molecular vibrations, which can be seen in the VDOS. The dissociation of H_2 leads to a visible decrease of NQC, followed by an increase with density.

A volume dependent NQC to the free energy results in a quantum correction to pressure. These can easily be obtained from the fit function Eq. (5.2.3) as:

$$p^{QC} = \frac{n_e^2}{1+x} \frac{\partial f^{QC}}{\partial n_e}, \quad (5.2.4)$$

where the He fraction in the term $(1+x)^{-1}$ is needed to translate electron number N_e to particle number N , i.e. $N_e = (1+x)N$. In Fig. 5.2.2, the quantum corrections to pressure are shown as a function of total pressure for pure hydrogen and pure helium for five temperatures, similar to Fig. 5.2.1. For hydrogen, the NQC to pressure are negative for low pressures and temperatures as expected by the shape of the NQC to free energy in Fig. 5.2.1. For higher pressures, the NQC to pressure increase and become positive. For helium, the NQC to pressure are positive for all temperatures and also show an increase with pressure. For both pure H and He, the absolute value of p^{QC} decreases with increasing temperature. The dashed lines show the percental

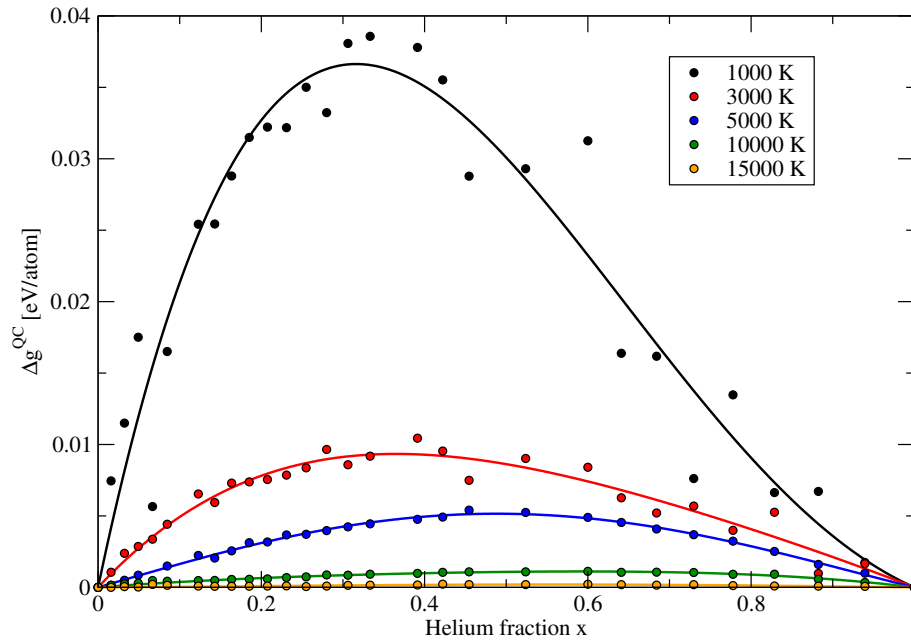


Figure 5.2.3: Quantum corrections to the Gibbs free energy of mixing at 1 Mbar for various temperatures (colour coded). Solid lines are Redlich-Kister fits of 3rd order.

fraction of p^{QC} to the total pressure. For most data points, the NQCs to pressure are less than 1% of the total pressure, except for hydrogen at 1000 K, where p^{QC} makes up to 7.6% of the total pressure at 0.5 Mbar. Thus, quantum corrections to pressure are only important for the lowest temperatures and pressures considered here and could otherwise be neglected entirely due to their low magnitude. However, it is apparent from Fig. 5.2.1 that the fit is a major source of uncertainty for those small pressures. It overestimates the slope and especially the change in slope at low densities. The fit could be improved if the NQC to free energy was fit to a density-dependent function for each temperature separately.

Using the NQC to the free energy and the derived pressure correction, the quantum corrections to the Gibbs free energy of mixing have been calculated. These are shown in Fig. 5.2.3 for a pressure of 1 Mbar and in Fig. 5.2.4 for a pressure of 10 Mbar. Lines are RK fits of third order. At 1 Mbar, the NQCs to the Gibbs free energy of mixing are positive for all He fractions and temperatures. Thus, the NQCs reduce the miscibility of H and He, because the total Gibbs free energy of mixing is increased. At 1000 K, the NQCs to the Gibbs free energy of mixing are largest. They decrease with increasing temperature as expected from the previous figures. The scatter of the data points is largest for 1000 K because the convergence of the VDOS is slow due to the low particle velocities and numbers. At these low temperatures,

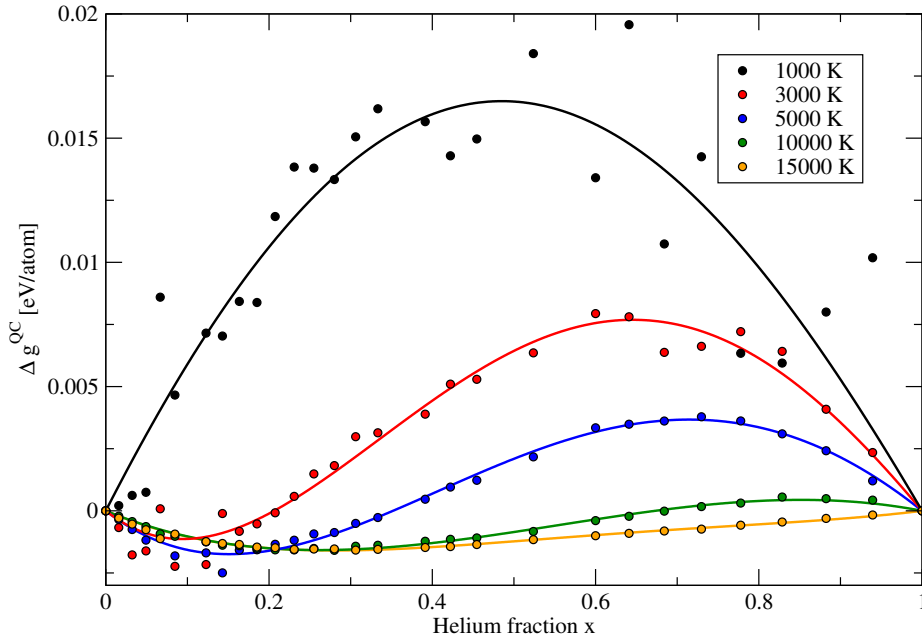


Figure 5.2.4: Quantum corrections to the Gibbs free energy of mixing at 10 Mbar for various temperatures (colour coded). Solid lines are RK fits of 3rd order.

the simulations would need to run much longer to obtain better statistics. However, given the large number of computations and the limited computational resources, the obtained accuracy is sufficient for the NQC to the Gibbs free energy of mixing. In Fig. 5.2.4, the contribution of NQC to the Gibbs free energy of mixing is generally smaller at 10 Mbar than at 1 Mbar. For 1000 K, Δg^{QC} is positive for all He fractions, which again favours the demixing. For higher temperatures, Δg^{QC} shows different features than before. For 3000 K, 5000 K, and 10000 K, the NQC to the Gibbs free energy of mixing is negative for small He fractions. For 15000 K, Δg^{QC} is negative for all He fractions, which favours the miscibility of hydrogen and helium. However, NQCs at 10 Mbar are too small to influence the total Gibbs free energy of mixing significantly as will be discussed in the next section.

5.3 Total Gibbs free energy of mixing for the vdW-DF

The Gibbs free energy of mixing has been calculated using the DFT-MD data and the entropies obtained via CCI and TI, see Ch. 4. Nuclear quantum corrections (NQC) have been added. The total Gibbs free energy (per particle) is thus given by

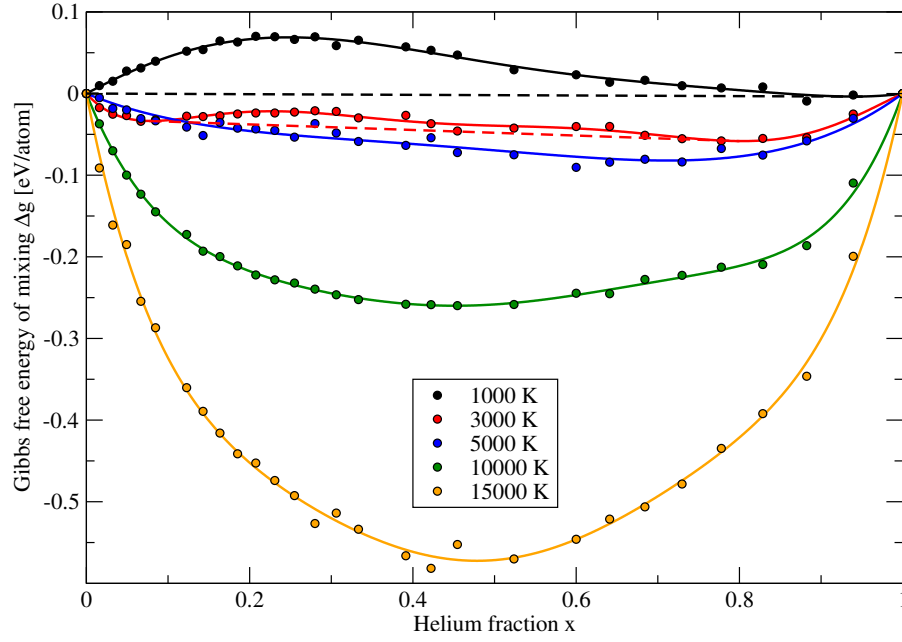


Figure 5.3.1: Total Gibbs free energy of mixing (including quantum corrections) at 1 Mbar for various temperatures (colour coded). Solid lines are RK fits of 5th order and straight dashed lines show the double tangent construction to Δg where it applies.

$$g(x, p, T) = u^{\text{DFT}}(x, p, T) - Ts^{\text{TI}}(x, p, T) + g^{\text{QC}}(x, p, T) + p^{\text{DFT}}v(x, p, T), \quad (5.3.1)$$

where $u^{\text{DFT}}(x, p, T)$ is the total energy of the DFT-MD simulations, $s^{\text{TI}}(x, p, T)$ is the entropy obtained via thermodynamic integration as explained in Ch. 4, and $p = p^{\text{DFT}} + p^{\text{QC}}$ is the sum of DFT-MD pressure and NQC to pressure.

In Figures 5.3.1 and 5.3.2, the total Gibbs free energy of mixing is shown for five temperatures and a pressure of 1 Mbar and 10 Mbar, respectively. Redlich-Kister fits of 5th order have been applied to the total Gibbs free energy of mixing. The common tangent construction has been numerically applied to the Redlich-Kister fits and is shown where it can be constructed. The Gibbs free energy of mixing shows demixing for temperatures up to 3000 K at 1 Mbar (Fig. 5.3.1). In this temperature and pressure range, the NQC contribute significantly to the total Gibbs free energy and enhance the insolubility. There would be no demixing at 3000 K without nuclear quantum effects. For higher temperatures, the NQC still tend to favour complete demixing, but are already small enough that no demixing can be seen in the total Gibbs free energy. At 10 Mbar (Fig. 5.3.2), demixing is present

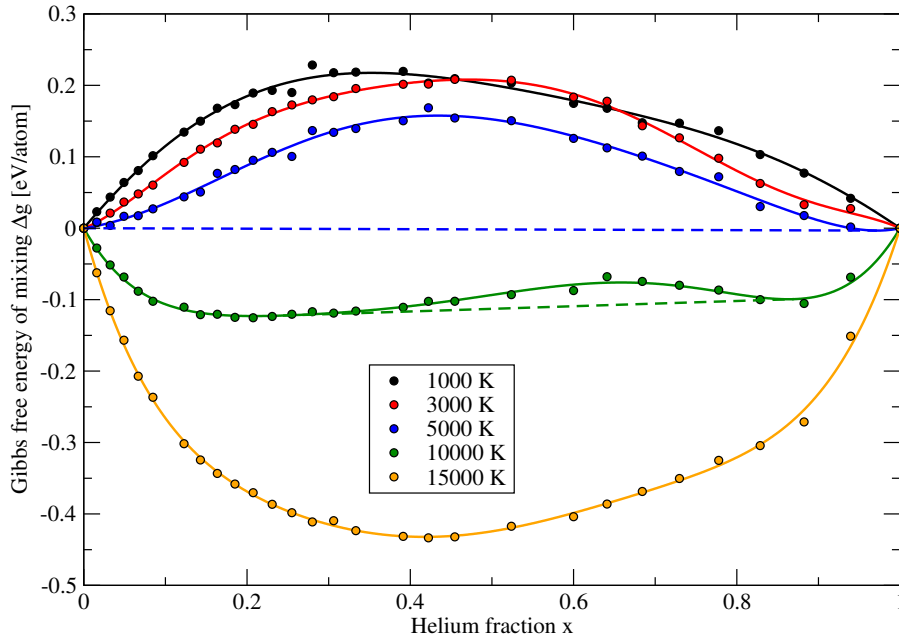


Figure 5.3.2: Total Gibbs free energy of mixing (including quantum corrections) at 10 Mbar for various temperatures (colour coded). Solid lines are RK fits of 5th order and straight dashed lines show the double tangent construction to Δg where it applies.

up to temperatures of 11 000 K (10 000 K is the highest shown temperature in the figure, where demixing occurs). The contribution of NQC at 10 Mbar is less than 1% and their effect is too small to influence the total Gibbs free energy. At 10 Mbar, the 1000 K curve intersects with the 3000 K curve, which is an unexpected behaviour for the Gibbs free energy of mixing, because it does not occur if the ideal entropy of mixing is used or if the Helmholtz energy is visualised. Thus, the crossing must be caused by the non-ideal entropy of mixing, which is higher for the lower temperature. Still, the demixing into the pure components is not altered by this crossover and there is no argument why the Gibbs free energy of mixing for different temperatures should not intersect. Furthermore, at 10 Mbar and 1 000 K, He should be solid, while at 3 000 K He starts to melt according to Fig. 1.2.2, which eventually influences the Gibbs free energy of mixing.

In total, the Gibbs free energy of mixing has been calculated for pressures of 0.5 Mbar, 1 Mbar, 1.2 Mbar, 1.5 Mbar, 2 Mbar, 4 Mbar, 10 Mbar, 24 Mbar, and 30 Mbar. The calculation of additional, intermediate pressures is possible, but the obtained grid is already sufficient for the construction of a complete miscibility diagram in that pressure range.

Chapter 6

Miscibility diagram

This chapter discusses the main results of this thesis: the miscibility gap of hydrogen-helium mixtures obtained using the vdW-DF XC functional and non-ideal entropy of mixing. First, the PBE demixing phase diagram of Lorenzen *et al.* [65, 134] is compared to the vdW-DF results that were obtained using the ideal entropy of mixing. Thus, the influence of the XC-functional is directly visualized for the complete miscibility diagram. Second, the influence of non-ideal entropy effects on the vdW-DF miscibility diagram is demonstrated by comparing the previously shown ideal entropy case with the non-ideal entropy case, which has a paramount impact on the miscibility diagram. In the last section, the demixing phase diagram for chosen He abundances is presented and compared to calculations by Morales *et al.* [136] and Lorenzen *et al.* [65, 134].

6.1 Miscibility gap for PBE and vdW-DF using the ideal entropy

To illustrate the effect of the XC-functional, a comparison of the miscibility diagrams for PBE [65, 134] (solid lines and coloured areas) and the vdW-DF (circles and dot-dashed lines) using the ideal entropy of mixing computed in this work is shown in Fig. 6.1.1. No nuclear quantum corrections have been taken into account because neither have they been taken into account by Lorenzen *et al.* [65, 134]. Demixing temperatures are given as a function of He fraction for different colour coded pressures. The dot-dashed lines are smoothing splines [259] to the circles and act as a guide to the eye. The coarseness of the temperature grid confines the critical temperature to an interval of 1 000 K. Thus, the splines have been restricted to show a maximum between the highest T where demixing could be numerically

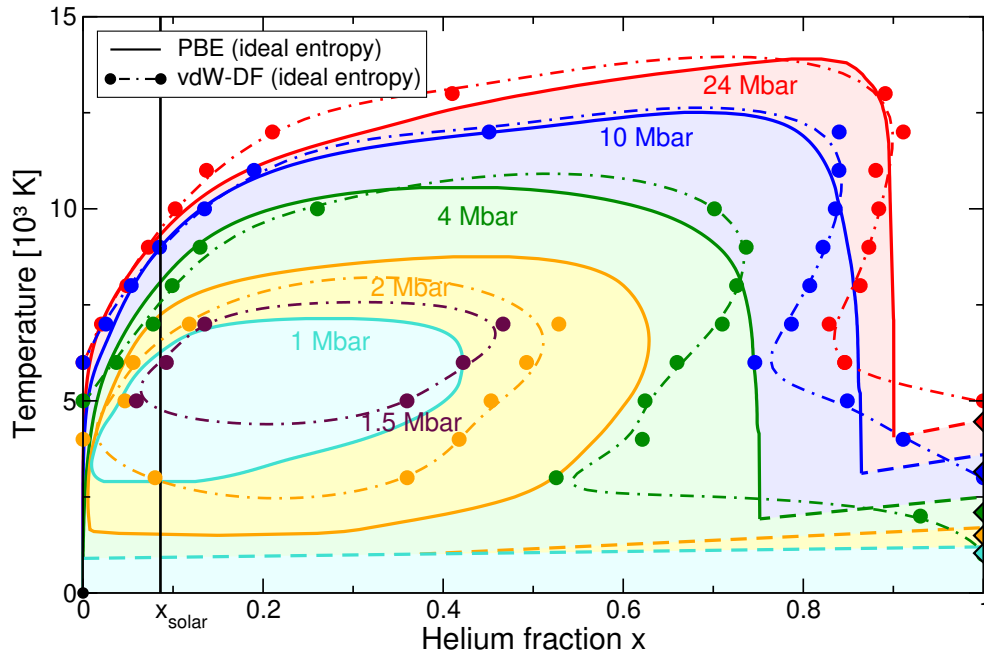


Figure 6.1.1: Miscibility gap of hydrogen-helium mixtures using the ideal mixing approximation. Dot-dashed lines are smoothing splines to the data points. Colours indicate the pressures. The coloured areas confined by solid lines are PBE results by Lorenzen *et al.* [65, 134].

determined and the next higher T where no demixing could be seen. First, it is important to note that both functionals show the effect of demixing in a similar way. There are certain differences in the demixing temperatures and pressures but the overall appearance is comparable. Nevertheless, there are three main differences between PBE and vdW-DF: first, the vdW-DF shows no sign of demixing for pressures below 1.5 Mbar. The lowest demixing pressure for the PBE functional is at 1 Mbar. The vdW-DF shifts the demixing pressures up by 0.5 Mbar compared to PBE. This shift towards higher pressures (relative to PBE) also appears for the metallisation transition [83] and the thermal equation of state in pure hydrogen and in pure helium as seen in Ch. 3 especially for lower pressures. The demixing regions for 1.5 Mbar and 2 Mbar form island structures similar to the PBE results, which are well separated from the liquidus line. The second difference is the vertical edge in the demixing temperatures appearing for PBE at 4 Mbar, 10 Mbar, and 24 Mbar at high He-fractions, which is different for the vdW-DF. There, a tilt towards lower He-fractions is obtained. As already discussed in the introduction, Sec. 1.3, this edge is due to the metallisation in the hydrogen subsystem, which is only possible

up to a critical He concentration, where the presence of He atoms inhibits the delocalization of H electrons, such that short lived H_2 molecules form again or, at least, increased molecular correlations are visible in the simulation box. From Fig. 6.1.1, it becomes apparent that a higher He concentration is necessary to inhibit the metallisation of the H subsystem for increasing pressure. For the vdW-DF the critical He fraction is temperature-dependent for all considered pressures, while for PBE it becomes temperature-independent for pressures greater than 4 Mbar. In general, higher temperatures favour mixing but also weaken the localisation of electrons, so that these two effects balance each other in PBE. However, that is not true for the vdW-DF results, where the demixing region is increased with temperature. The discussed behaviour is only apparent above a particular temperature. Below this temperature a kink appears, where the demixing region extends to higher He fractions. A complete separation into the pure components occurs below a certain temperature. For each pressure, this coincides with the melting temperatures of He (coloured diamonds at $x = 1$) and reveal the liquidus line of H-He mixtures. The last difference between the PBE and vdW-DF miscibility diagram is that for the solar He abundance, demixing temperatures for the vdW-DF are lowered compared to PBE especially for low pressures. This will be seen more clearly in Fig. 6.3.1 in Sec. 6.3, and it is a direct consequence of the shift to higher pressure by the vdW-DF compared to PBE, shown in Ch. 3.

6.2 Miscibility gap for the vdW-DF using the ideal and non-ideal entropy

In this section, the complete miscibility diagram using the non-ideal entropy is presented. Nuclear quantum corrections discussed in Ch. 5 are now taken into account, but their influence is minor compared to the effect of non-ideal entropy. In Fig. 6.2.1, the miscibility diagram with the vdW-DF using both ideal entropy and non-ideal entropy is shown. Solid lines and dot-dashed lines are smoothing splines corresponding to the coloured circles similar to Fig. 6.1.1. The inclusion of non-ideal effects in entropy has major consequences for the whole demixing phase diagram. In total, four striking differences can be seen: first, demixing temperatures are lowered significantly at high pressures. This consequence is particularly important for small He abundances relevant for Jupiter and Saturn, whose mean He content should be similar to the solar He abundance. It will be shown in the next section, how demixing temperatures are shifted at solar He abundance and in Ch. 7, the

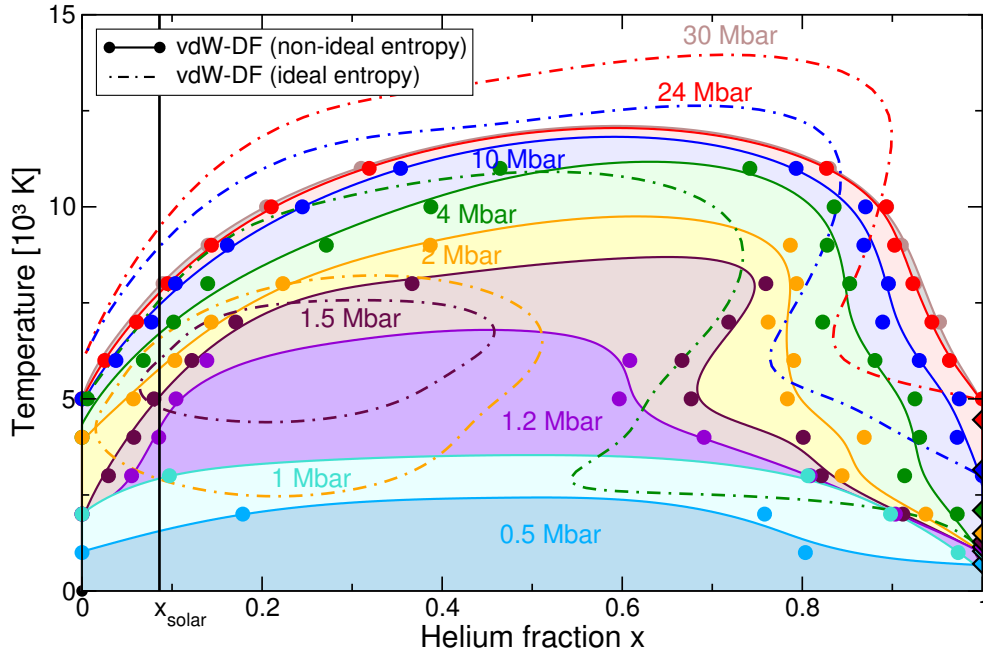


Figure 6.2.1: Miscibility gap of hydrogen-helium mixtures using the vdW-DF. Dot-dashed lines are the same as in Fig. 6.1.1. Solid lines are smoothing splines to the data points that include non-ideal effects in the entropy.

implications for Jupiter and Saturn are discussed. The second difference is that the demixing region using non-ideal entropy extends to pressures smaller than 1.5 Mbar, which directly removes the island-like structure that appeared when using the ideal entropy. The first two changes have already been anticipated in Ch. 1, Sec. 1.3, by comparing the work of Morales *et al.* [136] to the work of Lorenzen *et al.* [65, 134], where the demixing temperatures and the low-pressure miscibility diagram have been significantly altered due to the inclusion of the non-ideal entropy. As a third difference, it can be seen that the kink at high He fractions in the ideal entropy calculations is smoothed out significantly at pressures above 2 Mbar. At pressures of 1.5 Mbar and 1.2 Mbar, there is still a small sign of this effect but not as apparent as in the ideal entropy calculation. The fourth difference concerns the size of the demixing region, which is increased especially for pressures of 1.5 Mbar, 2 Mbar, and 4 Mbar by shifting the He fractions of the He-rich phase towards higher x . Due to uncertainties in the underlying DFT-MD data and in the Redlich-Kister fit of ΔG , it is estimated that the uncertainty in the He fractions of the He-rich and He-poor phases of the miscibility gap are $\delta x = \pm 0.02$, which has to be taken into account when calculating the planetary evolution.

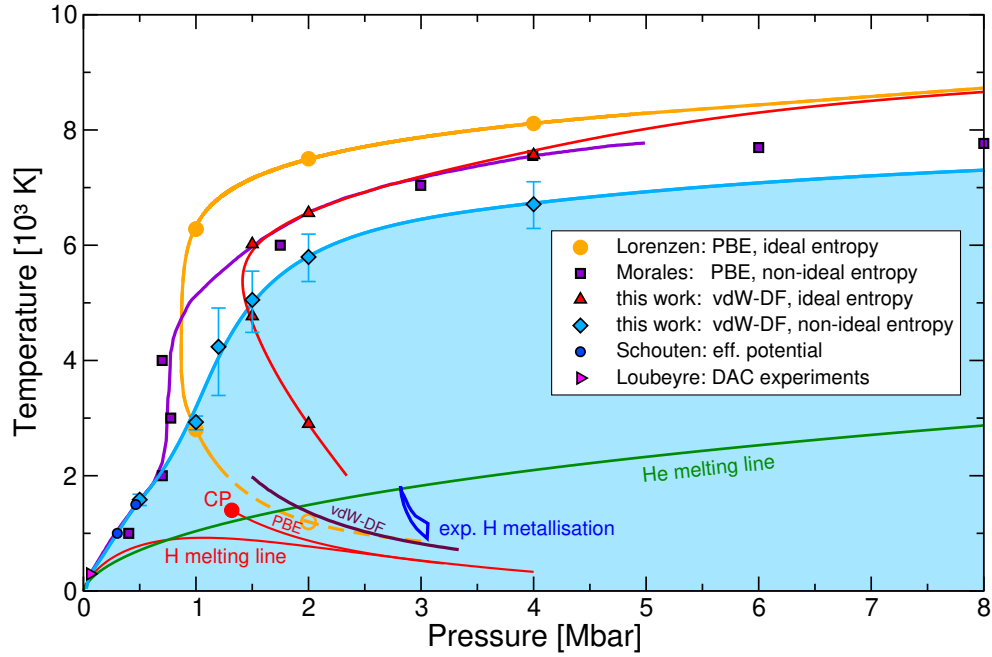


Figure 6.3.1: Miscibility gap of hydrogen-helium mixtures at solar Helium abundance. Theoretical results from Lorenzen *et al.* [65, 134], Morales *et al.* [136] and Schouten *et al.* [123] are shown. DAC experiments have been performed by Loubeyre *et al.* [122].

6.3 Miscibility gap for solar He concentration

In Fig. 6.3.1, the miscibility diagram for the mean solar He concentration $x_{\text{solar}} = 0.086$ is shown, which is relevant for the giant gas planets Jupiter and Saturn. The miscibility regions from PBE and vdW-DF calculations are compared, and for each functional both ideal and non-ideal entropy of mixing are shown. Error bars for the vdW-DF demixing temperatures for the non-ideal entropy case have been obtained by simply shifting the smoothing splines by $\delta x = \pm 0.02$, which results in a shift in demixing temperatures at the solar He abundance x_{solar} . The size of the error bars is thus directly related to the slope of the miscibility region and most pronounced at a pressure of 1.2 Mbar.

A comparison between the PBE data sets using ideal and non-ideal entropy has already been done in Sec. 1.3 so that the focus here is on comparing the vdW-DF results to their PBE counterparts. The differences between vdW-DF and PBE, that have been discussed in the two previous sections, are also pronounced at solar He composition: for the ideal entropy case a significant shift to higher pressures can be seen for the vdW-DF. This shift contributes to the lowering of the demixing

temperatures compared to PBE at pressures below 8 Mbar. For low temperatures, the island-like structure in the ideal entropy calculations results in a negative slope of the demixing phase boundary. The calculations using the non-ideal entropy do not show this behaviour. Instead, both the PBE and vdW-DF results confirm the calculations of Schouten *et al.* [123], who performed Monte Carlo simulations of H-He mixtures in the Gibbs ensemble [144] using effective pair-potentials. This special ensemble allows to simulate phase equilibria by ensuring equal chemical potentials in both phases. Thus, the concentration of the He-rich and He-poor phases can directly be visualized within the simulation boxes. The vdW-DF calculations using the non-ideal entropy are in excellent agreement with these data. The DAC experiments of Loubeyre *et al.* [122] can be reproduced, if the combined data is extrapolated to lower pressures. When comparing the vdW-DF and PBE calculations obtained with non-ideal entropy, it can be seen that the vdW-DF yields demixing temperatures that are on average 1000 K lower for pressures greater than 0.7 Mbar. It will be shown in the next chapter, that the new results have major consequences for planetary models of Jupiter and Saturn.

Chapter 7

Planetary isentropes

In the previous chapter, the miscibility diagram using the vdW density functional and non-ideal entropy has been presented and significant shifts compared to previous demixing phase diagrams have been identified. Most notably, the shown demixing temperatures were significantly decreased. In this chapter, it will be shown how the new miscibility diagram influences planetary models of Jupiter and Saturn. Furthermore, new $p - T$ profiles for Jupiter and Saturn will be calculated using the obtained vdW-DF EOS and entropy data. In the first section, it will be explained how the new $p - T$ profiles have been obtained and why they are only simple models. Then, in the second section, the calculated interiors will be compared to other models and put into contrast to the miscibility diagram.

7.1 Calculating planetary $p - T$ profiles

The pressure profile of a planet can be calculated by employing differential equations for the hydrostatic equilibrium and the mass distribution. For a spherical object these are [\[260\]](#):

$$\frac{dp}{dr} = -\frac{Gm(r)\varrho(r)}{r^2}, \quad (7.1.1)$$

$$\frac{dm}{dr} = 4\pi r^2 \varrho(r), \quad (7.1.2)$$

where G is the gravitational constant, $\varrho(r)$ is the mass density at radius r , and $m(r)$ is the integrated mass from the inside of the planet to r . The radius r is thus considered to be a coordinate, where $r = 0$ at the center of the planet and $r = R$ at the 1 bar level. The equation of state of the contained material is needed to relate pressure with mass density, but since the EOS also depends on temperature, one

additional equation is necessary - the temperature profile. In the theory of planetary modelling, the temperature gradient is often defined as the dimensionless quantity

$$\nabla_T = \frac{p}{T} \frac{dT}{dp} = \frac{d \ln T}{d \ln p}. \quad (7.1.3)$$

The gradient depends on the mechanism with that heat is transported from the inside to the outside of the planet. These mechanisms are conduction, radiation, and convection. If heat is only transported via radiation and conduction, the temperature gradient ∇_{rad} , could be calculated as [260–262]:

$$\nabla_{\text{rad}} = \frac{3}{4\pi\sigma G} \frac{\kappa l p}{m T^4}, \quad (7.1.4)$$

where l is the interior luminosity, σ is the Stefan-Boltzmann constant, and κ is the opacity that contains both contributions from radiation and conduction. If heat is transported primarily via convection, the temperature gradient ∇_T can be described by the adiabatic temperature gradient ∇_{ad} :

$$\nabla_{\text{ad}} = \left(\frac{d \ln T}{d \ln p} \right)_s, \quad (7.1.5)$$

where s denotes an evaluation of the derivative at constant entropy. The Schwarzschild criterion [263]:

$$\nabla_{\text{rad}} < \nabla_{\text{ad}} \quad (7.1.6)$$

then determines, if the medium is stable to convection. For Jupiter and Saturn, this criterion is likely violated for most $p - T$ conditions [261, 264–266] because of their high luminosities [267, 268]. Still, the opacities that enter Eq. (7.1.4) could be low enough to suppress convection under certain circumstances [261]: if only H-He mixtures are considered, the opacity at around 2000 K would be small enough to favour a radiative energy transport. Also the inclusion of water and methane would not increase the opacity above the critical opacity that is needed to violate Eq. (7.1.6) [261]. However, Guillot *et al.* [266] have shown that the presence of potassium and sodium would yield opacities high enough to ensure a convective interior. It can be shown [262] that convection leads to the case

$$\nabla_{\text{ad}} \simeq \nabla_T \ll \nabla_{\text{rad}}, \quad (7.1.7)$$

where almost all heat is transported via convection and the established temperature gradient ∇_T is very close to the adiabatic temperature gradient. Thus, as long as there are no first order phase transitions [269], core erosion [270], thermal boundary layers [271], or demixing transitions [272], the interior should be homogeneously

mixed and isentropic. The temperature profile is, thus, to a good approximation given by Eq. (7.1.5). The required thermodynamic path of constant entropy for a given material can be calculated in three ways: first, if the entropy is known for a given equation of state (either as a formula or discrete data), it is straight-forward to construct thermodynamic paths of constant entropy by numerically inverting the analytical expressions or interpolating the discrete simulation data. Second, if the entropy is not known, it is possible to use thermodynamic integration via the equation of state as described in Sec. 2.6. No knowledge about the actual entropy at a given reference state is required except that this reference condition on the isentrope has to be known. The temperature at the 1 bar level is often used for that purpose. The third method involves solving a differential equation, which also requires an initial state that is part of the isentropic path. This differential equation can be written as

$$\left(\frac{\partial T}{\partial V}\right)_s = -T \frac{\left(\frac{\partial p}{\partial T}\right)_V}{\left(\frac{\partial U}{\partial T}\right)_V}, \quad (7.1.8)$$

which can be derived by using Maxwell's relations [273] and other thermodynamic relations. In principle, the obtained set of V , p , and T should be self-consistently determined by additionally solving Eq. (7.1.1) and (7.1.2) to relate the thermodynamic conditions to the radius coordinate. This is required to fulfil all observational constraints. Furthermore, gravitational field data expressed in terms of gravitational moments J_n can hardly be reproduced using a completely homogeneous interior. Instead, two-layer or three-layer models are required, with a different composition in each layer [262]. In a first step however, it is not necessary to determine a fully self-consistent and observationally constrained three-layer model to answer the question if the immiscibility of H-He mixtures is relevant for Jupiter and Saturn. A simple $p - T$ profile consisting only of hydrogen and helium is sufficient to compare to the miscibility diagram obtained in the previous chapter. Such simplified models have been calculated for Jupiter and Saturn based on the vdW-DF EOS and entropy data and will be discussed in the next section.

7.2 Profiles for Jupiter and Saturn

Isentropes for Jupiter and Saturn are fully determined by their entropy value. At the 1 bar level, Jupiter has a temperature of 166.1 K [274], measured by the Galileo entry probe, whereas Saturn is slightly cooler with a temperature of 135 K [57]. If only H and He are considered the corresponding entropy can be easily determined. In Fig. 7.2.1, the entropy at 1 bar for H, He, and a mixture with $x = 0.07563$ is

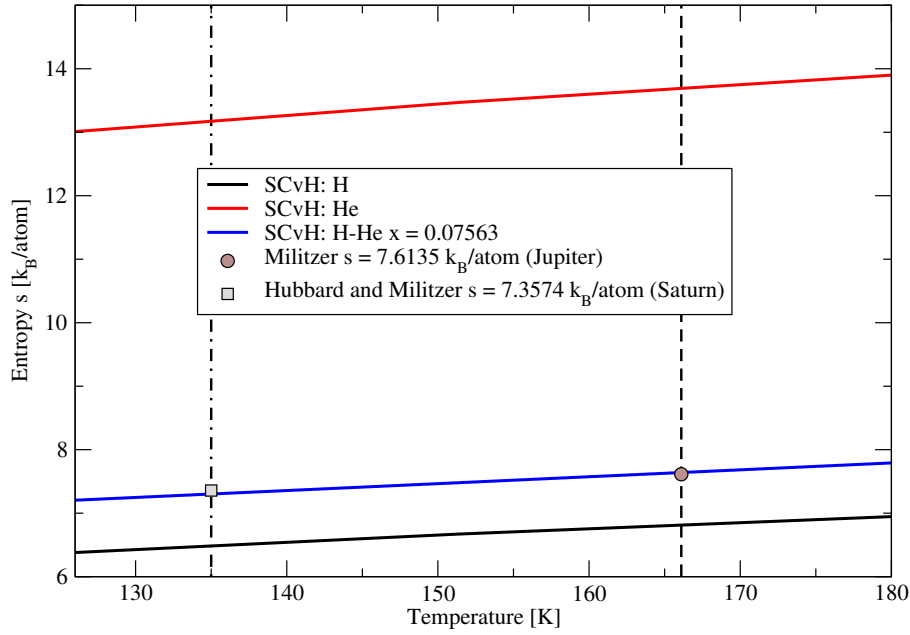


Figure 7.2.1: Entropy for hydrogen, helium and a linear mixture with helium fraction $x = 0.07563$ at $p = 1$ bar according to the EOS of Saumon, Chabrier, and van Horn (SCvH) [258]. The temperatures of Saturn (dot-dashed) and Jupiter (dashed) for that pressure are shown as vertical black lines.

shown as a function of temperature. These entropies have been taken from the EOS of Saumon, Chabrier, and van Horn (SCvH) [258], who calculated the free energy of pure H and pure He within a free energy minimization scheme using a chemical model. Note that the nuclear spin entropy of H, $s_{\text{nuc}} = \ln 2 k_B$, has been subtracted. For the considered mixture, the H and He EOS have been linearly mixed and the ideal entropy of mixing has been added. Here, the ideal entropy approximation is valid because at 1 bar, H and He behave as ideal gases. The He fraction $x = 0.07563$ corresponds to a mass fraction of $Y = 0.245$, which is slightly higher than the Jupiter value determined by the Galileo entry probe $Y_J = 0.238 \pm 0.04$. For Saturn the value is within the reanalysed Voyager data $Y_S = 0.18 \dots 0.25$, but outside of the Cassini data $Y_S = 0.16 \dots 0.22$. Calculations of the EOS and entropy data for this particular He fraction have been performed by Militzer [142] using DFT simulations with the PBE functional. These results were subsequently used by Hubbard and Militzer [114] to calculate a new Jupiter model and an isentrope for Saturn's entropy value. In Fig. 7.2.1, their entropy values are marked by the symbols. The Jupiter value $s = 7.6135 k_B$ and the Saturn value $s = 7.3574 k_B$ agree with the SCvH entropy at the respective temperature within 1%. To obtain models with the same He

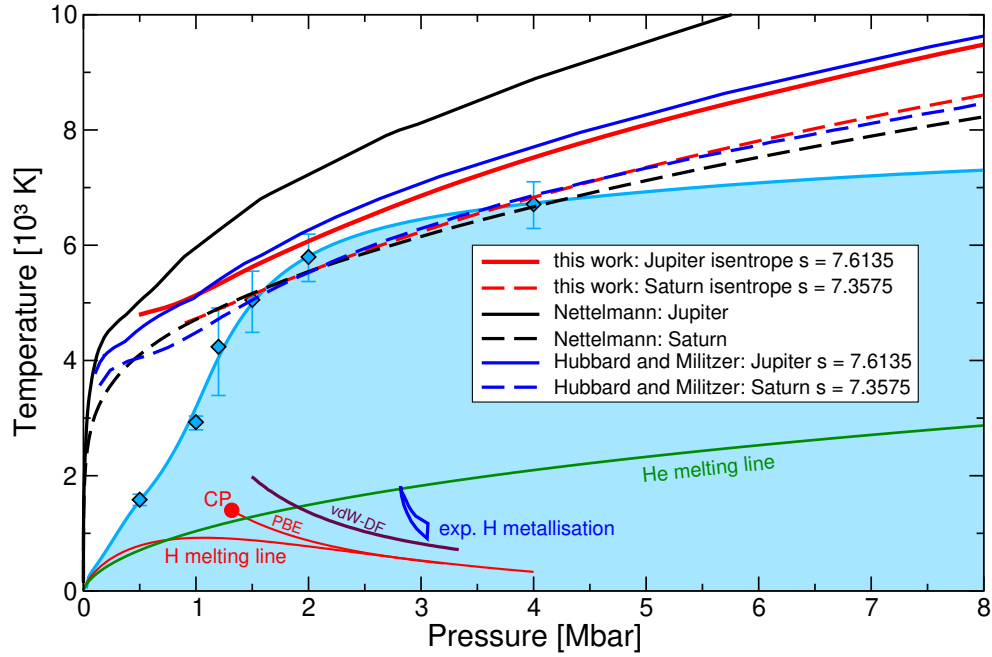


Figure 7.2.2: Isentropes of Jupiter and Saturn in comparison to the miscibility diagram. Diamonds and coloured area are the same as in Fig. 6.3.1. Planetary isentropes are from Nettelmann *et al.* [115, 140], Hubbard and Militzer [114], and vdW-DF calculations from this work. Entropies are given in k_B/atom .

fraction, DFT-MD simulations with the vdW-DF using 256 electrons (18 He atoms and 220 H atoms) were performed similar to the calculations of Militzer [142]. EOS calculations for the miscibility diagram have been calculated using 64 electrons so that $x = 0.07563$ is not available in that data set. In turn, there is no entropy data for arbitrary p and T for that mixture. However, the entropy at 10 000 K has been calculated for 256 electrons and $x = 0.07563$ using CCI, see Fig. 4.3.1. This data has been used to obtain the corresponding pressure at 10 000 K for the required entropy value. These $p - T$ conditions have been used to compute isentropes via Eq. 7.1.8. Resulting profiles for Jupiter and Saturn are shown in Fig. 7.2.2 in comparison to the models of Nettelmann *et al.* [115, 140], Hubbard and Militzer [114], and the miscibility diagram at solar He abundance obtained in Sec. 6.3. Note that the vdW-DF isentropes have not been calculated for pressures lower than 0.5 Mbar because DFT-MD simulations become increasingly demanding for large volumes. In principle, one could use the SCvH EOS for lower pressures as done by Hubbard and Militzer, but a thermodynamically consistent connection between different EOS models is challenging [230] and out of the scope of this work. The available vdW-DF EOS data

are sufficient for a comparison with the demixing phase diagram. For Jupiter, the vdW-DF isentrope and the isentrope of Hubbard and Militzer *et al.* [114] show much lower temperatures than the isentrope of Nettelmann *et al.* [140]. The isentropes of Hubbard and Militzer and Nettelmann *et al.* are outside of the vdW-DF miscibility diagram, whereas the vdW-DF isentrope still intersects within the error bars. QMC calculations have shown that the vdW-DF overestimates the pressure to a larger extent than PBE [147] does. This indicates that the true isentrope could be located at slightly lower pressures than both DFT calculations predict and thus no demixing would occur in Jupiter. However, much more QMC calculations are needed to derive a more sophisticated conclusion. If demixing still occurs, it remains to be seen if planetary evolution models with helium rain are still able to reproduce the observed helium fraction in the atmosphere. The occurrence of hydrogen-helium immiscibility in Jupiter should therefore be critically discussed and the possibility of no helium rain at all should be taken into account. Other factors than demixing could influence the amount of He in the atmosphere. As mentioned in the previous section, a radiative zone that acts as barrier to convection could form, so that the combined effect of gravitational settling and thermal diffusion leads to a depletion of helium. The existence of such a zone at temperatures around 2 000 K depends on the presence of strong absorbers like potassium, sodium, and titanium oxide [266]. Interestingly, the atmospheric helium abundance in the Sun is similar to that of Jupiter and this He depletion compared to the protosolar value is actually caused by gravitational settling and thermal diffusion [55]. However, a strong argument in favour of He rain is the depletion of neon compared to the solar value, because it was found that Ne dissolves preferably in the non-metallic He rather than in the metallic hydrogen [64]. Alternatively, the neon depletion might be explained with a clathrate-hydrate formation scenario where neon is not easily trapped in these ice cages [275] and therefore not present in a solar abundance.

For the shown Saturn isentropes, differences between the models are not as pronounced as for Jupiter. The isentropes of Hubbard and Militzer [114], and the presented one based on vdW-DF calculations agree well with each other. For high pressures, the vdW-DF isentrope shows slightly higher temperatures than the isentrope of Hubbard and Militzer. Both isentropes show slightly higher temperatures than the isentrope of Nettelmann *et al.* [140]. Still, all isentropes intersect with the miscibility diagram. In Fig. 7.2.3, evolution calculations for Saturn performed by Püstow *et al.* [61] are reprinted to discuss consequences of the presented miscibility diagram for Saturn. Püstow *et al.* used the Lorenzen *et al.* [65, 134] miscibility diagram to calculate Saturn's inhomogeneous evolution. Inhomogeneous evolution

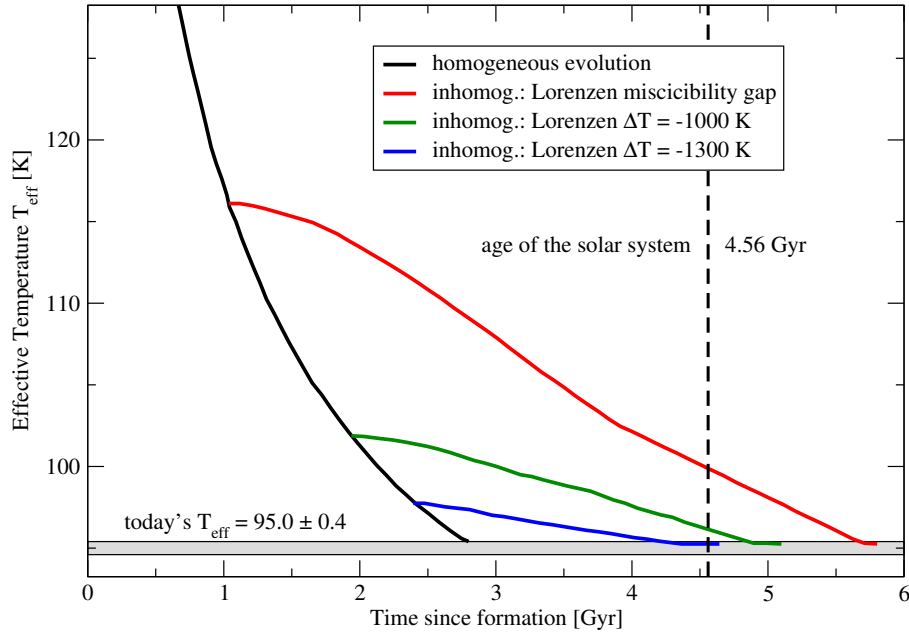


Figure 7.2.3: Effective temperature of Saturn as a function of time since its formation. Today's effective temperature is shown as grey area. All data has been calculated by Püstow *et al.* [61] based on the Lorenzen *et al.* data [65, 134]. The Lorenzen *et al.* demixing temperatures were shifted by Püstow *et al.* by ΔT to mimic the Morales *et al.* [136] phase diagram.

means that the composition of a given layer in the planetary model is allowed to change during its evolution. Thus, helium is allowed to sink down according to the underlying miscibility diagram. Saturn's age is overestimated when the original Lorenzen *et al.* data is considered. Püstow *et al.* lowered the demixing temperatures by ΔT in order to mimic the Morales *et al.* [136] data because these are only available for a single H-He mixture. A decrease in demixing temperature results in a lowering of Saturn's age and a shift of $\Delta T = -1300$ K reproduces the age of the solar system. It has been shown in Fig. 6.1.1, 6.2.1, and 6.3.1 that the miscibility diagram changes significantly when the vdW density functional and the non-ideal entropy of mixing is used. The demixing temperatures for the solar mixture decrease by about 2000 K compared to the Lorenzen *et al.* data. The calculations by Püstow *et al.* suggest that such a decrease would lower Saturn's age to a value below the age of the solar system, because demixing in Saturn would start at a later stage in its evolution. Furthermore, demixing would occur in a smaller part of its volume and at deeper levels. However, the artificial lowering of the Lorenzen *et al.* data does not include the changes introduced by the non-ideal entropy to the complete miscibility

diagram. This effect has been shown in Fig. 6.2.1 and significantly increases the He fraction of the He-rich phase. In turn, more He would sink towards the planetary core and a greater amount of energy would be converted to heat. As a consequence, the inhomogeneous evolution would possibly lead to a slower decrease of the effective temperature with time, effectively prolonging Saturn's cooling curve. If more He sinks towards the core, compositional gradients would be increased. Leconte and Chabrier [63] pointed out that these gradients could lead to layered convection, which reduces the cooling rate of Saturn significantly and offers an alternative or additional mechanism to explain its excess luminosity.

The calculations in this chapter are only the starting point for new and improved planetary models which have to be produced in future calculations. Especially the recalculation of Saturn's evolution is of great interest to see the quantitative impact of the new miscibility gap on Saturn's excess luminosity and its predicted age.

Chapter 8

Conclusion

8.1 Summary

In this thesis, density functional theory calculations coupled to classical molecular dynamics simulations have been performed for hydrogen-helium mixtures. The equation of state has been calculated for 29 He fractions, 15 temperatures from 1 000 K to 15 000 K and pressures between 0.5 Mbar and 30 Mbar were considered in particular for each He fraction. More than 7 500 EOS calculations have been performed for that purpose. The vdW-DF of Dion *et al.* [100] has been selected as an appropriate exchange-correlation functional based on the comparison to experimental and theoretical data. Especially the shift of the hydrogen metallisation pressure towards the experiments of Knudson *et al.* [83] and the agreement of the enthalpy with QMC data [147] are strong indications that the vdW-DF is superior to PBE for the purpose of calculating a more accurate miscibility diagram. In Ch. 4, it has been shown, that the ideal entropy of mixing is insufficient to approximate the entropy. Different approaches have been tested to obtain the non-ideal entropy of mixing. The coupling-constant integration method has been proven to yield most accurate non-ideal entropies. These have subsequently been used to obtain the entropy for arbitrary pressures and temperatures using a thermodynamic integration technique via the equation of state. It has been shown that this technique yields the same results as coupling-constant integration. The EOS data and entropies were used to obtain the Gibbs free energy of mixing. It has been shown that nuclear quantum corrections affect the Gibbs free energy of mixing mostly at low temperatures and that their inclusion increases the miscibility gap by a small amount. The Gibbs free energy of mixing was subsequently used to calculate the complete miscibility gap of hydrogen-helium mixtures for pressures up to 30 Mbar. It was shown

that the vdW-DF and the non-ideal entropy both have a significant impact on the demixing phase diagram compared to calculations by Lorenzen *et al.* [65, 134] and Morales *et al.* [136]. The main influence of the vdW-DF is a shift of demixing pressures to higher values by about 0.5 Mbar. The inclusion of the non-ideal entropy has been shown to alter the miscibility diagram completely at low pressures. Calculations using the ideal entropy of mixing show demixing islands, see Fig. 1.3.2, 6.1.1, and 6.2.1, which are separated from the proposed liquidus line. It has been confirmed, that the non-ideal entropy changes this behaviour by extending the miscibility to much lower pressures. Additionally, the demixing temperatures are lowered significantly compared to calculations using the ideal entropy of mixing. In Ch. 7, it has been shown that demixing temperatures are decreased to such an extent, that the present-day Jupiter model of Hubbard and Militzer [114] does not intersect with the vdW-DF miscibility diagram. As a consequence, helium has possibly not been separated from hydrogen in Jupiter due to demixing and the observed He depletion in the atmosphere needs an alternative explanation. However, a Jupiter $p - T$ profile based on the calculated vdW-DF EOS data has been computed and it has been shown in Fig. 7.2.2 that this isentrope still intersects with the error bars of the vdW-DF miscibility diagram. Therefore, it is not clear, whether He rain still occurs in Jupiter. Due to the proximity of the Jupiter models to the miscibility diagram, Jupiter could be in a state where demixing has just begun or is about to begin. For Saturn, the situation is clear because all isentropes intersect with the miscibility diagram. However, the layer of He rain is shifted to higher pressures, i.e. deeper into the planet. Thus, demixing would begin at a later time in Saturn's evolution compared to calculations based on PBE data. This eventually impacts the calculation of Saturn's cooling time and would lead to a younger age than determined by previous calculations [61] that made use of the PBE demixing phase diagram of Lorenzen *et al.* [65, 134].

8.2 Outlook

The quality of density functional theory calculations depends crucially on the treatment of exchange and correlation effects by the chosen XC-functional. High precision experiments are needed to verify these approximations. For hydrogen, it has been outlined in Sec. 1.2, that no available XC-functional is able to reproduce Hugoniot data within the error bars [146]. Additionally, contradicting experiments exist regarding the metallisation transition in liquid hydrogen. This further complicates the choice of an appropriate XC-functional. Hence, it needs to be clarified, why different

experiments yield contradicting results. Only then, theoretical calculations can be benchmarked. Up to now, the most precise dynamic compression experiment on the metallisation of deuterium has been done by Knudson *et al.* [83] at Sandia National Labs using magnetically driven flyer plates [276]. The reproduction of the results of this experiment on other platforms, e.g. at the National Ignition Facility using Laser-driven shocks [277], is a necessary and mandatory step. In turn, these experiments will allow a better evaluation of theoretical approaches like DFT or QMC. Depending on the results of future experiments, it could be necessary to revise the H-He miscibility diagram using a different approximation for the XC-functional. For the demixing phase diagram of H-He mixtures, no published experimental results exist at pressures and temperatures relevant for Jupiter and Saturn. To validate the obtained miscibility gap, such experiments are needed and will hopefully be performed in the near future.

The miscibility diagram could also be revalidated using other theoretical methods. It has been shown by Lorenzen *et al.* [65] and Soubiran *et al.* [127] that demixing can be determined by direct visualisation of the simulation box if the particle numbers are sufficiently high. This can be used to obtain the miscibility gap by direct simulations. However, a number of difficulties are associated with that technique. Foremost, it is completely unclear how finite-size effects affect the demixing. It has to be checked that convergence with respect to particle number can be achieved and that this particle number is still feasible within standard DFT codes such as VASP. Alternatively, it might be possible to derive effective potentials from the DFT-MD simulations of H-He mixtures using a force-matching algorithm [278, 279]. These potentials could then be used in classical MD simulations with millions of atoms. Furthermore, they could be used in a Gibbs ensemble Monte Carlo simulation [144] similar to the work of Schouten *et al.* [123].

In Ch. 6, it has been shown, that the chosen temperature grid (1000 K) might be too large to obtain accurate critical temperatures. Thus, it would be possible to obtain a denser temperature grid using more computational resources, which would decrease the error of the critical temperatures.

In future work, new consistent models of Saturn and Jupiter have to be calculated based on the obtained miscibility diagram. Especially the cooling history of Saturn will be influenced and new information on its luminosity anomaly will be gathered. In general, the obtained vdW-DF EOS and entropy data could be used. However, the usage of that functional has been motivated by its ability to reproduce QMC calculations of the enthalpy [147]. Yet, it has also been shown, that the vdW-DF, compared to QMC, overestimates the pressure more than PBE does. Thus, the vdW-

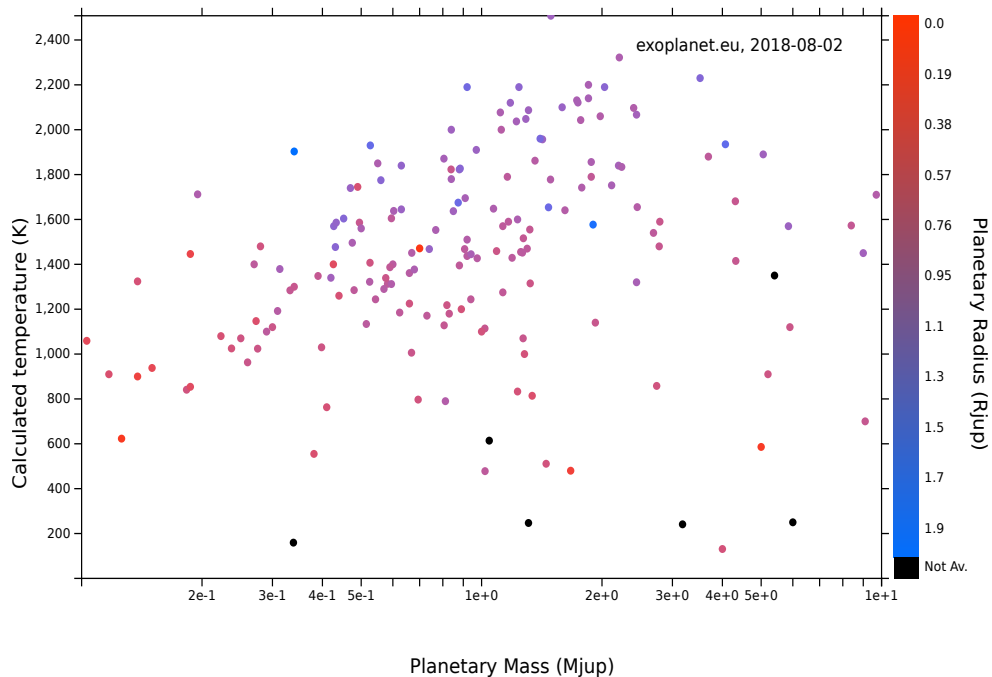


Figure 8.2.1: Calculated equilibrium temperature of 176 out of 4017 confirmed exoplanets as a function of their mass in units of Jupiter masses. The planetary radius in Jupiter radii is colour-coded. Figure obtained from exoplanet.org on August, 2nd 2018.

DF might not be suitable for planetary models and a more appropriate functional has to be identified. There is already a huge amount of EOS calculations that use PBE in the highly correlated regime. Wide-range equations of state for pure H and He have been calculated by Becker *et al.* [230]. These data lack information about the entropy and therefore free energy. The methods from Sec. 2.6 applied in Ch. 4 could be used to calculate the missing data which would facilitate the calculation of planetary models. Still, only linear mixtures using the ideal entropy of mixing could be constructed for arbitrary He fractions. To obtain information about the real mixture, simulations as done by Militzer [142] for a H-He mixture with $x = 0.07563$ should be performed also for different He fractions. For Saturn, He-rich mixtures would be favourable because He would be present in higher amounts deep in Saturn because of He rain. These calculations are subject to future work.

The calculations in this work are also relevant for exoplanets that are Jupiter- or Saturn-like. In Fig. 8.2.1, the calculated equilibrium temperatures of 176 exoplanets with masses between $0.1 M_J$ and $10 M_J$ are shown. The data might be biased towards hotter exoplanets because the detection of planets by their transit in front of

their host star favours smaller semi-major axes [280]. Nevertheless, a few exoplanets with equilibrium temperatures around 200 K are known. Hydrogen-helium demixing could occur on these planets, if their compositions are close to Jupiter and Saturn. In the future, more exoplanets will be discovered by new missions such as TESS [13] or PLATO [14]. Additionally, it is absolutely necessary that a Saturn entry probe is planned that measures the composition of Saturn similarly to the Galileo entry probe for Jupiter. The uncertainties of the remote observations by the Voyager and Cassini missions are too large to calculate the precise He abundance. Furthermore, information on the neon and argon abundance would be beneficial since these elements have been argued to be a tracer of H-He demixing.

Other interesting questions concerning the miscibility of H and He are: how do helium-rich droplets form in the interior of giant planets? How large are these droplets and what are the time scales on which they sink towards the core? Do they dissolve again before they reach the core? The formation of droplets is in general described by nucleation theory [281, 282] and first estimates to these questions have been given by Püstow [283] under strongly simplifying assumptions. However, more accurate descriptions of these processes are needed in order to understand the physics of planetary interiors and evolution models.

Appendix A

Derivations

A.1 Thermodynamic integration formula for p, T

The derivation of Eq. (2.6.2) is straightforward and similar to the derivation of Eq. (2.6.1), which is available in Ref. [262].

Starting from the definition of the Gibbs free energy, Eq. (2.5.2), the entropy can be written as

$$S(p, T) = \frac{U(p, T)}{T} + \frac{p}{T}V(p, T) - \frac{G(p, T)}{T}. \quad (\text{A.1.1})$$

We use the fact that the difference of $\frac{G(p, T)}{T}$ to a reference state $\frac{G(p_0, T_0)}{T_0}$ can be written as a line integral

$$\frac{G(p, T)}{T} - \frac{G(p_0, T_0)}{T_0} = \int_{p_0, T_0}^{p, T} d\frac{G(p, T)}{T}, \quad (\text{A.1.2})$$

and insert this into Eq. (A.1.1), which yields

$$S(p, T) = \frac{U(p, T)}{T} + \frac{p}{T}V(p, T) - \int_{p_0, T_0}^{p, T} d\frac{G(p, T)}{T} + c, \quad (\text{A.1.3})$$

where $c = -\frac{G(p_0, T_0)}{T_0}$. Using a suitable map [262], the line integral can be split into paths of constant pressure and paths of constant temperature, where

$$\int_{p_0, T_0}^{p, T} d\frac{G(p, T)}{T} = \int_{p_0}^p \frac{\partial}{\partial p'} \left(\frac{G(p', T_0)}{T_0} \right)_T dp' + \int_{T_0}^T \frac{\partial}{\partial T'} \left(\frac{G(p, T')}{T'} \right)_p dT'. \quad (\text{A.1.4})$$

The derivatives of $\frac{G(p,T)}{T}$ w.r.t. pressure and temperature can be evaluated when using the fundamental thermodynamic relation $dG = -SdT + Vdp$ as follows:

$$\frac{\partial}{\partial p} \left(\frac{G(p,T)}{T} \right)_T = \frac{V(p,T)}{T}, \quad (\text{A.1.5})$$

$$\frac{\partial}{\partial T} \left(\frac{G(p,T)}{T} \right)_p = -\frac{G(p,T)}{T^2} + \frac{1}{T} \frac{\partial G(p,T)}{\partial T} = -\frac{U(p,T) + pV(p,T)}{T^2} \quad (\text{A.1.6})$$

Inserting these equations into Eq. (A.1.3) one arrives at

$$S(p,T) = \frac{U(p,T) + pV(p,T)}{T} - \int_{p_0}^p dp' \frac{V(p', T_0)}{T_0} + \int_{T_0}^T dT' \frac{U(p, T') + pV(p, T')}{T'^2} + c, \quad (\text{A.1.7})$$

which is Eq. (2.6.2).

A.2 Reduced coupling-constant integration

The series expansion centered around λ_0 of Eq. (2.6.22) can be generally expressed as

$$\Delta F = \int_0^1 d\lambda \sum_{n=0}^{\infty} \frac{1}{n!} \left(\frac{\partial^{n+1} F(\lambda)}{\partial \lambda^{n+1}} \right)_{\lambda_0} (\lambda - \lambda_0)^n. \quad (\text{A.2.1})$$

The derivatives of $F(\lambda)$ w.r.t. λ have to be calculated similar to Eq. (2.6.28), using the definitions of $Q(\lambda)$ and the ensemble average. The first derivative has already been derived in Eq. (2.6.28), where

$$\frac{\partial F(\lambda)}{\partial \lambda} = \left\langle \frac{\partial V(\lambda)}{\partial \lambda} \right\rangle_{\lambda}. \quad (\text{A.2.2})$$

The second derivative is

$$\frac{\partial^2 F(\lambda)}{\partial \lambda^2} = \frac{\partial}{\partial \lambda} \left\langle \frac{\partial V(\lambda)}{\partial \lambda} \right\rangle_{\lambda}, \quad (\text{A.2.3})$$

$$= \frac{\partial}{\partial \lambda} \frac{1}{Q(\lambda)} \int \frac{d\mathbf{r} d\mathbf{p}}{h^{3N} N!} \left(\frac{\partial V(\lambda)}{\partial \lambda} \right) e^{-\beta H(\lambda)}, \quad (\text{A.2.4})$$

$$= \beta \left\langle \frac{\partial V(\lambda)}{\partial \lambda} \right\rangle \left\langle \frac{\partial V(\lambda)}{\partial \lambda} \right\rangle + \left\langle \frac{\partial^2 V(\lambda)}{\partial \lambda^2} \right\rangle - \beta \left\langle \left(\frac{\partial V(\lambda)}{\partial \lambda} \right)^2 \right\rangle \quad (\text{A.2.5})$$

$$= -\beta \{ \langle (V_1 - V_0)^2 \rangle - \langle V_1 - V_0 \rangle^2 \}, \quad (\text{A.2.6})$$

where the second term in Eq. (A.2.5) is zero because a linear combination of the Hamiltonians in Eq. (2.6.18) has been used. Deriving higher order terms is cumbersome. The following quantity is introduced to facilitate the notation:

$$C_n^m = \left\langle \left(\frac{\partial V(\lambda)}{\partial \lambda} \right)^n \right\rangle_\lambda^m = \langle (V_1 - V_0)^n \rangle_\lambda^m. \quad (\text{A.2.7})$$

Higher order derivatives of $F(\lambda)$ w.r.t. λ can be expressed as derivatives of C_n^1 , which themselves can be expressed through C_n^m :

$$\frac{\partial C_1^1}{\partial \lambda} = \beta(C_1^2 - C_2^1), \quad (\text{A.2.8})$$

$$\frac{\partial C_2^1}{\partial \lambda} = \beta(C_1^1 C_2^1 - C_3^1), \quad (\text{A.2.9})$$

$$\frac{\partial C_3^1}{\partial \lambda} = \beta(C_1^1 C_3^1 - C_4^1). \quad (\text{A.2.10})$$

Expressing Eq. (A.2.6) using these quantities results in

$$\frac{\partial^2 F(\lambda)}{\partial \lambda^2} = \frac{\partial}{\partial \lambda} C_1^1 = \beta(C_1^2 - C_2^1). \quad (\text{A.2.11})$$

The third and fourth derivatives are

$$\frac{\partial^3 F}{\partial \lambda^3} = \beta^2 (-3C_1^1 C_2^1 + C_3^1 + 2C_1^3), \quad (\text{A.2.12})$$

and

$$\frac{\partial^4 F}{\partial \lambda^4} = \beta^3 (-12C_1^2 C_2^1 + 3C_2^2 + 4C_1^1 C_3^1 + 6C_1^4 - C_4^1), \quad (\text{A.2.13})$$

respectively. These expressions have been used to obtain the Taylor series up to third order in λ (which requires the fourth derivative). However, no systematic convergence could be obtained for the quadratic and cubic term. This might be due to the fact that higher order moments of $\langle V_1 - V_0 \rangle$ require much better statistics and thus much longer simulations to converge. The convergence of the higher moments has not been systematically checked because simulations using the standard CCI approach have been used during this thesis anyway. Still, this open question will be addressed in future work.

Bibliography

- [1] Alpher R.A., Bethe H., and Gamow G. *The Origin of Chemical Elements*. [Phys. Rev.](#) **73**, 803 (1948).
- [2] Bethe H.A. *Energy production in stars*. [Phys. Rev.](#) **55**, 0103 (1939).
- [3] Burrows A. and Liebert J. *The science of brown dwarfs*. [Rev. Mod. Phys.](#) **65**, 301 (1993).
- [4] Baraffe I., Chabrier G., Allard F., and Hauschildt P.H. *New Evolutionary Tracks for Very Low Mass Stars*. [Astrophys. J.](#) **446**, L35 (1995).
- [5] Kulkarni S.R. *Brown Dwarfs: A Possible Missing Link Between Stars and Planets*. [Science](#) **276**, 1350 (1997).
- [6] *Calar Alto Observatory*. <http://www.caha.es>. Accessed: 8th of August 2018.
- [7] *Subaru Telescope*. <https://subarutelescope.org>. Accessed: 8th of August 2018.
- [8] *Extremely Large Telescope*. <https://www.eso.org/public/teles-instr/elt/>. Formerly known as European Extremely Large Telescope (E-ELT), accessed: 8th of August 2018.
- [9] Pollacco D.L., Skillen I., Cameron A.C., Christian D.J., Hellier C., Irwin J., Lister T.A., Street R.A., West R.G., Anderson D., Clarkson W.I., Deeg H., Enoch B., Evans A., Fitzsimmons A., Haswell C.A., Hodgkin S., Horne K., Kane S.R., Keenan F.P., Maxted P.F.L., Norton A.J., Osborne J., Parley N.R., Ryans R.S.I., Smalley B., Wheatley P.J., and Wilson D.M. *The WASP Project and the SuperWASP Cameras*. [Publ. Astron. Soc. Pac.](#) **118**, 1407 (2006).
- [10] Neuhauser R., Errmann R., Berndt A., Maciejewski G., Takahashi H., Chen W.P., Dimitrov D.P., Pribulla T., Nikogossian E.H., Jensen E.L.N., Marschall L., Wu Z.Y., Kellerer A., Walter F.M., Briceño C., Chini R., Fernandez M.,

- Raetz S., Torres G., Latham D.W., Quinn S.N., Niedzielski A., Bukowiecki Ł., Nowak G., Tomov T., Tachihara K., Hu S.C.L., Hung L.W., Kjurkchieva D.P., Radeva V.S., Mihov B.M., Slavcheva-Mihova L., Bozhinova I.N., Budaj J., Vaňko M., Kundra E., Hambálek Ł., Krushevskaya V., Movsessian T., Harutyunyan H., Downes J.J., Hernandez J., Hoffmeister V.H., Cohen D.H., Abel I., Ahmad R., Chapman S., Eckert S., Goodman J., Guerard A., Kim H.M., Koontharana A., Sokol J., Trinh J., Wang Y., Zhou X., Redmer R., Kramm U., Nettelmann N., Mugrauer M., Schmidt J., Moualla M., Ginski C., Marka C., Adam C., Seeliger M., Baar S., Roell T., Schmidt T.O.B., Treppl L., Eisenbeiß T., Fiedler S., Tetzlaff N., Schmidt E., Hohle M.M., Kitze M., Chakrova N., Gräfe C., Schreyer K., Hambaryan V.V., Broeg C.H., Koppenhoefer J., and Pandey A.K. *The Young Exoplanet Transit Initiative (YETI)*. *Astron. Nachr.* **332**, 547 (2011).
- [11] Bahcall N.A. *The Hubble Space Telescope*. *Ann. N.Y. Acad. Sci.* **470**, 331 (1986).
- [12] Borucki W.J., Koch D., Basri G., Batalha N., Brown T., Caldwell D., Caldwell J., Christensen-Dalsgaard J., Cochran W.D., DeVore E., Dunham E.W., Dupree A.K., Gautier T.N.I., Geary J.C., Gilliland R., Gould A., Howell S.B., Jenkins J.M., Kondo Y., Latham D.W., Marcy G.W., Meibom S., Kjeldsen H., Lissauer J.J., Monet D.G., Morrison D., Sasselov D., Tarter J., Boss A., Brownlee D., Owen T., Buzasi D., Charbonneau D., Doyle L., Fortney J., Ford E.B., Holman M.J., Seager S., Steffen J.H., Welsh W.F., Rowe J., Anderson H., Buchhave L., Ciardi D., Walkowicz L., Sherry W., Horch E., Isaacson H., Everett M.E., Fischer D., Torres G., Johnson J.A., Endl M., MacQueen P., Bryson S.T., Dotson J., Haas M., Kolodziejczak J., Van Cleve J., Chandrasekaran H., Twicken J.D., Quintana E.V., Clarke B.D., Allen C., Li J., Wu H., Tenenbaum P., Verner E., Bruhweiler F., Barnes J., and Prsa A. *Kepler Planet-Detection Mission: Introduction and First Results*. *Science* **327**, 977 (2010).
- [13] *Transiting Exoplanet Survey Satellite (TESS) website*. <https://tess.gsfc.nasa.gov>. Accessed: 2nd of August 2018.
- [14] *PLANetary Transits and Oscillations of stars (PLATO) website*. <http://sci.esa.int/plato/>. Accessed: 2nd of August 2018.
- [15] Nettelmann N., Holst B., Kietzmann A., French M., Redmer R., and Blaschke

- D. *Ab Initio Equation of State Data for Hydrogen, Helium, and Water and the Internal Structure of Jupiter*. [Astrophys. J.](#) **683**, 1217 (2008).
- [16] French M., Mattsson T.R., Nettelmann N., and Redmer R. *Equation of state and phase diagram of water at ultrahigh pressures as in planetary interiors*. [Phys. Rev. B](#) **79**, 513 (2009).
- [17] French M., Becker A., Lorenzen W., Nettelmann N., Bethkenhagen M., Wicht J., and Redmer R. *Ab Initio Simulations for Material Properties along the Jupiter Adiabats*. [Astrophys. J. Suppl. Ser.](#) **202**, 5 (2012).
- [18] Bethkenhagen M., French M., and Redmer R. *Equation of state and phase diagram of ammonia at high pressures from ab initio simulations*. [J. Chem. Phys.](#) **138**, 234504 (2013).
- [19] Bethkenhagen M., Cebulla D., Redmer R., and Hamel S. *Superionic Phases of the 1:1 Water–Ammonia Mixture*. [J. Phys. Chem.](#) **119**, 10582 (2015).
- [20] Bethkenhagen M., Meyer E.R., Hamel S., Nettelmann N., French M., Scheibe L., Ticknor C., Collins L.A., Kress J.D., Fortney J.J., and Redmer R. *Planetary Ices and the Linear Mixing Approximation*. [Astrophys. J.](#) **848** (2017).
- [21] Irwin P.G.J., Toledo D., Garland R., Teanby N.A., Fletcher L.N., Orton G.A., and Bézard B. *Detection of hydrogen sulfide above the clouds in Uranus’s atmosphere*. [Nature Astron.](#) **2**, 420 (2018).
- [22] Hubbard W.B., Nellis W.J., Mitchell A.C., Holmes N.C., Limaye S.S., and McCandless P.C. *Interior Structure of Neptune - Comparison with Uranus*. [Science](#) **253**, 648 (1991).
- [23] Dong X., Oganov A.R., Goncharov A.F., Stavrou E., Lobanov S., Saleh G., Qian G.R., Zhu Q., Gatti C., Deringer V.L., Dronskowski R., Zhou X.F., Prakapenka V.B., Konôpkova Z., Popov I.A., Boldyrev A.I., and Wang H.T. *A stable compound of helium and sodium at high pressure*. [Nature Chem.](#) **9**, 440 (2017).
- [24] Hall C.F. *Pioneer 10*. [Science](#) **183**, 301 (1974).
- [25] Abelson P.H. *Pioneer 10 Mission to Jupiter*. [Science](#) **183**, 261 (1974).
- [26] Opp A.G. *Scientific Results from the Pioneer 11 Mission to Jupiter*. [Science](#) **188**, 447 (1975).

- [27] Lo D.J. *Voyager-1 - Moons of Jupiter*. [Technol. Rev.](#) **81**, 74 (1979).
- [28] Stone E.C. and Lane A.L. *Voyager-1 Encounter with the Jovian System*. [Science](#) **204**, 945 (1979).
- [29] Loudon J. *Voyager-2 - Jovian Moons Revisited*. [Technol. Rev.](#) **82**, 70 (1979).
- [30] Stone E.C. and Miner E.D. *Voyager-2 Encounter with the Saturnian System*. [Science](#) **215**, 499 (1982).
- [31] Johnson T.V., Yeates C.M., and Young R. *Space Science Reviews Volume on Galileo Mission Overview*. [Space Sci. Rev.](#) **60**, 3 (1992).
- [32] Bolton S.J. and the Juno Science Team. *The Juno Mission*. [Proc. Int. Astron. Union](#) **6**, 92 (2010).
- [33] Bolton S.J., Lunine J., Stevenson D., Connerney J.E.P., Levin S., Owen T.C., Bagenal F., Gautier D., Ingersoll A.P., Orton G.S., Guillot T., Hubbard W., Bloxham J., Coradini A., Stephens S.K., Mokashi P., Thorne R., and Thorpe R. *The Juno Mission*. [Space Sci. Rev.](#) **213**, 5 (2017).
- [34] Niemann H.B., Atreya S.K., Carignan G.R., Donahue T.M., Haberman J.A., Harpold D.N., Hartle R.E., Hunten D.M., Kasprzak W.T., Mahaffy P.R., Owen T.C., Spencer N.W., and Way S.H. *The Galileo probe mass spectrometer: Composition of Jupiter's atmosphere*. [Science](#) **272**, 846 (1996).
- [35] Zahn U., Hunten D.M., and Lehmacher G. *Helium in Jupiter's atmosphere: Results from the Galileo probe Helium Interferometer Experiment*. [J. Geophys. Res. Planets](#) **103**, 22815 (1998).
- [36] Bolton S.J. and Connerney J.E.P. *Editorial: Topical Collection of the Juno Mission Science Objectives, Instruments, and Implementation*. [Space Sci. Rev.](#) **213**, 1 (2017).
- [37] Helled R. and Lunine J. *Measuring Jupiter's water abundance by Juno: the link between interior and formation models*. [Mon. Not. R. Astron. Soc.](#) **441**, 2273 (2014).
- [38] Folkner W.M., Iess L., Anderson J.D., Asmar S.W., Buccino D.R., Durante D., Feldman M., Gomez Casajus L., Gregnanin M., Milani A., Parisi M., Park R.S., Serra D., Tommei G., Tortora P., Zannoni M., Bolton S.J., Connerney J.E.P., and Levin S.M. *Jupiter gravity field estimated from the first two Juno orbits*. [Geophys. Res. Lett.](#) **44**, 4694 (2017).

- [39] Wahl S.M., Hubbard W.B., Militzer B., Guillot T., Miguel Y., Movshovitz N., Kaspi Y., Helled R., Reese D., Galanti E., Levin S., Connerney J.E., and Bolton S.J. *Comparing Jupiter interior structure models to Juno gravity measurements and the role of a dilute core.* [Geophys. Res. Lett.](#) **44**, 4649 (2017).
- [40] Li C., Ingersoll A., Janssen M., Levin S., Bolton S., Adumitroaie V., Allison M., Arballo J., Bellotti A., Brown S., Ewald S., Jewell L., Misra S., Orton G., Oyafuso F., Steffes P., and Williamson R. *The distribution of ammonia on Jupiter from a preliminary inversion of Juno microwave radiometer data.* [Geophys. Res. Lett.](#) **44**, 5317 (2017).
- [41] Ingersoll A.P., Adumitroaie V., Allison M.D., Atreya S., Bellotti A.A., Bolton S.J., Brown S.T., Gulkis S., Janssen M.A., Levin S.M., Li C., Li L., Lunine J.I., Orton G.S., Oyafuso F.A., and Steffes P.G. *Implications of the ammonia distribution on Jupiter from 1 to 100 bars as measured by the Juno microwave radiometer.* [Geophys. Res. Lett.](#) **44**, 7676 (2017).
- [42] Kaspi Y., Galanti E., Hubbard W.B., Stevenson D.J., Bolton S.J., Iess L., Guillot T., Bloxham J., Connerney J.E.P., Cao H., Durante D., Folkner W.M., Helled R., Ingersoll A.P., Levin S.M., LUNINE J.I., Miguel Y., Militzer B., Parisi M., and Wahl S.M. *Jupiter’s atmospheric jet streams extend thousands of kilometres deep.* [Nature](#) **555**, 223 (2018).
- [43] Iess L., Folkner W.M., Durante D., Parisi M., Kaspi Y., Galanti E., Guillot T., Hubbard W.B., Stevenson D.J., Anderson J.D., Buccino D.R., Casajus L.G., Milani A., Park R., Racioppa P., Serra D., Tortora P., Zannoni M., Cao H., Helled R., LUNINE J.I., Miguel Y., Militzer B., Wahl S., Connerney J.E.P., Levin S.M., and Bolton S.J. *Measurement of Jupiter’s asymmetric gravity field.* [Nature](#) **555**, 220 (2018).
- [44] Bolton S.J., Adriani A., Adumitroaie V., Allison M., Anderson J., Atreya S., Bloxham J., Brown S., Connerney J.E.P., DeJong E., Folkner W., Gautier D., Grassi D., Gulkis S., Guillot T., Hansen C., Hubbard W.B., Iess L., Ingersoll A., Janssen M., Jorgensen J., Kaspi Y., Levin S.M., Li C., Lunine J., Miguel Y., Mura A., Orton G., Owen T., Ravine M., Smith E., Steffes P., Stone E., Stevenson D., Thorne R., Waite J., Durante D., Ebert R.W., Greathouse T.K., Hue V., Parisi M., Szalay J.R., and Wilson R. *Jupiter’s interior and deep atmosphere: The initial pole-to-pole passes with the Juno spacecraft.* [Science](#) **356**, 821 (2017).

- [45] Conrath B.J. and Gautier D. *Saturn Helium Abundance: A Reanalysis of Voyager Measurements*. [Icarus](#) **144**, 124 (2000).
- [46] Opp A.G. *Scientific Results from the Pioneer Saturn Encounter: Summary*. [Science](#) **207**, 401 (1980).
- [47] Waldrop M.M. *Voyager-1 at Saturn*. [Science](#) **210**, 1107 (1980).
- [48] Matson D.L., Spilker L.J., and Lebreton J.P. *The Cassini/Huygens Mission to the Saturnian System*. In *The Cassini-Huygens Mission*, pages 1–58. [Springer Netherlands, Dordrecht](#) (2003).
- [49] Mitchell R.T. *Cassini/Huygens at Saturn and Titan*. [Acta Astronaut.](#) **59**, 335 (2006).
- [50] Dougherty M.K., Esposito L.W., and Krimigis S.M., editors. *Saturn from Cassini-Huygens*. [Springer Netherlands, Dordrecht](#) (2009).
- [51] Lainey V., Jacobson R.A., Tajeddine R., Cooper N.J., Murray C., Robert V., Tobie G., Guillot T., Mathis S., Remus F., Desmars J., Arlot J.E., De Cuyper J.P., Dehant V., Pascu D., Thuillot W., Poncin-Lafitte C.L., and Zahn J.P. *New constraints on Saturn’s interior from Cassini astrometric data*. [Icarus](#) **281**, 286 (2017).
- [52] Kellermann, C., Becker, A., and Redmer, R. *Interior structure models and fluid Love numbers of exoplanets in the super-Earth regime*. [Astron. Astrophys.](#) **615**, A39 (2018).
- [53] Gautier D., Conrath B., Flasar M., Hanel R., Kunde V., Chedin A., and Scott N. *The Helium Abundance of Jupiter From Voyager*. [J. Geophys. Res. Space Phys.](#) **86**, 8713 (1981).
- [54] Conrath B.J., Gautier D., Hanel R.A., and Hornstein J.S. *The helium abundance of Saturn from Voyager measurements*. [Astrophys. J.](#) **282**, 807 (1984).
- [55] Bahcall J.N. and Pinsonneault M.H. *Helium Diffusion in the Sun*. [Astrophys. J.](#) **395**, L119 (1992).
- [56] Proffitt C.R. *Effects of heavy-element settling on solar neutrino fluxes and interior structure*. [Astrophys. J.](#) **425**, 849 (1994).
- [57] Koskinen T.T. and Guerlet S. *Atmospheric structure and helium abundance on Saturn from Cassini/UVIS and CIRS observations*. [Icarus](#) **307**, 161 (2018).

-
- [58] Stevenson D.J. *Thermodynamics and phase separation of dense fully ionized hydrogen-helium fluid mixtures*. [Phys. Rev. B](#) **12**, 3999 (1975).
- [59] Stevenson D.J. and Salpeter E.E. *The phase diagram and transport properties for hydrogen-helium fluid planets*. [Astrophys. J. Suppl. Ser.](#) **35**, 221 (1977).
- [60] Fortney J.J. *Looking into the giant planets*. [Science](#) **305**, 1414 (2004).
- [61] Püstow R., Nettelmann N., Lorenzen W., and Redmer R. *H/He demixing and the cooling behavior of Saturn*. [Icarus](#) **267**, 323 (2016).
- [62] Fortney J.J. and Hubbard W.B. *Phase separation in giant planets: inhomogeneous evolution of Saturn*. [Icarus](#) **164**, 228 (2003).
- [63] Leconte J. and Chabrier G. *Layered convection as the origin of Saturn's luminosity anomaly*. [Nat. Geosci.](#) **6**, 347 (2013).
- [64] Wilson H.F. and Militzer B. *Sequestration of Noble Gases in Giant Planet Interiors*. [Phys. Rev. Lett.](#) **104**, 121101 (2010).
- [65] Lorenzen W., Holst B., and Redmer R. *Metallization in hydrogen-helium mixtures*. [Phys. Rev. B](#) **84**, 235109 (2011).
- [66] Dalladay-Simpson P., Howie R.T., and Gregoryanz E. *Evidence for a new phase of dense hydrogen above 325 gigapascals*. [Nature](#) **529**, 63 (2016).
- [67] Dias R., Noked O., and Silvera I.F. *New low temperature phase in dense hydrogen: The phase diagram to 421 GPa*. arXiv:1603.02162v2 (2016).
- [68] Wigner E. and Huntington H.B. *On the possibility of a metallic modification of hydrogen*. [J. Chem. Phys.](#) **3**, 764 (1935).
- [69] Nellis W.J. *Wigner and Huntington: the long quest for metallic hydrogen*. [High Pressure Res.](#) **33**, 369 (2013).
- [70] Dubrovinsky L., Dubrovinskaia N., Prakapenka V.B., and Abakumov A.M. *Implementation of micro-ball nanodiamond anvils for high-pressure studies above 6[thinsp]Mbar*. [Nat. Commun.](#) **3**, 1163 (2012).
- [71] Dubrovinsky L., Dubrovinskaia N., Bykova E., Bykov M., Prakapenka V., Prescher C., Glazyrin K., Liermann H.P., Hanfland M., Ekholm M., Feng Q., Pourovskii L.V., Katsnelson M.I., Wills J.M., and Abrikosov I.A. *The most incompressible metal osmium at static pressures above 750 gigapascals*. [Nature](#) **525**, 226 (2015).

- [72] Dubrovinskaia N., Dubrovinsky L., Solopova N.A., Abakumov A., Turner S., Hanfland M., Bykova E., Bykov M., Prescher C., Prakapenka V.B., Petitgirard S., Chuvashova I., Gasharova B., Mathis Y.L., Ershov P., Snigireva I., and Snigirev A. *Terapascal static pressure generation with ultrahigh yield strength nanodiamond*. [Sci. Adv.](#) **2**, e1600341 (2016).
- [73] Dias R.P. and Silvera I.F. *Observation of the Wigner-Huntington transition to metallic hydrogen*. [Science](#) **355**, 715 (2017).
- [74] Goncharov A.F. and Struzhkin V.V. *Comment on "Observation of the Wigner-Huntington transition to metallic hydrogen"*. [Science](#) **357**, eaam9736 (2017).
- [75] Silvera I. and Dias R. *Response to Comment on "Observation of the Wigner-Huntington transition to metallic hydrogen"*. [Science](#) **357**, eaan1215 (2017).
- [76] Liu X.D., Dalladay-Simpson P., Howie R.T., Li B., and Gregoryanz E. *Comment on "Observation of the Wigner-Huntington transition to metallic hydrogen"*. [Science](#) **357**, eaan2286 (2017).
- [77] Silvera I.F. and Dias R. *Response to Comment on "Observation of the Wigner-Huntington transition to metallic hydrogen"*. [Science](#) **357**, eaan2671 (2017).
- [78] Dzyabura V., Zaghoo M., and Silvera I.F. *Evidence of a liquid-liquid phase transition in hot dense hydrogen*. [Proc. Natl. Acad. Sci. U.S.A.](#) **110**, 8040 (2013).
- [79] Ohta K., Ichimaru K., Einaga M., Kawaguchi S., Shimizu K., Matsuoka T., Hirao N., and Ohishi Y. *Phase boundary of hot dense fluid hydrogen*. [Sci. Rep.](#) **5**, 16560 (2015).
- [80] Zaghoo M., Salamat A., and Silvera I.F. *Evidence of a first-order phase transition to metallic hydrogen*. [Phys. Rev. B](#) **93**, 155128 (2016).
- [81] Weir S.T., Mitchell A.C., and Nellis W.J. *Metallization of Fluid Molecular Hydrogen at 140 GPa (1.4 Mbar)*. [Phys. Rev. Lett.](#) **76**, 1860 (1996).
- [82] Nellis W.J., Weir S.T., and Mitchell A.C. *Minimum metallic conductivity of fluid hydrogen at 140 GPa (1.4 Mbar)*. [Phys. Rev. B](#) **59**, 3434 (1999).
- [83] Knudson M.D., Desjarlais M.P., Becker A., Lemke R.W., Cochrane K.R., Savage M.E., Bliss D.E., Mattsson T.R., and Redmer R. *Direct observation of an abrupt insulator-to-metal transition in dense liquid deuterium*. [Science](#) **348**, 1455 (2015).

- [84] Lorenzen W., Holst B., and Redmer R. *First-order liquid-liquid phase transition in dense hydrogen*. [Phys. Rev. B](#) **82**, 195107 (2010).
- [85] Lorenzen W. *Phase Transitions in Hydrogen-Helium Mixtures*. Ph.D. thesis, Universität Rostock (2012).
- [86] Mazzola G., Helled R., and Sorella S. *Phase Diagram of Hydrogen and a Hydrogen-Helium Mixture at Planetary Conditions by Quantum Monte Carlo Simulations*. [Phys. Rev. Lett.](#) **120**, 025701 (2018).
- [87] Ebeling W. and Kremp D. *Theory of bound states and ionization equilibrium in plasmas and solids*. Ergebnisse der Plasmaphysik und der Gaselektronik. [Akademie-Verlag, Berlin](#) (1976).
- [88] Beule D., Ebeling W., Forster A., Juranek H., Redmer R., and Röpke G. *Hydrogen equation of state and plasma phase transition*. [Contrib. Plasma Phys.](#) **39**, 21 (1999).
- [89] Holst B., Nettelmann N., and Redmer R. *Equation of state for dense hydrogen and plasma phase transition*. [Contrib. Plasma Phys.](#) **47**, 368 (2007).
- [90] Koudriavtsev A., Jameson R., and Linert W. *The Law of Mass Action*. [Springer, Berlin, Heidelberg](#) (2011).
- [91] Heintz A. *Thermodynamik der Mischungen*. [Springer, Berlin, Heidelberg](#) (2017).
- [92] Ebeling W., Blaschke D., Redmer R., Reinholz H., and Röpke G. *The influence of Pauli blocking effects on the properties of dense hydrogen*. [J. Phys. A: Math. Theor.](#) **42**, 214033 (2009).
- [93] Redmer R. and Holst B. *Metal–Insulator Transition in Dense Hydrogen*. In R. Redmer, F. Hensel, and B. Holst, editors, *Metal-to-Nonmetal Transitions*, pages 63–84. [Springer, Berlin, Heidelberg](#) (2010).
- [94] Morales M.A., Pierleoni C., Schwegler E., and Ceperley D.M. *Evidence for a first-order liquid-liquid transition in high-pressure hydrogen from ab initio simulations*. [Proc. Natl. Acad. Sci. U.S.A.](#) **107**, 12799 (2010).
- [95] Morales M.A., Pierleoni C., and Ceperley D.M. *Equation of state of metallic hydrogen from coupled electron-ion Monte Carlo simulations*. [Phys. Rev. E](#) **81**, 021202 (2010).

- [96] Pierleoni C., Morales M.A., Rillo G., Holzmann M., and Ceperley D.M. *Liquid-liquid phase transition in hydrogen by coupled electron-ion Monte Carlo simulations*. [Proc. Natl. Acad. Sci. U.S.A.](#) **113**, 4953 (2016).
- [97] Perdew J.P., Burke K., and Ernzerhof M. *Generalized Gradient Approximation Made Simple*. [Phys. Rev. Lett.](#) **77**, 3865 (1996).
- [98] Heyd J., Scuseria G.E., and Ernzerhof M. *Hybrid functionals based on a screened Coulomb potential*. [J. Chem. Phys.](#) **118**, 8207 (2003).
- [99] Heyd J., Scuseria G.E., and Ernzerhof M. *Erratum: "Hybrid functionals based on a screened Coulomb potential" [J. Chem. Phys. 118, 8207 (2003)]*. [J. Chem. Phys.](#) **124**, 219906 (2006).
- [100] Dion M., Rydberg H., Schröder E., Langreth D.C., and Lundqvist B.I. *Van der Waals Density Functional for General Geometries*. [Phys. Rev. Lett.](#) **92**, 246401 (2004).
- [101] Lee K., Murray É.D., Kong L., Lundqvist B.I., and Langreth D.C. *Higher-accuracy van der Waals density functional*. [Phys. Rev. B](#) **82**, 081101 (2010).
- [102] Morales M.A., McMahon J.M., Pierleoni C., and Ceperley D.M. *Nuclear Quantum Effects and Nonlocal Exchange-Correlation Functionals Applied to Liquid Hydrogen at High Pressure*. [Phys. Rev. Lett.](#) **110**, 065702 (2013).
- [103] Dugdale J.S. and MacDonald D.K.C. *The Thermal Expansion of Solids*. [Phys. Rev.](#) **89**, 832 (1953).
- [104] Crawford R.K. and Daniels W.B. *Experimental Determination of the P-T Melting Curves of Kr, Ne, and He*. [J. Chem. Phys.](#) **55**, 5651 (1971).
- [105] Mills R.L., Liebenberg D.H., and Bronson J.C. *Equation of state and melting properties of ^4He from measurements to 20 kbar*. [Phys. Rev. B](#) **21**, 5137 (1980).
- [106] Loubeyre P., Besson J.M., Pinceaux J.P., and Hansen J.P. *High-Pressure Melting Curve of ^4He* . [Phys. Rev. Lett.](#) **49**, 1172 (1982).
- [107] Vos W.L., van Hinsberg M.G.E., and Schouten J.A. *High-pressure triple point in helium: The melting line of helium up to 240 kbar*. [Phys. Rev. B](#) **42**, 6106 (1990).

-
- [108] Datchi F., Loubeyre P., and Le Toullec R. *Extended and accurate determination of the melting curves of argon, helium, ice (H₂O), and hydrogen (H₂).* [Phys. Rev. B](#) **61**, 6535 (2000).
- [109] Santamaría-Pérez D., Mukherjee G.D., Schwager B., and Boehler R. *High-pressure melting curve of helium and neon: Deviations from corresponding states theory.* [Phys. Rev. B](#) **81**, 214101 (2010).
- [110] Belonoshko A.B., Koči L., and Rosengren A. *Stability of the bcc phase of ⁴He close to the melting curve: A molecular dynamics study.* [Phys. Rev. B](#) **85**, 012503 (2012).
- [111] Loubeyre P., LeToullec R., Pinceaux J.P., Mao H.K., Hu J., and Hemley R.J. *Equation of state and phase diagram of solid ⁴He from single-crystal x-ray diffraction over a large P-T domain.* [Phys. Rev. Lett.](#) **71**, 2272 (1993).
- [112] Zhang W., Li Z., Fu Z., Dai J., Chen Q., and Cai L. *Revisiting metallization boundary of warm dense helium in a wide ρ -T regime from ab initio study.* [Sci. Rep.](#) **7**, 41885 (2017).
- [113] Stixrude L. and Jeanloz R. *Fluid helium at conditions of giant planetary interiors.* [Proc. Natl. Acad. Sci. U.S.A.](#) **105**, 11071 (2008).
- [114] Hubbard W.B. and Militzer B. *A Preliminary Jupiter Model.* [Astrophys. J.](#) **820**, 80 (2016).
- [115] Nettelmann N., Püstow R., and Redmer R. *Saturn layered structure and homogeneous evolution models with different EOSs.* [Icarus](#) **225**, 548 (2013).
- [116] Preising M. and Redmer R. *The high pressure melting line of helium* (2018). Submitted.
- [117] Davis P., Döppner T., Rygg J.R., Fortmann C., Divol L., Pak A., Fletcher L., Becker A., Holst B., Sperling P., Redmer R., Desjarlais M.P., Celliers P., Collins G.W., Landen O.L., Falcone R.W., and Glenzer S.H. *X-ray scattering measurements of dissociation-induced metallization of dynamically compressed deuterium.* [Nature Commun.](#) **7**, 11189 (2016).
- [118] Stevenson D.J. *Metallic helium in massive planets.* [Proc. Nat. Acad. Sci. U.S.A.](#) **105**, 11035 (2008).

- [119] Preising M., Lorenzen W., Becker A., Redmer R., Knudson M.D., and Desjarlais M.P. *Equation of state and optical properties of warm dense helium*. [Phys. Plasmas](#) **25**, 012706 (2018).
- [120] Perdew J.P. *Density functional theory and the band gap problem*. [International Journal of Quantum Chemistry](#) **30**, 451 (1986).
- [121] Belonoshko, A. B. *Molecular-Dynamics of MgSiO₃ Perovskite at High-Pressures - Equation of State, Structure, and Melting Transition*. [Geochim. Cosmochim. Acta](#) **58**, 4039 (1994).
- [122] Loubeyre P., LeToullec R., and Pinceaux J.P. *A New Determination of the Binary Phase-Diagram of H₂-He Mixtures at 296-K*. [J. Phys.: Condens. Matter](#) **3**, 3183 (1991).
- [123] Schouten J. and Bergh L.V.D. *Density inversions between fluid and solid phases in the system He-H₂ at high pressures*. [Fluid Phase Equilib.](#) **32**, 1 (1986).
- [124] Bergh L.V.D., Schouten J., and Trappeniers N. *Fluid-fluid, fluid-solid and three-phase equilibria in the system helium-hydrogen at pressures up to 75 kbar*. [Physica A](#) **141**, 524 (1987).
- [125] Loubeyre P., Le Toullec R., and Pinceaux J.P. *Binary phase diagrams of H₂-He mixtures at high temperature and high pressure*. [Phys. Rev. B](#) **36**, 3723 (1987).
- [126] Lim J. and Yoo C.S. *Phase Diagram of Dense H₂-He Mixtures: Evidence for Strong Chemical Association, Miscibility, and Structural Change*. [Phys. Rev. Lett.](#) **120**, 165301 (2018).
- [127] Soubiran F., Mazevet S., Winisdoerffer C., and Chabrier G. *Optical signature of hydrogen-helium demixing at extreme density-temperature conditions*. [Phys. Rev. B](#) **87**, 165114 (2013).
- [128] Pfaffen-zeller O., Hohl D., and Ballone P. *Miscibility of Hydrogen and Helium under Astrophysical Conditions*. [Phys. Rev. Lett.](#) **74**, 2599 (1995).
- [129] Pollock E.L. and Alder B.J. *Phase Separation for a Dense Fluid Mixture of Nuclei*. [Phys. Rev. A](#) **15**, 1263 (1977).

-
- [130] Hansen J.P., Torrie G.M., and Vieillefosse P. *Statistical-Mechanics of Dense Ionized Matter .7. Equation of State and Phase Separation of Ionic Mixtures in a Uniform Background*. [Phys. Rev. A](#) **16**, 2153 (1977).
- [131] Hubbard W.B. and DeWitt H.E. *Statistical Mechanics of Light-Elements at High Pressure. VII. A Perturbative Free-Energy for Arbitrary Mixtures of H and He*. [Astrophys. J.](#) **290**, 388 (1985).
- [132] Klepeis J.E., Schafer K.J., Barbee T.W., and Ross M. *Hydrogen-Helium Mixtures at Megabar Pressures - Implications for Jupiter and Saturn*. [Science](#) **254**, 986 (1991).
- [133] Schouten J.A., de Kuijper A., and Michels J. *Critical line of He-H₂ up to 2500 K and the influence of attraction on fluid-fluid separation*. [Phys. Rev. B](#) **44**, 6630 (1991).
- [134] Lorenzen W., Holst B., and Redmer R. *Demixing of Hydrogen and Helium at Megabar Pressures*. [Phys. Rev. Lett.](#) **102**, 115701 (2009).
- [135] Morales M.A., Schwegler E., Ceperley D., Pierleoni C., Hamel S., and Caspersen K. *Phase separation in hydrogen-helium mixtures at Mbar pressures*. [Proc. Natl. Acad. Sci. U.S.A.](#) **106**, 1324 (2009).
- [136] Morales M.A., Hamel S., Caspersen K., and Schwegler E. *Hydrogen-helium demixing from first principles: From diamond anvil cells to planetary interiors*. [Phys. Rev. B](#) **87**, 174105 (2013).
- [137] Hohenberg P. and Kohn W. *Inhomogeneous Electron Gas*. [Phys. Rev.](#) **136**, B864 (1964).
- [138] Car R. and Parrinello M. *Unified Approach for Molecular Dynamics and Density-Functional Theory*. [Phys. Rev. Lett.](#) **55**, 2471 (1985).
- [139] Vorberger J., Tamblyn I., Militzer B., and Bonev S.A. *Hydrogen-helium mixtures in the interiors of giant planets*. [Phys. Rev. B](#) **75**, 024206 (2007).
- [140] Nettelmann N., Becker A., Holst B., and Redmer R. *Jupiter Models with Improved Ab Initio Hydrogen Equation of State (H-REOS.2)*. [Astrophys. J.](#) **750**, 52 (2012).
- [141] Militzer B. and Hubbard W.B. *Ab Initio Equation of State for Hydrogen-Helium Mixtures with Recalibration of the Giant-planet Mass-Radius Relation*. [Astrophys. J.](#) **774**, 148 (2013).

- [142] Militzer B. *Equation of state calculations of hydrogen-helium mixtures in solar and extrasolar giant planets*. [Phys. Rev. B](#) **87**, 014202 (2013).
- [143] Militzer B., Soubiran F., Wahl S.M., and Hubbard A. *Understanding Jupiter's interior*. [J. Geophys. Res. Planets](#) **121**, 1552 (2016).
- [144] Panagiotopoulos A.Z., Quirke N., Stapleton M., and Tildesley D.J. *Phase equilibria by simulation in the Gibbs ensemble*. [Mol. Phys.](#) **63**, 527 (1988).
- [145] Kohn W. and Sham L.J. *Self-Consistent Equations Including Exchange and Correlation Effects*. [Phys. Rev.](#) **140**, A1133 (1965).
- [146] Knudson M.D. and Desjarlais M.P. *High-Precision Shock Wave Measurements of Deuterium: Evaluation of Exchange-Correlation Functionals at the Molecular-to-Atomic Transition*. [Phys. Rev. Lett.](#) **118**, 035501 (2017).
- [147] Clay III R.C., Holzmann M., Ceperley D.M., and Morales M.A. *Benchmarking density functionals for hydrogen-helium mixtures with quantum Monte Carlo: Energetics, pressures, and forces*. [Phys. Rev. B](#) **93**, 035121 (2016).
- [148] Schöttler M. and Redmer R. *Ab Initio Calculation of the Miscibility Diagram for Hydrogen-Helium Mixtures*. [Phys. Rev. Lett.](#) **120**, 115703 (2018).
- [149] Schöttler M. and Redmer R. *Simulations of H-He mixtures using the van der Waals density functional*. [J. Plasma Phys.](#) **84**, 755840401 (2018).
- [150] Schöttler M., French M., Cebulla D., and Redmer R. *Free energy model for solid high-pressure phases of carbon*. [J. Phys.: Condens. Matter](#) **28**, 145401 (2016).
- [151] Le Bellac M. *Quantum Physics*. [Cambridge University Press, Cambridge](#) (2009).
- [152] Marx D. and Hutter J. *Ab initio Molecular Dynamics: Basic Theory And Advanced Methods*. [Cambridge University Press, Cambridge](#) (2009).
- [153] Born M. and Oppenheimer R. *Zur Quantentheorie der Molekeln*. [Ann. Phys.](#) **389**, 457 (1927).
- [154] Born M. and Huang K. *Dynamical theory of crystal lattices*. Oxford Classic Texts in the Physical Sciences. [The Clarendon Press, Oxford University Press, New York](#) (1998).

-
- [155] Szabo A. and Ostlund N. *Modern Quantum Chemistry: Introduction to Advanced Electronic Structure Theory*. [Dover Publications, Mineola, N.Y.](#) (1996).
- [156] Engel E. and Dreizler R.M. *Density Functional Theory - An Advanced Course*. [Springer, Berlin, Heidelberg](#) (2011).
- [157] Mermin N.D. *Thermal properties of the inhomogeneous electron gas*. [Phys. Rev.](#) **137**, A1441 (1965).
- [158] Collins L., Kwon I., Kress J., Troullier N., and Lynch D. *Quantum molecular dynamics simulations of hot, dense hydrogen*. [Phys. Rev. E](#) **52**, 6202 (1995).
- [159] Karasiev V.V., Sjostrom T., Dufty J., and Trickey S.B. *Accurate Homogeneous Electron Gas Exchange-Correlation Free Energy for Local Spin-Density Calculations*. [Phys. Rev. Lett.](#) **112**, 076403 (2014).
- [160] Sjostrom T. and Daligault J. *Gradient corrections to the exchange-correlation free energy*. [Phys. Rev. B](#) **90**, 155109 (2014).
- [161] Dornheim T., Groth S., Filinov A., and Bonitz M. *Permutation blocking path integral Monte Carlo: a highly efficient approach to the simulation of strongly degenerate non-ideal fermions*. [New J. Phys.](#) **17**, 073017 (2015).
- [162] Burke K., Smith J.C., Grabowski P.E., and Pribram-Jones A. *Exact conditions on the temperature dependence of density functionals*. [Phys. Rev. B](#) **93**, 195132 (2016).
- [163] Pribram-Jones A. and Burke K. *Connection formulas for thermal density functional theory*. [Phys. Rev. B](#) **93**, 205140 (2016).
- [164] Pribram-Jones A., Grabowski P.E., and Burke K. *Thermal Density Functional Theory: Time-Dependent Linear Response and Approximate Functionals from the Fluctuation-Dissipation Theorem*. [Phys. Rev. Lett.](#) **116**, 233001 (2016).
- [165] Groth S., Schoof T., Dornheim T., and Bonitz M. *Ab initio quantum Monte Carlo simulations of the uniform electron gas without fixed nodes*. [Phys. Rev. B](#) **93**, 085102 (2016).
- [166] Dornheim T., Groth S., Schoof T., Hann C., and Bonitz M. *Ab initio quantum Monte Carlo simulations of the uniform electron gas without fixed nodes: The unpolarized case*. [Phys. Rev. B](#) **93**, 205134 (2016).

- [167] Dornheim T., Groth S., Sjostrom T., Malone F.D., Foulkes W.M.C., and Bonitz M. *Ab Initio Quantum Monte Carlo Simulation of the Warm Dense Electron Gas in the Thermodynamic Limit*. [Phys. Rev. Lett.](#) **117**, 156403 (2016).
- [168] Dornheim T., Groth S., Vorberger J., and Bonitz M. *Permutation-blocking path-integral Monte Carlo approach to the static density response of the warm dense electron gas*. [Phys. Rev. E](#) **96**, 023203 (2017).
- [169] Groth S., Dornheim T., and Bonitz M. *Free energy of the uniform electron gas: Testing analytical models against first-principles results(dagger)*. [Contrib. Plasma Phys.](#) **57**, 137 (2017).
- [170] Smith J.C., Pribram-Jones A., and Burke K. *Exact thermal density functional theory for a model system: Correlation components and accuracy of the zero-temperature exchange-correlation approximation*. [Phys. Rev. B](#) **93**, 245131 (2016).
- [171] Slater J.C. *A Simplification of the Hartree-Fock Method*. [Phys. Rev.](#) **81**, 385 (1951).
- [172] Ceperley D.M. and ALDER B.J. *Ground State of the Electron Gas by a Stochastic Method*. [Phys. Rev. Lett.](#) **45**, 566 (1980).
- [173] Vosko S.H., Wilk L., and Nusair M. *Accurate spin-dependent electron liquid correlation energies for local spin density calculations: a critical analysis*. [Can. J. Phys.](#) **58**, 1200 (1980).
- [174] Ortiz G. and Ballone P. *Correlation energy, structure factor, radial distribution function, and momentum distribution of the spin-polarized uniform electron gas*. [Phys. Rev. B](#) **50**, 1391 (1994).
- [175] Gunnarsson O. and Lundqvist B.I. *Exchange and correlation in atoms, molecules, and solids by the spin-density-functional formalism*. [Phys. Rev. B](#) **13**, 4274 (1976).
- [176] Dobson J.F., Vignale G., and Das M.P. *Electronic Density Functional Theory*. [Springer US, Springer Science+Business Media New York](#), first edition (1998).
- [177] Gunnarsson O. and Lundqvist B.I. *Exchange and Correlation in Atoms, Molecules, and Solids by Spin-Density Functional Formalism*. [Phys. Rev. B](#) **13**, 4274 (1976).

- [178] Perdew J.P. *Accurate Density Functional for the Energy - Real-Space Cutoff of the Gradient Expansion for the Exchange Hole.* [Phys. Rev. Lett.](#) **55**, 1665 (1985).
- [179] Perdew J.P. and Yue W. *Accurate and Simple Density Functional for the Electronic Exchange Energy - Generalized Gradient Approximation.* [Phys. Rev. B](#) **33**, 8800 (1986).
- [180] Perdew J.P., Chevary J.A., Vosko S.H., Jackson K.A., Pederson M.R., Singh D.J., and Fiolhais C. *Atoms, Molecules, Solids, and Surfaces - Applications of the Generalized Gradient Approximation for Exchange and Correlation.* [Phys. Rev. B](#) **46**, 6671 (1992).
- [181] Armiento R. and Mattsson A.E. *Functional designed to include surface effects in self-consistent density functional theory.* [Phys. Rev. B](#) **72**, 085108 (2005).
- [182] Lee C.T., Yang W.T., and Parr R.G. *Development of the Colle-Salvetti Correlation-Energy Formula Into a Functional of the Electron-Density.* [Phys. Rev. B](#) **37**, 785 (1988).
- [183] Zhang Y.K. and Yang W.T. *Comment on "Generalized gradient approximation made simple".* [Phys. Rev. Lett.](#) **80**, 890 (1998).
- [184] Handy N.C. and Cohen A.J. *Left-right correlation energy.* [Mol. Phys.](#) **99**, 403 (2001).
- [185] Wu Z. and Cohen R.E. *More accurate generalized gradient approximation for solids.* [Phys. Rev. B](#) **73**, 235116 (2006).
- [186] Perdew J.P., Ernzerhof M., Zupan A., and Burke K. *Nonlocality of the density functional for exchange and correlation: Physical origins and chemical consequences.* [J. Chem. Phys.](#) **108**, 1522 (1998).
- [187] Tao J., Perdew J.P., Staroverov V.N., and Scuseria G.E. *Climbing the Density Functional Ladder: Nonempirical Meta-Generalized Gradient Approximation Designed for Molecules and Solids.* [Phys. Rev. Lett.](#) **91**, 146401 (2003).
- [188] Perdew J.P., Ruzsinszky A., Csonka G.I., and Constantin L.A. *Workhorse semilocal density functional for condensed matter physics and quantum chemistry.* [Phys. Rev. Lett.](#) **103**, 026403 (2009).

- [189] Sun J., Ruzsinszky A., and Perdew J.P. *Strongly Constrained and Appropriately Normed Semilocal Density Functional*. [Phys. Rev. Lett.](#) **115**, 036402 (2015).
- [190] Clementi E. and Chakravorty S.J. *A comparative study of density functional models to estimate molecular atomization energies*. [J. Chem. Phys.](#) **93**, 2591 (1990).
- [191] Becke A.D. *A new mixing of Hartree–Fock and local density-functional theories*. [J. Chem. Phys.](#) **98**, 1372 (1993).
- [192] Muscat J., Wander A., and Harrison N. *On the prediction of band gaps from hybrid functional theory*. [Chem. Phys. Lett.](#) **342**, 397 (2001).
- [193] Berland K., Cooper V.R., Lee K., Schroeder E., Thonhauser T., Hyldgaard P., and Lundqvist B.I. *van der Waals forces in density functional theory: a review of the vdW-DF method*. [Rep. Prog. Phys.](#) **78**, 066501 (2015).
- [194] Langreth D.C. and Perdew J.P. *The exchange-correlation energy of a metallic surface*. [Solid State Commun.](#) **17**, 1425 (1975).
- [195] Langreth D.C. and Perdew J.P. *Exchange-Correlation Energy of a Metallic Surface - Wave-Vector Analysis*. [Phys. Rev. B](#) **15**, 2884 (1977).
- [196] Rydberg H., Lundqvist B., Langreth D., and Dion M. *Tractable nonlocal correlation density functionals for flat surfaces and slabs*. [Phys. Rev. B](#) **62**, 6997 (2000).
- [197] Rydberg M. *Non local correlations in density functional theory*. Ph.D. thesis, Chalmers University of Technology and Göteborg University (2001).
- [198] Rydberg H., Dion M., Jacobson N., Schröder E., Hyldgaard P., Simak S., Langreth D., and Lundqvist B. *Van der Waals Density Functional for Layered Structures*. [Phys. Rev. Lett.](#) **91**, 126402 (2003).
- [199] Dion M. *van der Waals forces in density functional theory*. Ph.D. thesis, Rutgers The State University of New Jersey - New Brunswick (2004).
- [200] Langreth D.C., Dion M., Rydberg H., Schröder E., Hyldgaard P., and Lundqvist B.I. *Van der Waals density functional theory with applications*. [Int. J. Quantum Chem.](#) **101**, 599 (2005).

-
- [201] Grimme S. *Accurate description of van der Waals complexes by density functional theory including empirical corrections*. [J. Comput. Chem.](#) **25**, 1463 (2004).
- [202] Vydrov O. and Van Voorhis T. *Nonlocal van der Waals Density Functional Made Simple*. [Phys. Rev. Lett.](#) **103**, 063004 (2009).
- [203] Vydrov O.A. and Van Voorhis T. *Nonlocal van der Waals density functional: The simpler the better*. [J. Chem. Phys.](#) **133**, 244103 (2010).
- [204] Grimme S., Antony J., Ehrlich S., and Krieg H. *A consistent and accurate ab initio parametrization of density functional dispersion correction (DFT-D) for the 94 elements H-Pu*. [J. Chem. Phys.](#) **132**, 154104 (2010).
- [205] Grimme S. *Density functional theory with London dispersion corrections*. [Wiley Interdiscip. Rev. Comput. Mol. Sci.](#) **1**, 211 (2011).
- [206] Tkatchenko A. and Scheffler M. *Accurate Molecular Van Der Waals Interactions from Ground-State Electron Density and Free-Atom Reference Data*. [Phys. Rev. Lett.](#) **102**, 073005 (2009).
- [207] Tkatchenko A., DiStasio R.A., Car R., and Scheffler M. *Accurate and Efficient Method for Many-Body van der Waals Interactions*. [Phys. Rev. Lett.](#) **108**, 236402 (2012).
- [208] Tkatchenko A., Ambrosetti A., and DiStasio Jr R.A. *Interatomic methods for the dispersion energy derived from the adiabatic connection fluctuation-dissipation theorem*. [J. Chem. Phys.](#) **138**, 074106 (2013).
- [209] Wu X., Vargas M.C., Nayak S., Lotrich V., and Scoles G. *Towards extending the applicability of density functional theory to weakly bound systems*. [J. Chem. Phys.](#) **115**, 8748 (2001).
- [210] Buhmann S.Y. *Dispersion Forces I*. [Springer, Berlin, Heidelberg](#) (2012).
- [211] Clay III R.C., McMinis J., McMahon J.M., Pierleoni C., Ceperley D.M., and Morales M.A. *Benchmarking exchange-correlation functionals for hydrogen at high pressures using quantum Monte Carlo*. [Phys. Rev. B](#) **89**, 184106 (2014).
- [212] Jurečka P., Šponer J., Černý J., and Hobza P. *Benchmark database of accurate (MP2 and CCSD(T) complete basis set limit) interaction energies of small model complexes, DNA base pairs, and amino acid pairs*. [Phys. Chem. Chem. Phys.](#) **8**, 1985 (2006).

- [213] Gulans A., Puska M.J., and Nieminen R.M. *Linear-scaling self-consistent implementation of the van der Waals density functional*. [Phys. Rev. B](#) **79**, 48 (2009).
- [214] Klimeš J., Bowler D.R., and Michaelides A. *Van der Waals density functionals applied to solids*. [Phys. Rev. B](#) **83**, 195131 (2011).
- [215] Klimeš J., Bowler D.R., and Michaelides A. *Chemical accuracy for the van der Waals density functional*. [J. Phys.: Condens. Matter](#) **22**, 022201 (2010).
- [216] Kohanoff J. *Electronic Structure Calculations for Solids and Molecules: Theory and Computational Methods*. [Cambridge University Press, Cambridge](#) (2006).
- [217] Blöchl P.E. *Projector augmented-wave method*. [Phys. Rev. B](#) **50**, 17953 (1994).
- [218] Kresse G. and Joubert D. *From ultrasoft pseudopotentials to the projector augmented-wave method*. [Phys. Rev. B](#) **59**, 1758 (1999).
- [219] Kresse G. and Hafner J. *Ab initio molecular dynamics for liquid metals*. [Phys. Rev. B](#) **47**, 558 (1993).
- [220] Kresse G. and Furthmüller J. *Efficiency of ab-initio total energy calculations for metals and semiconductors using a plane-wave basis set*. [Comp. Mater. Sci.](#) **6**, 15 (1996).
- [221] Kresse G. and Furthmüller J. *Efficient iterative schemes for ab initio total-energy calculations using a plane-wave basis set*. [Phys. Rev. B](#) **54**, 11169 (1996).
- [222] Feynman R.P. *Forces in Molecules*. [Phys. Rev.](#) **56**, 340 (1939).
- [223] Verlet L. *Computer "Experiments" on Classical Fluids. I. Thermodynamical Properties of Lennard-Jones Molecules*. [Phys. Rev.](#) **159**, 98 (1967).
- [224] Nosé S. *A unified formulation of the constant temperature molecular dynamics methods*. [J. Chem. Phys.](#) **81**, 511 (1984).
- [225] Hoover W.G. *Canonical dynamics: Equilibrium phase-space distributions*. [Phys. Rev. A](#) **31**, 1695 (1985).
- [226] Allen M.P. and Tildesley D.J. *Computer Simulation of Liquids*. [Oxford University Press, Oxford](#) (1989).

-
- [227] Deng Y.F., McCoy R.A., Marr R.B., Peierls R.F., and Yasar O. *Molecular dynamics on distributed-memory MIMD computers with load balancing*. [Appl. Math. Lett.](#) **8**, 37 (1995).
- [228] Vashishta P., Kalia R.K., Li W., Nakanos A., Omeltchenko A., Tsuruta K., Wang J., and Ebbsjö I. *Million atom molecular dynamics simulations of materials on parallel computers*. [Curr. Opin. Solid State Mater. Sci.](#) **1**, 853 (1996).
- [229] Becker A., Nettelmann N., Holst B., and Redmer R. *Isentropic compression of hydrogen: Probing conditions deep in planetary interiors*. [Phys. Rev. B](#) **88**, 045122 (2013).
- [230] Becker A., Lorenzen W., Fortney J.J., Nettelmann N., Schoettler M., and Redmer R. *Ab Initio Equations of State for Hydrogen (H-REOS.3) and Helium (He-REOS.3) and their Implication for the Interior of Brown Dwarfs*. [Astrophys. J. Suppl. Ser.](#) **215**, 21 (2014).
- [231] Soubiran F. and Militzer B. *The properties of heavy elements in giant planet envelopes*. [Astrophys. J.](#) **829**, 14 (2016).
- [232] Marx D. and Parrinello M. *Ab-Initio Path-Integral Molecular-Dynamics*. [Z. Phys. B: Condens. Matter](#) **95**, 143 (1994).
- [233] Marx D. and Parrinello M. *Ab initio path integral molecular dynamics: Basic ideas*. [J. Chem. Phys.](#) **104**, 4077 (1996).
- [234] Tuckerman M.E., Marx D., Klein M.L., and Parrinello M. *Efficient and general algorithms for path integral Car-Parrinello molecular dynamics*. [J. Chem. Phys.](#) **104**, 5579 (1996).
- [235] Ceriotti M., Bussi G., and Parrinello M. *Nuclear Quantum Effects in Solids Using a Colored-Noise Thermostat*. [Phys. Rev. Lett.](#) **103**, 030603 (2009).
- [236] Ceriotti M., Bussi G., and Parrinello M. *Colored-Noise Thermostats a la Carte*. [J. Chem. Theory Comput.](#) **6**, 1170 (2010).
- [237] Berens P.H., Mackay D.H.J., White G.M., and Wilson K.R. *Thermodynamics and quantum corrections from molecular dynamics for liquid water*. [J. Chem. Phys.](#) **79**, 2375 (1983).
- [238] French M. and Redmer R. *Construction of a thermodynamic potential for the water ices VII and X*. [Phys. Rev. B](#) **91**, 014308 (2015).

- [239] French M. and Redmer R. *Estimating the quantum effects from molecular vibrations of water under high pressures and temperatures.* [J. Phys.: Condens. Matter](#) **21**, 375101 (2009).
- [240] Weinhold F. *Classical and Geometrical Theory of Chemical and Phase Thermodynamics.* [John Wiley & Sons, Hoboken, New Jersey](#) (2009).
- [241] Redlich O. and Kister A.T. *Algebraic Representation of Thermodynamic Properties and the Classification of Solutions.* [Ind. Eng. Chem.](#) **40**, 345 (1948).
- [242] Lin S.T., Blanco M., and Goddard III W.A. *The two-phase model for calculating thermodynamic properties of liquids from molecular dynamics: Validation for the phase diagram of Lennard-Jones fluids.* [J. Chem. Phys.](#) **119**, 11792 (2003).
- [243] Desjarlais M.P. *First-principles calculation of entropy for liquid metals.* [Phys. Rev. E](#) **88**, 062145 (2013).
- [244] Earl B.L. *The method of intercepts: Alternative derivation.* [J. Chem. Educ.](#) **66**, 56 (1989).
- [245] French M., Desjarlais M.P., and Redmer R. *Ab initio calculation of thermodynamic potentials and entropies for superionic water.* [Phys. Rev. E](#) **93**, 022140 (2016).
- [246] Lin S.T., Maiti P.K., and Goddard W.A. *Two-Phase Thermodynamic Model for Efficient and Accurate Absolute Entropy of Water from Molecular Dynamics Simulations.* [J. Phys. Chem.](#) **114**, 8191 (2010).
- [247] Huang S.N., Pascal T.A., Goddard W.A., Maiti P.K., and Lin S.T. *Absolute Entropy and Energy of Carbon Dioxide Using the Two-Phase Thermodynamic Model.* [J. Chem. Theory Comput.](#) **7**, 1893 (2011).
- [248] Tjon J.A. *Quantum Theory of Magnetic-Resonance Line Shape in a Rigid Lattice.* [Phys. Rev.](#) **143**, 259 (1966).
- [249] Berne B.J., Boon J.P., and Rice S.A. *On the Calculation of Autocorrelation Functions of Dynamical Variables.* [J. Chem. Phys.](#) **45**, 1086 (1966).
- [250] Singwi K.S. and Tosi M.P. *On the Velocity Autocorrelation in a Classical Fluid.* [Phys. Rev.](#) **157**, 153 (1967).

- [251] Kirkwood J.G. *Statistical Mechanics of Fluid Mixtures*. [J. Chem. Phys.](#) **3**, 300 (1935).
- [252] Frenkel D. and Smit B. *Understanding Molecular Simulation*. From Algorithms to Applications. [Elsevier, Amsterdam](#) (2001).
- [253] Akima H. *A New Method of Interpolation and Smooth Curve Fitting Based on Local Procedures*. [J. ACM](#) **17**, 589 (1970).
- [254] Smith P.E. and van Gunsteren W.F. *Predictions of free energy differences from a single simulation of the initial state*. [J. Chem. Phys.](#) **100**, 577 (1994).
- [255] Hummer G. and Szabo A. *Calculation of free-energy differences from computer simulations of initial and final states*. [J. Chem. Phys.](#) **105**, 2004 (1996).
- [256] Baldereschi A. *Mean-Value Point in the Brillouin Zone*. [Phys. Rev. B](#) **7**, 5212 (1973).
- [257] Juranek H., Redmer R., and Rosenfeld Y. *Fluid variational theory for pressure dissociation in dense hydrogen: Multicomponent reference system and nonadditivity effects*. [J. Chem. Phys.](#) **117**, 1768 (2002).
- [258] Saumon D., Chabrier G., and van Horn H.M. *An Equation of State for Low-Mass Stars and Giant Planets*. [Astrophys. J. Suppl. Ser.](#) **99**, 713 (1995).
- [259] De Boor C. *A practical guide to splines*. [Springer, New York](#), 1st edition (1978).
- [260] Kippenhahn R., Weigert A., and Weiss A. *Stellar Structure and Evolution*. Astronomy and Astrophysics Library. [Springer, Berlin, Heidelberg](#) (2012).
- [261] Guillot T., Gautier D., Chabrier G., and Mosser B. *Are the Giant Planets Fully Convective*. [Icarus](#) **112**, 337 (1994).
- [262] Nettelmann N. *Matter under extreme conditions: modelling giant planets*. Ph.D. thesis, Universität Rostock (2009).
- [263] Schwarzschild K. *Über das Gleichgewicht der Sonnenatmosphäre*. Nachr. Ges. Wiss. Göttingen Math. Phys. Kl. **195**, 41 (1906).
- [264] Salpeter E.E. *Convection and Gravitational Layering in Jupiter and in Stars of Low Mass*. [Astrophys. J.](#) **181**, L83 (1973).

- [265] Hubbard W.B. *Thermal structure of Jupiter*. [Astrophys. J.](#) **152**, 745 (1968).
- [266] Guillot T., Stevenson D.J., Hubbard W.B., and Saumon D. *The interior of Jupiter*. In F. Bagenal, T.E. Dowling, and W.B. McKinnon, editors, *Jupiter. The Planet, Satellites and Magnetosphere*, pages 35–57. [Cambridge University Press, Cambridge](#) (2004).
- [267] Hanel R.A., Conrath B.J., Herath L.W., Kunde V.G., and Pirraglia J.A. *Albedo, internal heat, and energy balance of Jupiter: Preliminary results of the Voyager Infrared Investigation*. [J. Geophys. Res. Space Phys.](#) **86**, 8705 (1981).
- [268] Hanel R.A., Conrath B.J., Kunde V.G., Pearl J.C., and Pirraglia J.A. *Albedo, internal heat flux, and energy balance of Saturn*. [Icarus](#) **53**, 262 (1983).
- [269] Salpeter E.E. and Stevenson D.J. *Heat transport in a stratified two-phase fluid*. [Phys. Fluids](#) **19**, 502 (1976).
- [270] Chabrier G. and Baraffe I. *Heat Transport in Giant (Exo)planets: A New Perspective*. [Astrophys. J.](#) **661**, L81 (2007).
- [271] Nettelmann N., Wang K., Fortney J.J., Hamel S., Yellamilli S., Bethkenhagen M., and Redmer R. *Uranus evolution models with simple thermal boundary layers*. [Icarus](#) **275**, 107 (2016).
- [272] Stevenson D.J. and Salpeter E.E. *The dynamics and helium distribution in hydrogen-helium fluid planets*. [Astrophys. J. Suppl. Ser.](#) **35**, 239 (1977).
- [273] Militzer B. and Hubbard W.B. *Comparison of Jupiter interior models derived from first-principles simulations*. [Astrophys. Space Sci.](#) **322**, 129 (2009).
- [274] Seiff A., Kirk D.B., Knight T.C.D., Young R.E., Mihalov J.D., Young L.A., Milos F.S., Schubert G., Blanchard R.C., and Atkinson D. *Thermal structure of Jupiter’s atmosphere near the edge of a 5- μ m hot spot in the north equatorial belt*. [J. Geophys. Res. Planets](#) **103**, 22857 (1998).
- [275] Irwin P. *Giant Planets of Our Solar System*. [Springer, Berlin, Heidelberg](#), 2nd edition (2009).
- [276] Matzen M.K., Sweeney M.A., Adams R.G., Asay J.R., Bailey J.E., Bennett G.R., Bliss D.E., Bloomquist D.D., Brunner T.A., Campbell R.B., Chandler G.A., Coverdale C.A., Cuneo M.E., Davis J.P., Deeney C., Desjarlais

- M.P., Donovan G.L., Garasi C.J., Haill T.A., Hall C.A., Hanson D.L., Hurst M.J., Jones B., Knudson M.D., Leeper R.J., Lemke R.W., Mazarakis M.G., McDaniel D.H., Mehlhorn T.A., Nash T.J., Olson C.L., Porter J.L., Rambo P.K., Rosenthal S.E., Rochau G.A., Ruggles L.E., Ruiz C.L., Sanford T.W.L., Seamen J.F., Sinars D.B., Slutz S.A., Smith I.C., Struve K.W., Stygar W.A., Vesey R.A., Weinbrecht E.A., Wenger D.F., and Yu E.P. *Pulsed-power-driven high energy density physics and inertial confinement fusion research*). [Phys. Plasmas](#) **12**, 055503 (2005).
- [277] Cauble R., Da Silva L.B., Perry T.S., Bach D.R., Budil K.S., Celliers P., Collins G.W., Ng A., T W Barbee J., Hammel B.A., Holmes N.C., Kilkenny J.D., Wallace R.J., Chiu G., and Woolsey N.C. *Absolute measurements of the equations of state of low-Z materials in the multi-Mbar regime using laser-driven shocks*. [Phys. Plasmas](#) **4**, 1857 (1998).
- [278] Ercolessi F. and Adams J.B. *Interatomic Potentials from First-Principles Calculations: The Force-Matching Method*. [Europhys. Lett.](#) **26**, 583 (1994).
- [279] Brommer P. and Gähler F. *Potfit: effective potentials from ab initio data*. [Modell. Simul. Mater. Sci. Eng.](#) **15**, 295 (2007).
- [280] Beatty T.G. and Gaudi B.S. *Predicting the Yields of Photometric Surveys for Transiting Extrasolar Planets*. [Astrophysical Journal](#) **686**, 1302 (2008).
- [281] Schmelzer J. *Nucleation Theory and Applications*. [Wiley, Weinheim](#) (2005).
- [282] Kalikmanov V. *Nucleation Theory*. Lecture Notes in Physics. [Springer Netherlands, Dordrecht](#) (2012).
- [283] Püstow R. *Evolution des Saturn auf der Basis von ab initio - Zustandsgleichungen*. Ph.D. thesis, Universität Rostock (2015).

Curriculum Vitae / Lebenslauf

Persönliche Information

Manuel Schöttler
Kurt-Tucholsky-Str. 36
18059 Rostock

Studium

Oktober 2013 bis heute	Doktorand in der Gruppe „Statistische Physik“ von Prof. Dr. Ronald Redmer
September 2013	Masterabschluss in Physik mit Note 1,3 Masterarbeit: <i>„Ab initio Simulationen von Kohlenstoff unter extremen Bedingungen“</i> in der Gruppe von Prof. Dr. Ronald Redmer
2011 – 2013	Studium im Masterstudiengang Physik an der Universität Rostock
August 2011	Bachelorabschluss in Physik mit Note 1,7 Bachelorarbeit: <i>„Berechnung einer Zustandsgleichung für Wasser im chemischen Bild“</i> in der Gruppe von Prof. Dr. Ronald Redmer
2008 – 2011	Studium im Bachelorstudiengang Physik an der Universität Rostock

Schulbildung

Juli 2008	Abitur mit Note 1,5
2005 – 2008	Besuch des „Gymnasium Fridericianum“ in Schwerin

2000 – 2005	Besuch des „Herder Gymnasium“ in Schwerin
1995 – 2000	Besuch der „Grundschule Lankow“ in Schwerin

Veröffentlichungen

1. Schöttler M. und Redmer R. *Simulations of H-He mixtures using the van der Waals density functional.* [J. Plasma Phys.](#) **84**, 755840401 (2018).
2. Schöttler M. und Redmer R. *Ab Initio Calculation of the Miscibility Diagram for Hydrogen-Helium Mixtures.* [Phys. Rev. Lett.](#) **120**, 115703 (2018).
3. Schöttler M., French M., Cebulla D. und Redmer R. *Free energy model for solid high-pressure phases of carbon.* [J. Phys.: Condens. Matter](#) **28**, 145401 (2016).
4. Becker A., Lorenzen W., Fortney J.J., Nettelmann N., Schöttler M. und Redmer R. *Ab Initio Equations of State for Hydrogen (H-REOS.3) und Helium (He-REOS.3) und their Implications for the Interior of Brown Dwarfs.* [Astrophys. J. Suppl. Ser.](#) **215** (2014).
5. Schöttler M., Redmer R. und French M. *Low-Density Equation of State for Water from a Chemical Model.* [Contrib. Plasma Phys.](#) **53**, 336 (2013).

Fachvorträge

1. *Miscibility gap of hydrogen-helium mixtures*
Manuel Schöttler und Ronald Redmer
International Conference Strongly Coupled Coulomb Systems, Kiel, Germany, 31.07.2017
2. *Miscibility gap of hydrogen-helium mixtures*
Manuel Schöttler und Ronald Redmer
9th International Workshop on Warm Dense Matter, Vancouver, Canada, 12.04.2017
3. *Miscibility gap of hydrogen-helium mixtures*
Manuel Schöttler und Ronald Redmer
Graduiertenkolleg, Rostock, Germany, 26.01.2017
4. *Miscibility gap of hydrogen-helium mixtures*
Manuel Schöttler und Ronald Redmer

5th Joint Workshop on High Pressure, Planetary und Plasma Physics, Hamburg, Germany, 14.09.2016

5. *Miscibility gap of hydrogen-helium mixtures und metallization of hydrogen*

Manuel Schöttler und Ronald Redmer

Summer School on 'Putting the Theory Back in Density Functional Theory', Los Angeles, United States of America, 25.08.2016

6. *Free energy model for the high pressure solid phases of carbon*

Manuel Schöttler, Martin French und Ronald Redmer

4th Joint Workshop on High Pressure, Planetary und Plasma Physics, Bayreuth, Germany, 24.09.2015

7. *Free energy model for the high pressure solid phases of carbon*

Manuel Schöttler, Martin French und Ronald Redmer

15th Conference on the Physics of Non-Ideal Plasmas, Almaty, Kazakhstan, 01.09.2015

8. *Entropy of Liquids from DFT-MD*

Manuel Schöttler, Martin French und Ronald Redmer, 5th PlanetMag Meeting, Nördlingen, Germany, 11.03.2015

9. *Ab initio simulations of Carbon und Magnesium Oxide under extreme conditions*

Manuel Schöttler, Daniel Cebulla und Ronald Redmer

Physics of High Energy Density in Matter, Hirschegg, Austria, 31.01.2014

Manuel Schöttler, 10.08.2018

Acknowledgments / Danksagung

Ich möchte mich an dieser Stelle bei allen bedanken, die mich auf dem Weg zu dieser Arbeit begleitet haben. Zuallererst danke ich Prof. Redmer, dass er mir ermöglicht hat diese Arbeit in der Arbeitsgruppe Statistische Physik anzufertigen und mir mit vielen guten Ratschlägen zur Seite stand. Weiterhin geht mein Dank an alle übrigen Mitglieder der AGSP für die vielen Diskussionen über Physik, Star Trek und andere wichtige Dinge des Lebens. Ich danke auch meinen Eltern, dass sie mir das Studium der Physik ermöglicht und mich bei meinem Weg immer unterstützt haben. Mein größter Dank geht an meine Freundin Stefanie, die mir in dieser Zeit eine wundervolle Tochter geschenkt hat und mir in der schwierigen Endphase dieser Arbeit stets den Rücken frei gehalten hat, auch wenn es für uns beide nicht immer leicht war.

Statement of authorship / Selbständigkeitserklärung

I hereby declare that I am the sole author of this thesis and that I have not used any sources other than those listed in the bibliography and identified as references. I further declare that I have not submitted this thesis at any other institution in this form or a otherwise.

Ich versichere hiermit an Eides statt, dass ich die vorliegende Arbeit selbständig angefertigt und ohne fremde Hilfe verfasst habe, keine außer den von mir angegebenen Hilfsmitteln und Quellen dazu verwendet habe und die den benutzten Werken inhaltlich und wörtlich entnommenen Stellen als solche kenntlich gemacht habe. Weiterhin versichere ich, dass ich diese Arbeit an keiner anderen Institution in dieser oder einer ähnlichen Form eingereicht habe.

Rostock, 10.08.2018